Western Australian School of Mines
Department of Exploration Geophysics

Coherency based time-domain imaging algorithms

Mohammad Javad Khoshnavaz

This thesis is presented for the Degree of
Doctor of Philosophy
of
Curtin University

May 2016

Declaration

To the best of my knowledge and belief this thesis contains no material previously published by any other person except where due acknowledgment has been made.

This thesis contains no material which has been accepted for the award of any other degree or diploma in any university.

Signature: …….

Date: ……16/05/2016…...

“Education is not the learnings of facts, but the training of the mind to think”

and

“We cannot solve our problems with the same thinking we used when we created them”

— Albert Einstein

I would like to dedicate this thesis to all scientists and reserachers who spent their whole life to learn more and to enlighten the humans.

Acknowledgements

I would like to express my sincere gratitude to my advisor Associate Professor Dr. Milovan Urosevic for providing me an opportunity to carry out my PhD at the Department of Exploration Geophysics at Curtin University. I am most grateful to him for spending his valuable time to review my thesis and for providing helpful feedback.

I wish to thank my second advisor Associate Professor Dr. Andrej Bóna whose office was always open to me for technical discussions. Without his kind technical support, the completion of this thesis would not have been possible.

It gives me immense pleasure to thank the former head of the Department of Exploration Geophysics at Curtin University, Professor Dr. Boris Gurevich, and the chair of my advisory panel, Associate Professor Dr. Maxim Lebedev, for their support.

I am indebted to Dr. Kit Chambers for his immense supports, advices and help during my PhD in the area of passive seismic monitoring and location.

Very special thank goes to Professor Dr. Sergey Fomel form University of Texas at Austin (UT Austin) for providing me an opportunity to visit him at UT Austin as a visiting researcher. I would like to thank him for his support, technical discussions, advises and for reviewing the technical contents of my research, and also for providing Madagascar, an open-source software package for multidimensional data analysis.

I would like to thank Ms. Deirdre Hollingsworth, the administrative officer in the Department of Exploration Geophysics at Curtin University during my PhD, for her kind help and support.

I am grateful to Halliburton, First Quantum Minerals Ltd and Geoscience Australia for providing me the permissions to use their seismic data sets for this research.

This work has been supported by the Deep Exploration Technologies Cooperative Research Centre (DET CRC) whose activities are funded by the Australian Government's Cooperative Research Centre Programme.

I am obliged to the DET CRC and Curtin University for the Scholarships awarded to me.

Last but not the least, I would like to thank my family, my parents and to my brother and sister for encouragements and supporting me spiritually throughout writing this thesis and life in general. I would also like to thank all my colleagues and friends who were always supportive over the last three and half years in building this thesis.

Table of contents

List of figures

List of tables

1. Introduction

Seismic method is one of the main techniques in exploration geophysics. The key concept is to send elastic waves into the ground using various sources and to evaluate subsurface structures by analysing the seismic responses recorded by ultrasensitive receivers. Seismic imaging is a process that reconstructs the subsurface geological structures from their seismic responses. There are two main streams in seismic imaging: time- and depth-domain. Time-domain imaging relies only on wave extrapolation in time, while depth-domain imaging is the genuine inverse process that attempts to produce true seismic representation of the underground geology. As such depth imaging is prone to inconsistencies, particularly in an environment where geological structures are close to Fresnel zone size or less, as typically found in mineral exploration and hard rock environment. In such type of environment, time-domain imaging is more stable process and therefore is the main focus of this thesis.

1.1. Time-domain imaging

Seismic time-domain imaging, which is one of the most robust tools in seismic data processing, is the workhorse of seismic data processing (Yilmaz, 2000; Fomel, 2014). The fundamental concept in time-domain imaging is wave propagation/emission through a homogenous media with a constant effective velocity. From there on, further complexities resembling the real geology are added and solved in different ways. Compared with depth-domain imaging, time-domain imaging employs a reduced number of parameters by taking effective approximations for wave propagation in the subsurface (Glogovsky et al., 2009). Despite the limited accuracy of time-domain imaging techniques in complex structures, it is a robust and reliable imaging tool for most of the geological situations, including unconventional reservoirs on land (Fomel, 2014).

In routine seismic time-domain imaging, the imaging parameters (e.g., velocity), particularly in oil and gas exploration, are estimated by semblance analysis (Taner and Koehler, 1969). This is generally labour-intensive and time-consuming

(Yilmaz, 2000; Fomel, 2007). Such workflows are often designed for only horizontally layered models and an experienced processor is required to pick the velocities in the velocity spectrum. Further level of complications is encountered in the presence of seismic anisotropy. Taking anisotropy into account, where more than a single parameter is required for higher-order traveltime approximations (e.g., Alkhalifah and Tsvankin, 1995; Fomel and Stovas, 2010), estimation of imaging parameters using classic semblance analysis becomes more time-consuming.

1.2. Oriented time-domain imaging

An alternative to the conventional velocity analysis techniques is oriented, velocity-independent or velocity-less time-domain imaging that uses seismic local slopes (e.g., Ottolini, 1983; Fomel, 2007, Cooke et al, 2009) and in some cases the higher order derivatives of traveltime with respect to the position of receivers deployed on the acquisition surface (Bóna, 2011; Khoshnavaz et al., 2015a). The derivatives, including the local slopes, carry complete information about the subsurface structures (Fomel, 2007). The oriented techniques do not require a priori knowledge of a velocity model. There are two approaches along this path; first is mapping the seismic data from the prestack domain to image domain directly (e.g., Fomel, 2007); and the second is simultaneous velocity analysis and imaging. Therefore, developments of innovative oriented time-domain imaging algorithms is of particular interest in this research.

1.3. Diffraction imaging

Other than the reflected seismic energy traditionally used in exploration seismology, there is also scattered energy related to diffractions. Diffractions, which carry valuable information about the local discontinuities and small scale objects (Papziner and Nick 1998), are rarely used in the process of geological interpretation. In routine seismic methods, diffractions are often recognized and interpreted by visual observation of an experienced interpreter and the reliability of such interpretation is low and very

subjective (Landa and Keydar, 1998). Diffraction imaging is an objective process that uses the information carried by diffractions. It is worth mentioning that since seismic migration removes the diffractions, diffraction imaging must be performed either in prestack- or in poststack zero-offset domain.

Many techniques for the imaging of seismic diffractions, in both post- and prestack domains, have been proposed and applied for isotropic media (e.g., Dell and Gajewski, 2011; Aloniazi et al., 2013), while relatively few techniques have been developed for anisotropic media. Ignoring anisotropy can result in low resolution images with wrongly positioned or spurious diffrators (e.g., Dell and Gajewski, 2013). Obtaining higher resolution images of diffractors by taking anisotropy into account is another focus of this research.

Despite the natural lack of reflectors and potentially abundant number of diffrators in hard rock environment (Eaton et al., 2003; Urosevic et al., 2012), there are only few studies of diffraction characterisation and imaging in hard rock environments (e.g., Bóna et al. 2013) with almost no examples of 3D diffraction imaging in prestack domain. Thus, it is important to fully investigate the potential utilisation of prestack diffraction imaging for delineation of complex geological structures, which are often found in hard rock environment. Hence, the applicability of diffraction analysis and imaging may be of key importance for further advances in the hard rock seismic exploration.

1.4. Objectives

Accurate time-efficient seismic imaging, which is certainly of interest for resolving complex geological situations through seismic methods, requires a nonconventional critical thinking. Hence, this thesis focuses on developing innovative seismic imaging algorithms/workflows in different areas of seismic exploration. The main objectives of this thesis are summarised as follows:

- To extend the idea of oriented time-domain imaging to microseismic/passive seismic monitoring,
- To simplify, improve and further develop the previous oriented techniques for the estimation of kinematic attributes in VTI media, by proposing a higher resolution approach,
- To improve the applicability of the currently available prestack oriented time-domain seismic imaging techniques by proposing a new migration approach for specular reflectors in common source domain,
- To suggest taking anisotropy into account for 2D poststack diffraction imaging to obtain higher resolution images, and
- To consider diffractivity (obtained by the application of 3D prestack diffraction imaging) as another attribute for the interpretation of seismic data collected over hard rock environments.

1.5. Thesis structure

This thesis is divided into seven chapters. These chapters are designed based on the research directions undertaken and published in "GEOPHYSICS", "INTERPRETATION", "GEOPHYSICAL PROSPECTING", and presented in the Society of Exploration Geophysics (SEG), the European Association of Geoscientists and Engineers (EAGE), and the Australian Society of Exploration Geophysicist (ASEG). These publications are listed in the references section, at the end of this chapter.

The ***introductory chapter*** provides a brief definition of time-domain seismic imaging, and a brief explanation about the challenges and the advantages in the existing time-domain imaging algorithms. The research objectives in this PhD research are included and summarised in the chapter.

In ***chapter 2***, I explained the advantages as well as challenges of the existing microseismic and/or passive seismic monitoring algorithms. Then, I developed a new algorithm and extended the idea of oriented time-domain seismic imaging to surface

passive seismic monitoring. The proposed technique is an oriented technique that uses local event slopes (Khoshnavaz et al., 2015b and 2017b). The technique is demonstrated on 2D synthetic data examples and is applied to a 3D field data set. In the process, I also described and applied a technique to evaluate the uncertainty in the focal position estimates using the bootstrap method.

In ***chapter 3***, I proposed a fully automated oriented algorithm for the inversion of kinematic attributes in vertical-transverse-isotropy (VTI) media (Khoshnavaz et al., 2016a). I further developed, improved and simplified the previous oriented techniques by removing one order of differentiation from the imaging attributes (e.g., anisotropy anellipticity coefficient η). These kinematic attributes are derived in terms of the local event slopes and the vertical two-way-travel-time. Use of predictive painting, which keeps all the attributes independent from the second derivative of two-way-travel-time (TWTT) with respect to offset (curvature), is proposed to estimate the vertical TWTT. The method can be orders of magnitudes faster than the routine multi-parameter semblance scanning.

In ***chapter 4***, I developed an oriented time-domain prestack migration, in common-source domain for specular reflectors (Khoshnavaz et al., 2016b). In some of the previous oriented imaging techniques, seismic data must be sorted in two different domains while seismic data is not always available in both domains and the use of interpolation is inevitable. As an example, some techniques need the same number of traces in both shot and receiver domain (reciprocal array) that is not often available. Some others are developed in terms of the higher order derivatives of traveltime with respect to the location of receivers on the acquisition surface while estimation of the higher order derivatives is difficult to achieve with the required accuracy. To address these issues, I replaced the need for higher order derivatives for the approximations of migration attributes by a point-to-point mapping approach using predictive painting technique. The theoretical contents of the proposed techniques were demonstrated on a 2D synthetic data example and applied to a field data set.

In ***chapter 5***, I discussed the existing poststack diffraction imaging techniques for isotropic and anisotropic media. It is discussed that the ignorance of anisotropy in the presence of anisotropy results in low resolution images with wrongly positioned or

spurious diffrators. To address these issues, I suggest to take anisotropy into account for 2D poststack diffraction imaging by considering non-hyperbolic diffraction traveltime approximations for VTI media, previously developed for reflection seismology (Khoshnavaz et al., 2017a). I also quantified the accuracy of six different approximations, including hyperbolic moveout approximation, by the application of anisotropic diffraction imaging algorithm on 2D synthetic data examples.

Chapter 6, addressed the difficulties encountered in the exploration of mineral deposits in hard rock environment using reflection seismic methods and the corresponding challenges, which are due to lack of continuous reflectors and sub-horizontal reflectors. In such environments, the heterogeneities and "fractal" hard rock geological environment produce considerable scattering of the seismic energy in the form of diffracted waves. For the first time, it is suggested to consider/apply 3D prestack diffraction imaging to compute "diffractivity", which is a robust attribute for identifying, detecting and locating the source of diffractions generated from highly fractured zones, terminations of mineralized rocks and the wedges of vertical intrusions (Khoshnavaz et al., 2015c, 2016c and 2016d).

Chapter 7, is the concluding chapter. In the chapter, I discussed the proposed and/or suggested techniques, the corresponding observations, advantages, challenges, the roads ahead and the potential research that can be done in the future to improve the techniques.

Each chapter contains a brif overview followed by an introduction, methodology, applications, disussion (if applies) and conclusion sections. For convinience, a list of references used in each topic/chaper is provided at the end of each chapter. A list of figures and tables are provided before the introductory chapter.

1.6. References

Alkhalifah, T., and I. Tsvankin, 1995, Velocity analysis for transversely isotropic media: Geophysics, **60**, 1550–1566, doi:10.1190/1.1443888.

Alonaizi, F., R. Pevzner, A. Bóna, V. Shulakova, and B. Gurevich, 2013, 3D diffraction imaging of linear features and its application to seismic monitoring: Geophysical Prospecting, **61**, no. 6, 1206-1217.

Bóna, A., 2011, Shot-gather time migration of planar reflectors without velocity model: Geophysics, **76**, no. 2, S93–S101.

Bóna, A., R. Pevzner, K. Tertyshnikov, A. Greenwood, B. Sun, S. Yavuz, and Urosevic M., 2013, Diffraction Imaging in Hard-rock Environments: 75th Conference and Exhibition, EAGE, Extended Abstracts, doi: 10.3997/2214-4609.20130702.

Cooke, D., A. Bóna, and B. Hansen, 2009, Simultaneous time imaging, velocity estimation and multiple suppression using local event slopes: Geophysics, **74**, no. 6, WCA65–WCA73.

Dell, S., and D. Gajewski, 2011, Common-reflection-surface-based workflow for diffraction imaging: Geophysics, **76**, no. 5, S187-S195.

Dell, S., A. Pronevich, B. Kashtan, and D. Gajewski, 2013, Diffraction traveltime approximation for general anisotropic media: Geophysics, **78**, no. 5, WC15-WC23.

Eaton, D.W., B. Milkereit, and M. Salisbury, 2003, Seismic Methods for Deep Mineral Exploration: Mature Technologies Adapted to New Targets: The Leading Edge, **22**, no. 6, 580-585.

Fomel, S., 2014, Recent advances in time-domain seismic imaging: 84th Annual International Meeting, SEG, Expanded Abstracts, 4400–4404.

Fomel, S., and A. Stovas, 2010, Generalized nonhyperbolic moveout approximation: Geophysics, **75**, no. 2, U9–U18, doi:10.1190/1.3334323.

Fomel, S., 2007, Velocity-independent time-domain seismic imaging using local event slopes: Geophysics, **72**, no. 3, S139–S147, doi: 10.1190/1.2714047.

Glogovsky, V., E. Landa, S. Langman, and T. Moser, 2009, Validating the velocity model: The Hamburg score: First Break, **27**, no. 3, 77–85.

Khoshnavaz, M. J., A. Bóna, and M. Urosevic, 2017a, Poststack diffraction imaging in vertical transverse isotropy media using non-hyperbolic moveout approximations: Geophysical prospecting, doi: 10.1111/1365-2478.12515.

Khoshnavaz, M. J., K. Chambers, A. Bóna, and M. Urosevic, 2017b, Oriented surface passive seismic location using local slopes: Geophysics, **82**, no. 2, KS13–KS25, doi: 10.1190/GEO2016-0017.1.

Khoshnavaz, M. J., A. Bóna, and M. Urosevic, 2016a, Velocity-independent estimation of kinematic attributes in vertical transverse isotropy media using local slopes and predictive painting: Geophysics, **81**, no. 5, U73-U85, doi: 10.1190/GEO2015-0638.1.

Khoshnavaz, M. J., A. Bóna, A. Dzunic, K. Ung, and M. Urosevic, 2016b, Oriented prestack time migration using local slopes and predictive painting in the common-source domain for planar reflectors: Geophysics, **81**, no. 6, S409–S418, doi: 10.1190/GEO2016-0127.1.

Khoshnavaz, M. J., A. Bóna, M. S. Hossain, and M. Urosevic, 2016c, Prestack diffraction imaging and its application in the exploration of mineral deposits: 25th

ASEG International Geophysical Conference and Exhibition, South Australia. http://www.publish.csiro.au/?act=view_file&file_id=ASEG2016ab172.pdf

Khoshnavaz, M. J., A. Bóna, M. S. Hossain, M. Urosevic, and K. Chambers, 2016d, Diffractivity- another attribute for the interpretation of seismic data in hard-rock environment, a case study: Interpretation, **4**, no. 4, B23-B32, doi: 10.1190/INT-2016-0023.1.

Khoshnavaz, M. J., Bóna, A., and Urosevic, M., 2015a, Pre-stack time migration in common source domain without velocity model: In 77th EAGE Conference and Exhibition; Tu P3 09, doi: 10.3997/2214-4609.201412779.

Khoshnavaz, M. J., K. Chambers, A. Bóna, and M. Urosevic, 2015b, Passive seismic localization without velocity model: application and uncertainty analysis: Annual SEG Meeting, Expanded Abstracts, 2467-2472, doi: 10.1190/segam2015-5915362.1.

Khoshnavaz, M. J., A. Bóna, M. Urosevic, S. Ziramov, and P. Ahmadi, 2015c, Pre-stack Diffraction Imaging and Its Application in Hard Rock Environment: 77th EAGE Conference and Exhibition, doi: 10.3997/2214-4609.201413006.

Landa, E., and S. Keydar, 1998, Seismic monitoring of diffraction images for detection of local heterogeneities, Geophysics, **63**, no. 3, 1093-1100.

Ottolini, R., 1983, Velocity independent seismic imaging: Stanford Exploration Project, **37**, 59–68.

Papziner, U., and K.P. Nick, 1998, Automatic detection of hyperbolas in georadargrams by slant-stack processing and migration: First Break, **16**, 219–223.

Taner, M.T., and M. Koehler, 1969, Velocity spectra-digital computer derivation applications of velocity functions: Geophysics, **34**, no. 6, 859-881.

Urosevic, M., G. Bhat, and M.H. Grochau, 2012, Targeting nickel sulfide deposits from 3D seismic reflection data at Kambalda, Australia: Geophysics, **77**, no. 5, WC123–WC132.

Yilmaz, Ö., 2000, Seismic data analysis: SEG.

2. Oriented surface passive seismic location using local slopes

2.1. Overview

Conventional exploration approach uses active seismic methods for studying the underground structures. While this is definitely the primary exploration approach/tool in oil and gas industry, it is less attractive for the mineral industry due to the high cost associated with this method. Lately, passive seismic methods came under investigation as an alternative imaging approach. One possibility is to use passive seismic prior to active seismic survey. In such scenario passive seismic surveys would be used over a vast space to localise the area where active seismic is required for detailed underground imaging. Such "hybrid" approach might be used in the mineral exploration space.

Passive seismic location is a procedure for locating seismic sources when the source locations and timings are unknown. It includes the location of passive seismic events made by drilling, fault displacement and hydraulic fracturing in permeable formations and has applications in the oil and gas as well as the mining industry. The main applications of passive seismic techniques include the monitoring of hydraulic-fractures and mining-induced seismicity for the management of hazards in deep hard rock mines. A common acquisition scenario in microseismic monitoring is the deployment of large areal receiver arrays on the surface of the earth above the region of activity. This acquisition geometry has the advantage of providing coverage of the source's focal hemisphere as well as characterization of the arrival time moveout curve; however, the accuracy of many location techniques applied to these data sets depends upon the accuracy of the velocity model provided prior to locationing. In this chapter, an oriented locationing technique is proposed whereby the wavefront focal points are estimated using the information carried by local slopes. These focal points are then used as constraints for a fit of a moveout relationship to a set of travel times. The focal coordinates of the passive source is then obtained from the coefficients of the moveout curve. The procedure has the advantage that full knowledge of a velocity

model is not required a priori. The performance of the proposed technique is demonstrated on several 2D synthetic data examples and on a 3D field data set. The results suggest that, despite the assumption of the method that the arrival moveout can be modelled using a constant effective velocity, a reliable event location is achieved. In fact the tests showed that the focal point coincides with the true source position provided the medium does not contain large lateral velocity variations. A procedure to assess the uncertainty of the proposed technique using bootstrap statistics is also described and applied to the field data set.

2.2. Introduction

As opposed to active seismic, passive seismic events are not generated from a dedicated controlled seismic source. Vibrations made by drilling, fault displacement and hydraulic fracturing during high-pressure fluid injection into permeable formations are generally known as passive seismic sources. It is established that the study of the distribution of passive seismic sources is a useful tool in the mining industry, as well as, unconventional reservoir development in the oil and gas industry (Chambers et al. 2014). Passive seismic monitoring has also been used in the mining industry over the last century with different applications: a) monitoring mining-induced seismicity for hazard management in deep hard rock mines (Mikula et al., 2008), b) drill-bit location in the subsurface such as in the case of coil tube (CT) drilling, when there is uncertainty about the position of the drill-bit caused by the flexibility of the tube (Mokaramian and Rasouli, 2013), and c) seismic velocity estimation/calibration down the borehole in seismic-while-drilling methods (Sun et al., 2014). The application of surface passive seismic monitoring in oil and gas industry is relatively new and includes the monitoring of passive seismic events induced by different reservoir activities, such as hydraulic fracturing (Anikiev et al., 2013). Monitoring of such activities gives significant information about the fluid flow paths and helps to optimize well design and reservoir drainage.

According to Maxwell et al. (2010), there are two main acquisition strategies employed in passive seismic monitoring: down-hole and surface acquisition. For

down-hole acquisition, a limited number of three-component (3C) geophones are placed into one or more observation wells near the passive source (Eisner et al., 2011). The main advantages of this technique are its high depth resolution and the high signal-to-noise ratio (S/N) of the recorded arrivals; however, borehole monitoring requires the presence of a well suitable for deploying 3C down-hole geophones leading to a limited monitoring aperture (Duncan and Eisner, 2010), and may require that the observation well be taken out of production during the monitoring process (Chambers et al., 2010a), also use of the expensive 3C downhole receivers is required.

Surface passive monitoring is an alternative strategy that makes use of hundreds or even thousands of sensors deployed on the surface or in shallow vertical observation wells on top of the passive source (Duncan and Eisner, 2010; Eisner et al., 2011). The wide spatial aperture of surface microseismic surveys provides additional coverage of the focal hemisphere leading to better determinations of the source mechanism as well as the possibility to monitor larger volumes. The intrinsic S/N for this technique is low; however, the high fold count provides a vastly improved S/N after stacking (Chambers, 2010b). The locationing methods applied to surface passive seismic data are typically similar to depth-imaging algorithms and are dependent upon the accuracy of the subsurface velocity model provided before the monitoring process; however, an accurate velocity model is often not available (Pavlis, 1986; Maxwell et al., 2010). Accordingly, most surveys include a calibration step where an initial velocity model extrapolated/derived from well logs measuring the petrophysical properties is optimized using known calibration source(s), typically perforation shots.

In contrast, oriented imaging techniques utilize arrival attributes estimated from local slope information (Fomel, 2007; Cooke 2009) and hence do not require a fully parameterized velocity model. Such techniques have been used effectively in active seismic imaging with the assumption of wave emission through a constant velocity medium (e.g. Ottolini, 1983; Fomel, 2007; Bóna, 2011; Casasanta and Fomel, 2011; Stovas and Fomel, 2016), the general assumption in time-domain seismic imaging. Time-domain imaging is robust and is the workhorse of seismic data processing (Yilmaz, 2000; Fomel 2014). Compared with depth imaging, time-domain imaging utilizes a reduced number of parameters by taking effective approximations for wave propagation in the subsurface (Glogovsky et al., 2009; Fomel, 2014). According to

Fomel (2014), despite the limited applicability of time-domain imaging techniques in complicated structures, it is a robust imaging tool for many situations, including unconventional reservoirs on land (e.g., Bancroft, 2007; Gei et al., 2011).

Khoshnavaz et al. (2015) extended the idea of oriented time-domain imaging to surface passive seismic imaging such that there was no need for a fully parameterized velocity model. Their technique uses higher order derivatives (first, second and the third) of arrival times with respect to the position of the receivers deployed on the observation surface (see Appendices A and B for details). Here, the technique is developed further such that the second and the third derivatives of arrival time are not required, thus increasing the efficiency and applicability of the method.

In the proposed technique, a moveout curve is fitted to a set of observed arrival times, in order to smooth and stabilize subsequent estimates of the moveout midpoint (the point of minimum arrival time) and the local slopes. The local slopes together with the center of the moevout curve are then used to derive a range of estimates for the vertical coordinate of the passive seismic source, the effective velocity of the medium and the origin time. A secondary fit of the hyperbolic moveout equation which is constrained by the range of these parameters is then performed. The final location, origin time and effective velocity are then estimated from the secondary hyperbolic fit. Similar to the previous time-domain passive imaging techniques (e.g., Vidale 1988; Bancroft and Xu, 2005; Bancroft, 2010; Gei et al., 2011), the proposed technique for identifying the source position is based on the assumption of wave emission through a constant effective velocity medium. In other words, the technique assumes the seismic wavefront is locally spherical in the area of interest, and that the center of curvature corresponds to the apparent source of the spherical wavefront.

A theoretical description of the technique is provided in this chapter followed by demonstrations of its performance on several 2D synthetic data, and then to a 3D field data set. In the process, I also described and applied a technique to evaluate the uncertainty in the focal position estimates using the bootstrap method. The obtained results show that despite the approximations in the method (i.e., assumption of homogeneity) reliable results were obtained, provided that the underlying medium does not contain strong lateral heterogeneities.

2.3. Methodology

The first step in the procedure is to fit a hyperbolic moveout to the observed arrival times, *t*, at observed array receivers, x_r,

$$t = s + \sqrt{{t_0}^2 + \left(\frac{x_r - x_s}{v}\right)^2} \tag{2.1}$$

where *s*, t_0, x_s, and *v* are time-shift, vertical travel-time, horizontal coordinate of the passive source and the effective velocity of the medium that should be determined. Given a set of arrival times, the parameters in equation 2.1 are solved for using trust region reflective least squares algorithm. The initial conditions are $t_0 = t_{min}$, $x_s = x_{smin}$, $s = s_{min}$, $v = v_{min}$. For this initial fit the trust region is kept deliberately broad whereby the solutions are only constrained to lie in the ranges $t_{min} < t_0 < t_{max}$, $x_{min} < x_s < x_{max}$, $s_{min} < x_s < s_{max}$ and $v_{min} < v < v_{max}$.

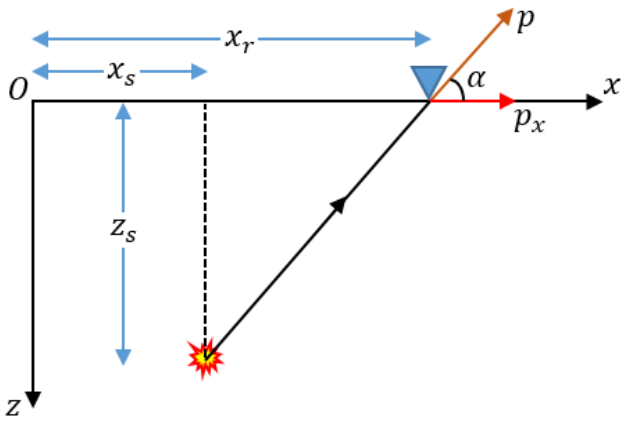

Figure 2.1: Geometry of an emitted wavefront from a passive seismic source.

For a set of arrival times from a linear surface array, the parameter x_s provides an estimate of the horizontal focal coordinate of the source. This is also the most accurately and uniquely constrained coefficient in the fitting of equation 2.1. Similarly, *s*, would correspond to the origin time, *v*, the effective velocity of the medium, and t_0 the vertical travel time related to the vertical source coordinate by $z_s = vt_0$. So, in principle, the parameters from equation 2.1 should constrain the position of the source in a medium with a constant effective velocity. However, initial tests showed more accurate estimates for the source positions are obtained through the fitting of equation 2.1 with a tighter set of constraints. Rather than specifying those constraints a priori, instead, I utilized the coefficients determined from the first fit of equation 2.1 to

provide x_s and local slope information, which in turn are used to derive a range of estimates for the source origin time, the source depth and the effective velocity of the medium. This range of estimates are then used as constraints for a subsequent re-fit of the moveout approximation providing more accurate and robust source locations.

The formula for the range estimates for *s*, t_0, and *v* are based upon the focal points for the incident arrival as a function of receiver position in the array, ($x_s(x)$, $z_s(x)$). Considering the schematic geometry of an emitted wavefront from a passive source to a receiver on the surface through an effective constant velocity medium (Figure 2.1), the coordinates of the focal points are given by

$$x_s(x) = x_r - Rcos(\alpha), \tag{2.2}$$

$$z_s(x) = Rsin(\alpha). \tag{2.3}$$

where α is the angle between the observation line on the surface ($z = 0$) and the direction of the emitted ray reaching to the receiver. *R* denotes the radius of the curvature of the emitted wavefront, from the passive source to the receivers. The radius is equal to the traveltime divided by the effective slowness (*p*), which is the inverse of the effective velocity,

$$R = vt = \frac{t}{p}. \tag{2.4}$$

The trigonometric connections between the effective emission angle (α), the effective slowness (*p*) and the local slope (p_x) are given by

$$cos\,\alpha(x) = \frac{p_x}{p}, \tag{2.5}$$

$$sin\,\alpha(x) = \sqrt{1 - \left(\frac{p_x}{p}\right)^2}. \tag{2.6}$$

Substitution of equations 2.4, 2.5 and 2.6 in equations 2.2 and 2.3 gives

$$x_s(x) = x_r - \frac{tp_x}{p^2}, \tag{2.7}$$

$$z_s(x) = \frac{t}{p}\sqrt{1 - \left(\frac{p_x}{p}\right)^2}. \tag{2.8}$$

After some algebra and using the relationship

$$c = (t + s) - (t_0 + s) = t - t_0, \tag{2.9}$$

and $v = 1/p$, one can obtain the following expressions for the effective velocity (v), vertical traveltime (t_0) and source depth (z_s) as a function of local slope (p_x) and horizontal offset ($x_r - x_s$)

$$v(x_r) = \sqrt{\frac{2(x_r - x_s)}{cp_x} - \frac{(x_r - x_s)^2}{c^2}}, \tag{2.10}$$

$$t_0(x_r) = c\left[\frac{c}{2c - (x_r - x_s)p_x} - 1\right], \tag{2.11}$$

$$z_s(x_r) = \sqrt{\frac{p_x(x_r - x_s)}{2c - p_x(x_r - x_s)}}\left[(x_r - x_s) - \frac{c}{p_x}\right]. \tag{2.12}$$

So, given the estimates for x_s, p_x and c, derived from the fit of the initial hyperbola equations 2.10-2.12, provide estimates for the velocity, vertical traveltime and the vertical coordinate of the passive source as a function of receiver position.

The final step is to return to equation 2.1 and perform a constrained fit of the hyperbola using the boundaries from the distributions of $v(x_r)$, $t_0(x_r)$, $z_s(x_r)$, obtained by the application of equations 2.10-2.12. As before, a trust region reflective least squares method is used to fit equation 2.1, with the initial conditions of $t_0 = t'_{min}$, $x_s = x'_{min}$, $s = s'_{min}$, $v = v'_{min}$, and the corresponding updated constraints (e.g., $v'_{min} < v < v'_{max}$). This secondary fit then provides a final estimate of the source position x_s, $z_s = vt_0$, origin time s, and the effective velocity v.

An outline of the procedure is as follows:

1. Given a set of arrival times on a 2D line of surface sensors, a moveout curve (equation 2.1) is fitted to the arrival time data with broad constraints.
2. From the moveout curve, local/effective slopes p_x, the relative arrival time c, and the horizontal focal coordinate x_s, are estimated.
3. Equations 2.10-2.12 are used to obtain the estimates of the velocity v, origin time, t_0, and the vertical coordinate z_s, for every receiver in the sensor line.
4. The range of these estimations are then used to update the constraints for a secondary fit of the moveout curve (equation 2.1).
5. The coefficients from the secondary fit of the moveout relationship are used to provide the source position, origin time and velocity.

2.4. Synthetic data examples

2.4.1. Constant velocity media

In the first synthetic example, I used a passive source fixed in a constant velocity homogeneous medium with the coordinates of x_s =800 m and z_s =800 m. The P-velocity of the medium is 2000 m/s. Sampling interval and geophone spacing are equal to 2 ms and 10 m, respectively. An explosive source was used and a Ricker wavelet with the dominant frequency of 30 Hz. The length of the 2D observation profile on the surface was 2.5 times longer than the depth of the target. The profile has a maximum horizontal offset of 1500 m from the passive seismic source. To demonstrate the independence of the technique from source origin time, a time shift of 0.3 s was applied to all traces. Figure 2.2 shows the passive record perturbed with zero-mean white noise with the S/N of 2 that was scaled by

$$\frac{S}{N} = \frac{E_S}{E_N} = \frac{\sum_1^m \sum_1^n {A_S}_{i,j}{}^2}{\sum_1^m \sum_1^n {A_N}_{i,j}{}^2}, \tag{2.13}$$

where added on top of the synthetic records. Herein, A_S and A_N denote the amplitude of signal and noise in each sample, respectively. i and j are counters for trace number and sample number in each trace within the window of the passive seismic event.

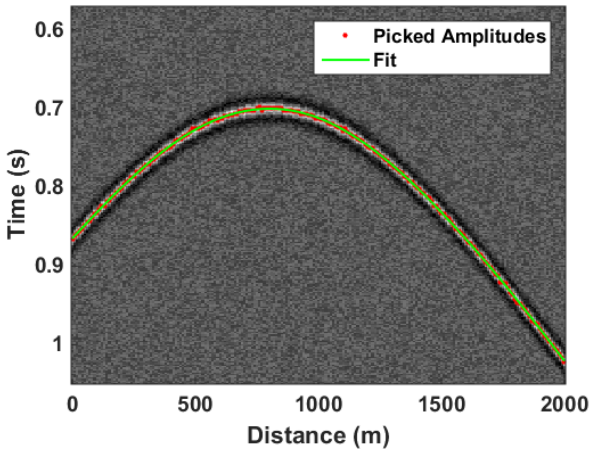

Figure 2.2: Synthetic passive record with S/N of 2. Red dots and the green curve denote the maximum picked amplitudes and the fitted hyperbolic curve on the picked amplitudes respectively.

The arrival times (red dots) are determined by the application of a stack maximization technique (e.g., Ronen and Claerbout, 1985) within the time window of

the passive record, in this example. The green curve shows the initial hyperbolic fit and the resulting parameters are provided in Table 2.1.

	s (s)	v (m/s)	x_s (m)	t_0 (s)
Minimum	-1	1000	0	0
Maximum	1	8000	2000	2

Table 2.1: Initial estimates/constraints used to fit a hyperbola to time arrivals in order to smooth them.

In the next step, I measured the local slopes from the fitted hyperbola using numerical gradient, and substituted the results in equations 2.10-2.12, which together with the horizontal coordinate estimate provide distributions for the source vertical coordinate, the origin time and the effective velocity of the medium. Figures 2.3a-2.3c show the related histograms. Many of the extreme values in the derived distributions relate to receivers near minima traveltime where the local slopes are near zero.

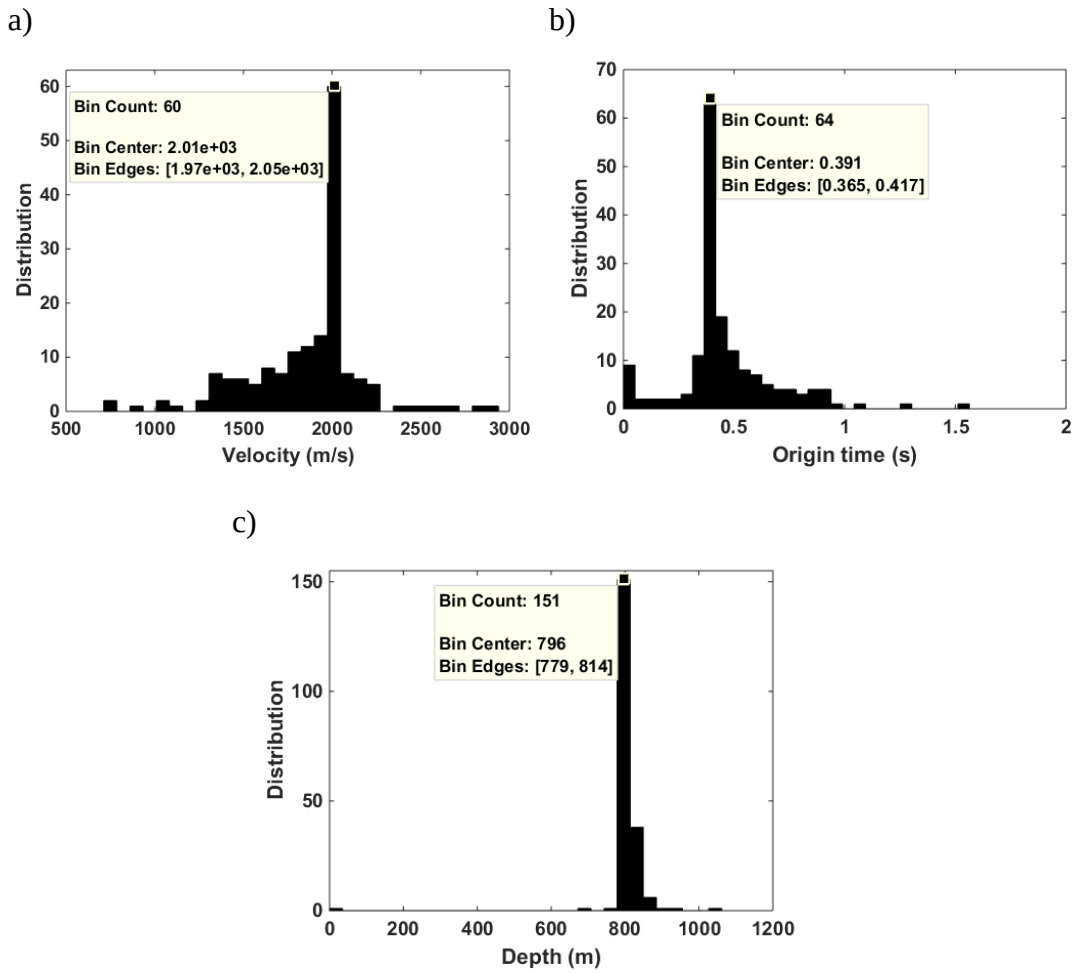

Figure 2.3: Distribution of a) effective P-velocity, b) vertical traveltime and c) vertical focal coordinate of the passive source estimated by the application of equations 2.10-2.12.

The range of these values provide the new boundaries that will be used for the second least square fitting for the inversion of the location parameters. Table 2.2 shows the final inverted parameters obtained after the second iteration of least square fitting and local slope estimation. It can be seen that the determined source location is within a few meters from the true location.

S (s)	V (m/s)	t_0 (s)	z_s (m)	x_s (m)
0.3022	2003	0.3975	798	800

Table 2.2: Final inverted coefficients using a non-linear least square fit.

The uncertainty of the proposed technique was also examined to evaluate its effectiveness. One of the main factors that influences location is perturbation around the true values of arrival times, caused by picking errors, which in turn leads to errors in the estimation of the moveout curve and the focal source position (Gei et al., 2011). I followed the uncertainty analysis approach presented by Eisner et al. (2009) and Mueller (2013). Different levels of arrival time perturbation between 0.1-1 percent are considered for this study. For each perturbation level, 1000 perturbed traveltime curves were generated and the proposed technique was applied to each record, separately.

Figures 2.4a-2.4b show the standard deviation of the misfit for each level of perturbation in the horizontal and vertical directions, respectively, whilst Figures 2.4c-2.4f show the probability density functions (PDFs) derived from the 1000 experiments at the perturbation level of 0.3, 0.5, 0.7 and 0.9 percent, respectively.

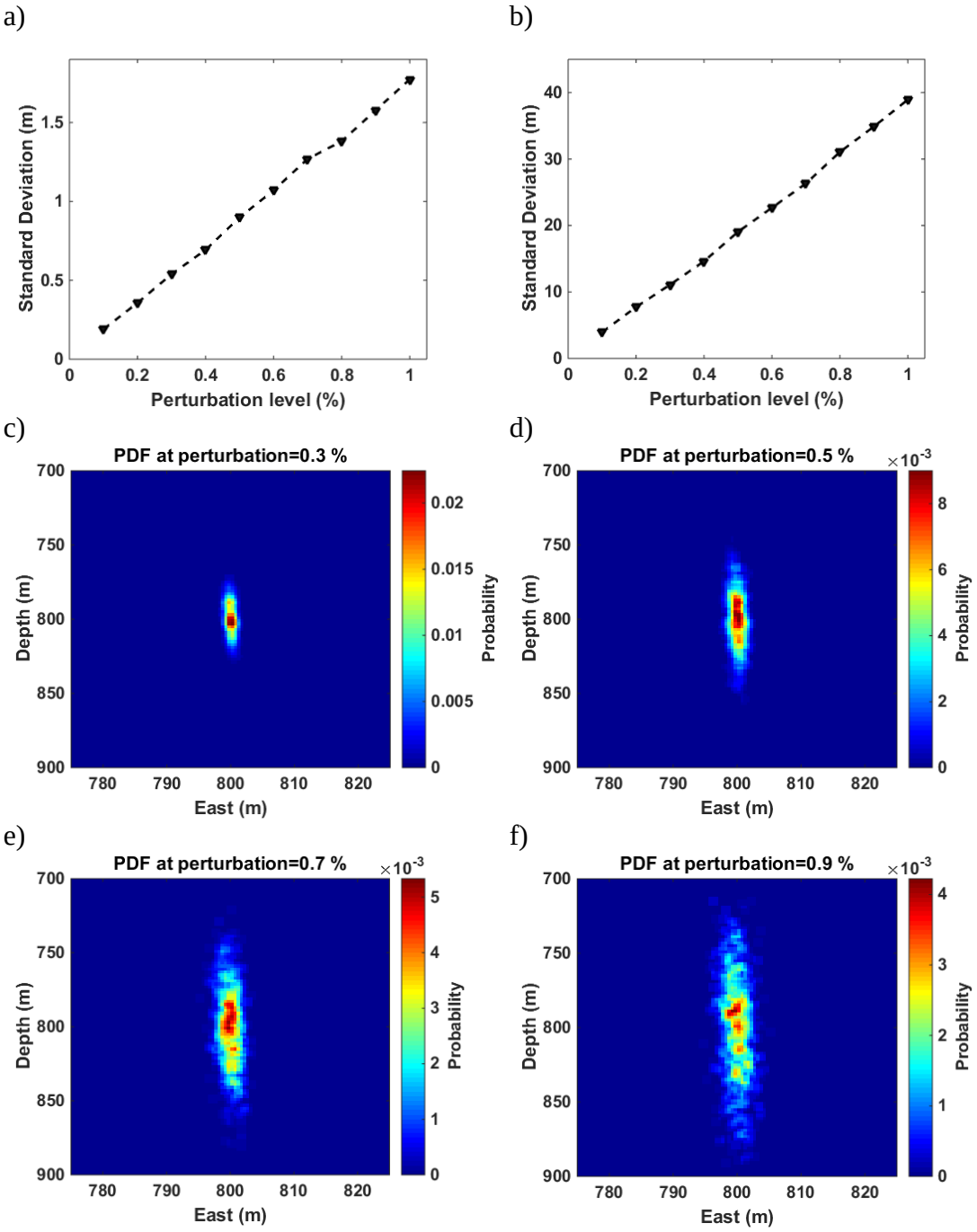

Figure 2.4: Standard deviation of localization error for a) horizontal and b) vertical direction in different perturbation level. PDF for perturbation level of c) 0.3 %, d) 0.5%, e) 0.7 % and f) 0.9 %.

2.4.2. Laterally homogeneous medium

In this example, the performance of the proposed approach is investigated using a horizontally layered model (Figure 2.5a). This horizontally layered model is suitable

for a number of shale gas lithologies, and is similar to that used by Douma et al. (2013). The passive source coordinates x_s and z_s are equal to 800 m and 1500 m, respectively (star in Figure 2.5a). An acoustic finite difference method was used to simulate the passive seismic record. The modelling assumed a Ricker wavelet with the dominant frequency of 30 Hz, 2 ms time sampling and 10 m receiver spacing to generate the synthetic record. Similar to the previous example, a constant time shift of 0.3 s was applied to all modelled traces and perturbed the record with random noise (S/N=2) scaled by equation 2.13. The simulated passive record is shown in Figure 2.5b.

a)

b)

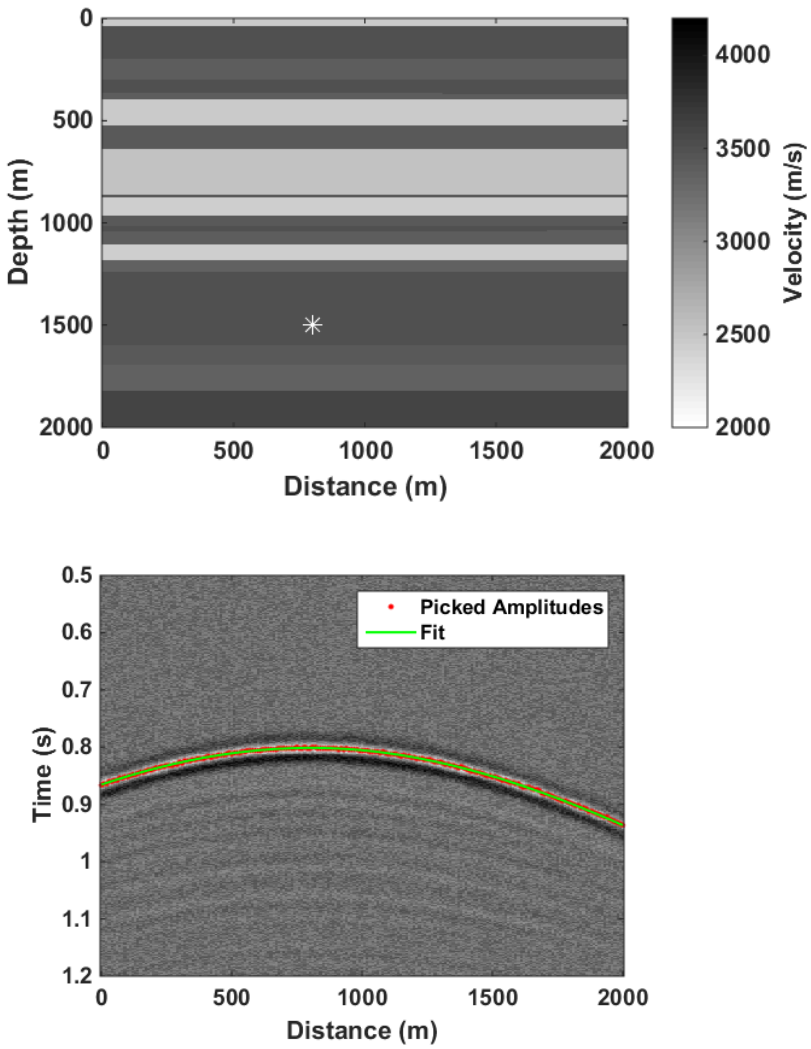

Figure 2.5: a) A horizontally layered P-velocity model and b) the corresponding passive record. Red dots and the green curve express the picked amplitudes and the hyperbolic fit on the picked amplitudes, respectively.

The red dots and green curves represent the picked amplitudes by stack maximization technique used in the previous example and the fit obtained by the least square technique, respectively.

Figure 2.6a-2.6c shows the distributions of the estimated effective velocity (v), origin time (t_0) and the vertical focal coordinate of the passive source (z_s), respectively. It is observed that the estimated values are centered around the true values used in the forward modelling. Table 2.3 shows the final source parameters and effective velocity of the medium derived from the secondary fit of the moveout relationship. The derived source location is within 5 m vertically and 2 m horizontally off the true position.

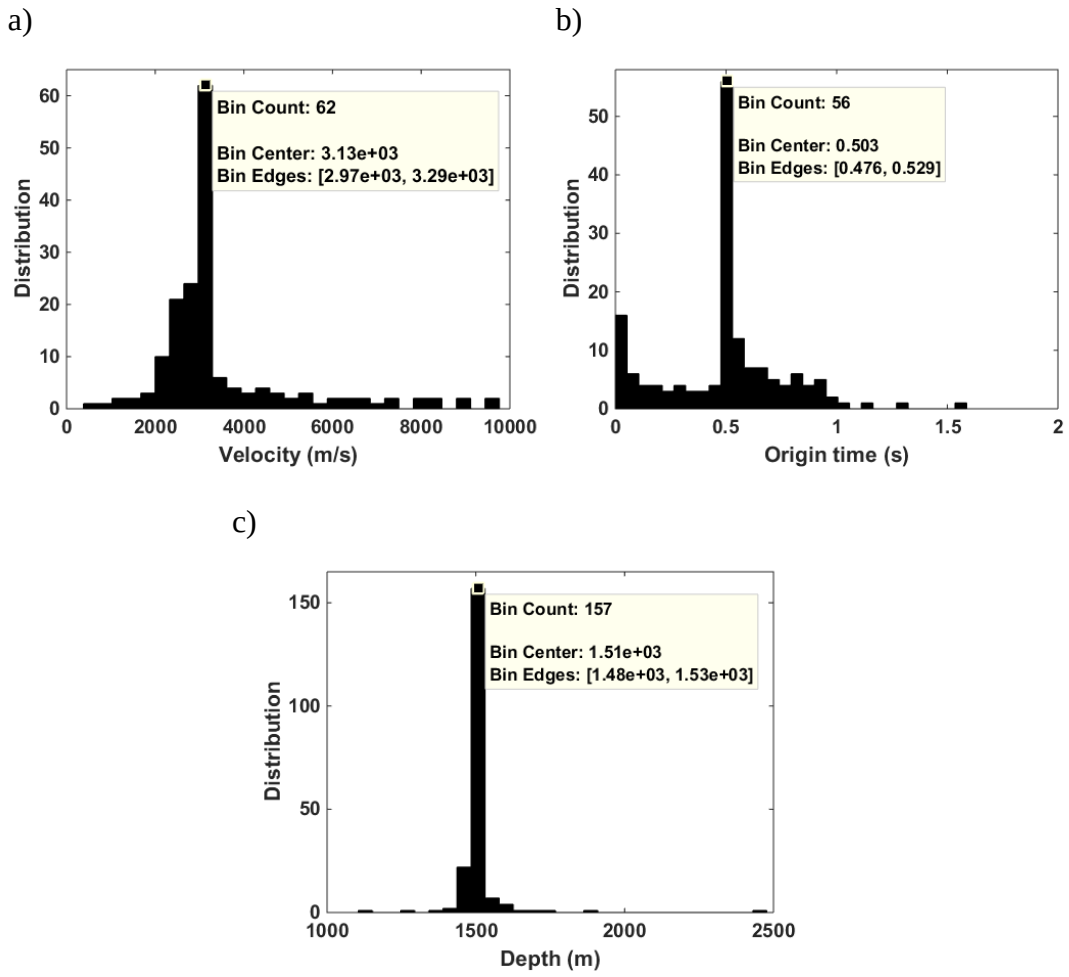

Figure 2.6: Distribution of a) effective P-velocity, b) vertical traveltime and c) vertical focal coordinate of passive source estimated by the application of equations 10-12 for the passive record shown in Figure 2.5b.

To have certain estimates for the monitoring parameters (v, t_0, and z_s), I ran least square fitting using the updated boundaries from the locationing equations 2.10-2.12 (Figures 2.6a-2.6c). The results are shown in Table 2.3. It is seen that the vertical focal coordinate of the passive source (z_s) coincided with the true source position.

S (s)	V (m/s)	t_0 (s)	z_s (m)	x_s (m)
0.3241	3128	0.478	1495	802

Table 2.3: Final inverted coefficients using a non-linear least square fit for the example shown in Figure 2.5.

2.4.3. Laterally inhomogeneous medium

The performance of the proposed technique is further challenged in the presence of lateral velocity variations on the locationing procedure. The input model is the same as that used in the previous section, except that a central interface between 500 m and 1000 m depth has been set to tilt at 10 degrees across the model (Figure 2.7a). The passive seismic source location is kept the same as the previous model presenting a laterally homogeneous model (x_s=800 m, z_s=1500). The corresponding simulated passive record is shown in Figure 2.7b. Picked amplitudes by the stack maximization technique and the fit obtained by least square method are shown by the red dots and the green curve, respectively. The corresponding distributions for source elevation, origin time and effective velocity are given in Figure 2.8, and the final location parameters are provided in Table 2.4. It is noticed that the horizontal error in the location (28 m) is larger than the vertical misfit (14 m), demonstrating the expected sensitivity of the method to lateral velocity variations.

a)

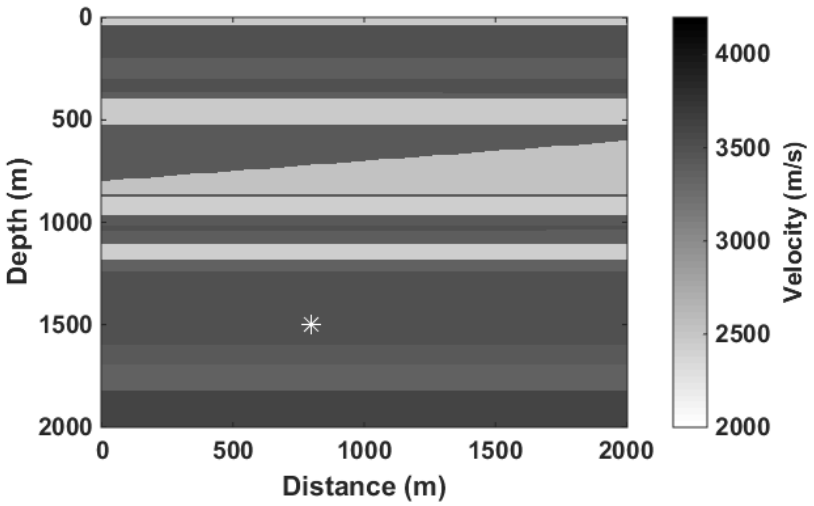

b)

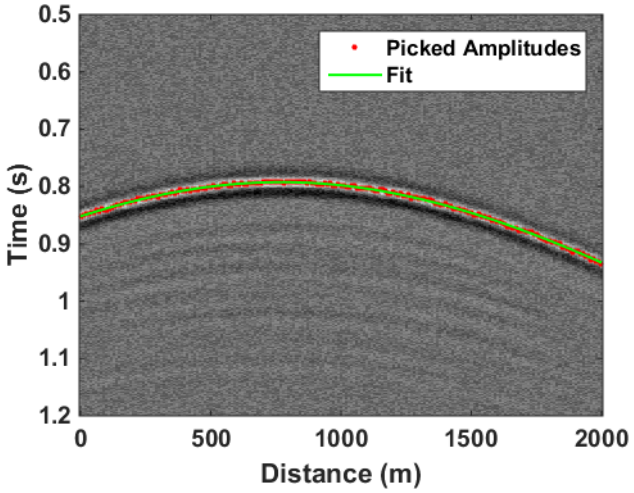

Figure 2.7: a) A P-velocity model with lateral velocity variation and b) the corresponding passive record. Red dots and the green curve express the picked amplitudes and the hyperbolic fit on the picked amplitudes, respectively.

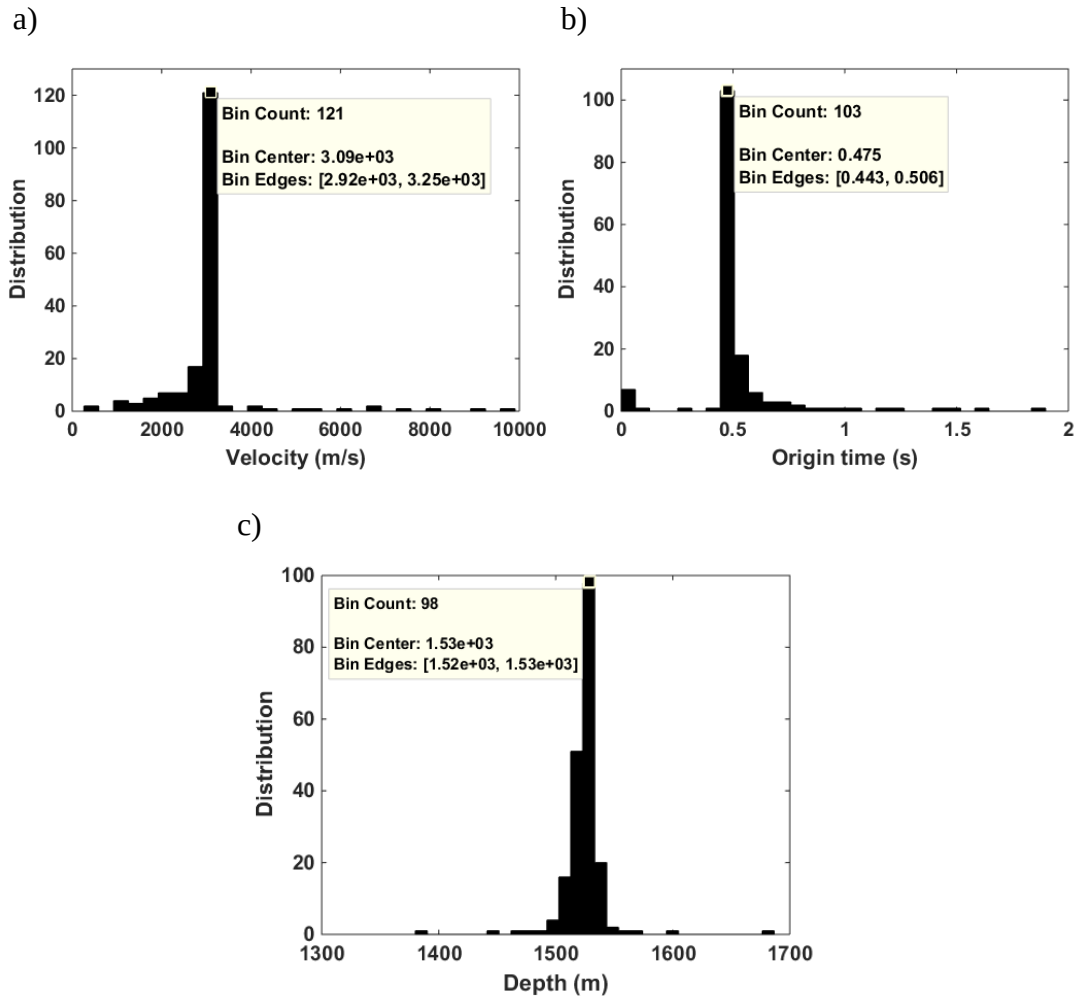

Figure 2.8: Distribution of a) effective P-velocity, b) vertical traveltime and c) vertical focal coordinate of passive source estimated by the application of equations 2.10-2.12 for the passive record shown in Figure 2.7b.

S (s)	V (m/s)	t_0 (s)	z_s (m)	x_s (m)
0.3011	3090	0.49	1514	772

Table 2.4: Final inverted coefficients using a non-linear least square fit for the example shown in Figure 2.7.

2.5. Field data example

The ultimate test for the proposed technique is of course its performance on a field data example. A hydraulic fracturing case study is selected for this purpose. The records were previously used by Chambers et al. (2014). The data was pre-processed using the workflow explained in Chambers et al. (2014). Analogous to the previous examples, arrival times in the field data are determined automatically using a stack maximization algorithm. However, since the data contain P-wave polarity reversals, the stack maximization was applied to the absolute value traces rather than the raw data values.

In 3D monitoring, the proposed technique requires an extra 2D observation line. In other words, the number of 2D lines used for location must be at least 2. The second line is used to estimate the horizontal coordinate of the focal point (epicentre). In the 3D case, vt_0 represents the distance between the focal location of the passive source and the apparent epicentre (Figures 2.9a-2.9b). The coordinates of the apparent epicentres (green dots), and the distance between them and the focal location of the passive source are estimated by the application of the proposed technique. As indicated in Figures 2.9a-2.9b, the actual epicentre is located along the lines that are perpendicular to the 2D observation lines passing through the apparent epicentres (black lines). Figure 2.10 shows the lines that are used in this example.

a)

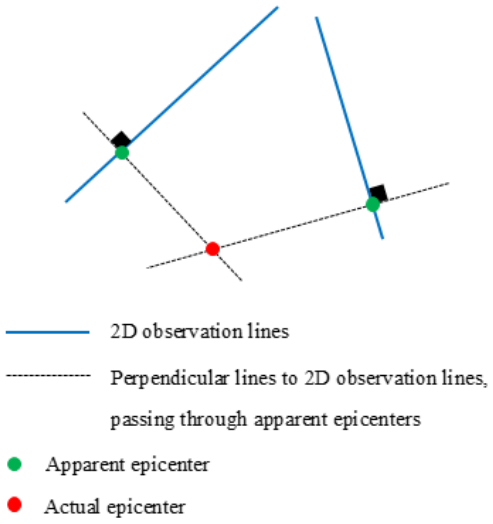

b)

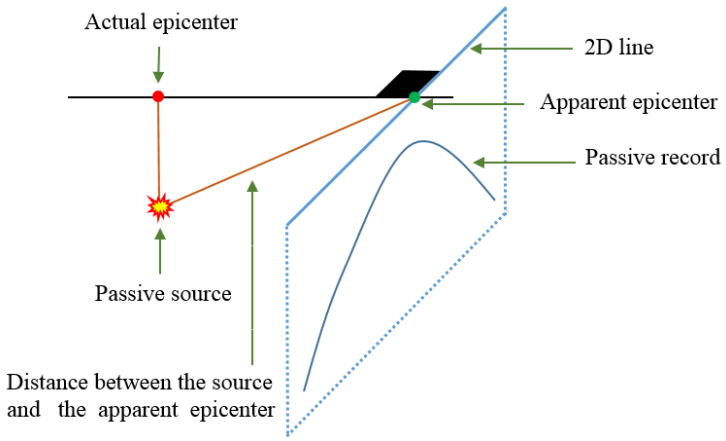

Figure 2.9: a) Top and b) front perspective of observation lines, position of passive source, apparent and actual epicentres.

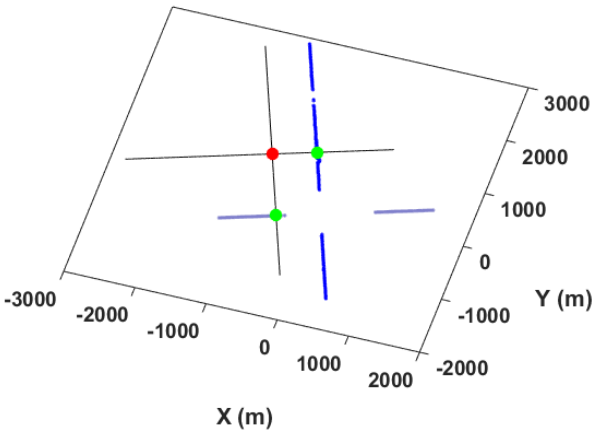

Figure 2.10: Geometry of two observation lines in the 3D survey used in the example.

The estimated coordinates of the apparent epicentres and the estimated horizontal focal position are shown in Table 2.5. Having the coordinates of the epicentre and the estimated distance from apparent epicentres to the focal location of passive source, one can directly estimate the focal depth of the passive source by the straightforward application of the Pythagorean rule. The deviation of the estimated coordinates from that provided by Chambers et al. (2014) for both lines is shown in Table 2.6.

	X (m)	Y (m)
Apparent epicenter of Line 1	-371	1053
Apparent epicenter of Line 2	-565	-204
Derived Epicenter	-942	849

Table 2.5: Estimated coordinates of apparent epicentres and the actual epicentre.

Deviation from Chambers et al. (2014)	
Δx (m)	+14
Δy (m)	+13
Δz (m)	+5

Table 2.6: Deviation of the estimated depth from the provided datum for both 2D lines used for localization.

To assess the uncertainty of the proposed technique in event locationing for the field data, a bootstrapping approach (Efron, 1993) was used. This technique is generally well suited for the experiments that are not repeatable and whose parameters of interest cannot be estimated by analytical means (Sacchi, 1998). The main idea in bootstrapping is that the distribution of a statistic can be reconstructed though repeated computations of the statistic using the data that are randomly selected with replacement from the original population. As it applies to the present work, I begin by computing traveltime residuals by subtracting the initial fitted hyperbola. I then construct 1000 bootstrap datasets by selecting residuals randomly with replacement. For each bootstrap data set, I reconstruct a set of arrival times by adding the fitted hyperbola to the residuals. These arrivals times are then used as input for the location procedure. As such, 1000 potential locations, whose distribution reflects the underlying variation of the arrival times, were computed. This distribution can be further summarized through the computation of standard deviations or confidence intervals.

Figure 2.11a shows the recorded and picked arrival times using a stack maximization algorithm applied to absolute value traces for the 2D line used for locationing (shown by blue dots in Figure 2.10). The blue circles and the red dots represent the picked arrival times and the final fit obtained by the non-linear least square fitting technique, respectively. Figure 2.11b shows the residual arrival time after subtraction of the fitted hyperbola. Figure 2.11c shows one of the bootstrap samples.

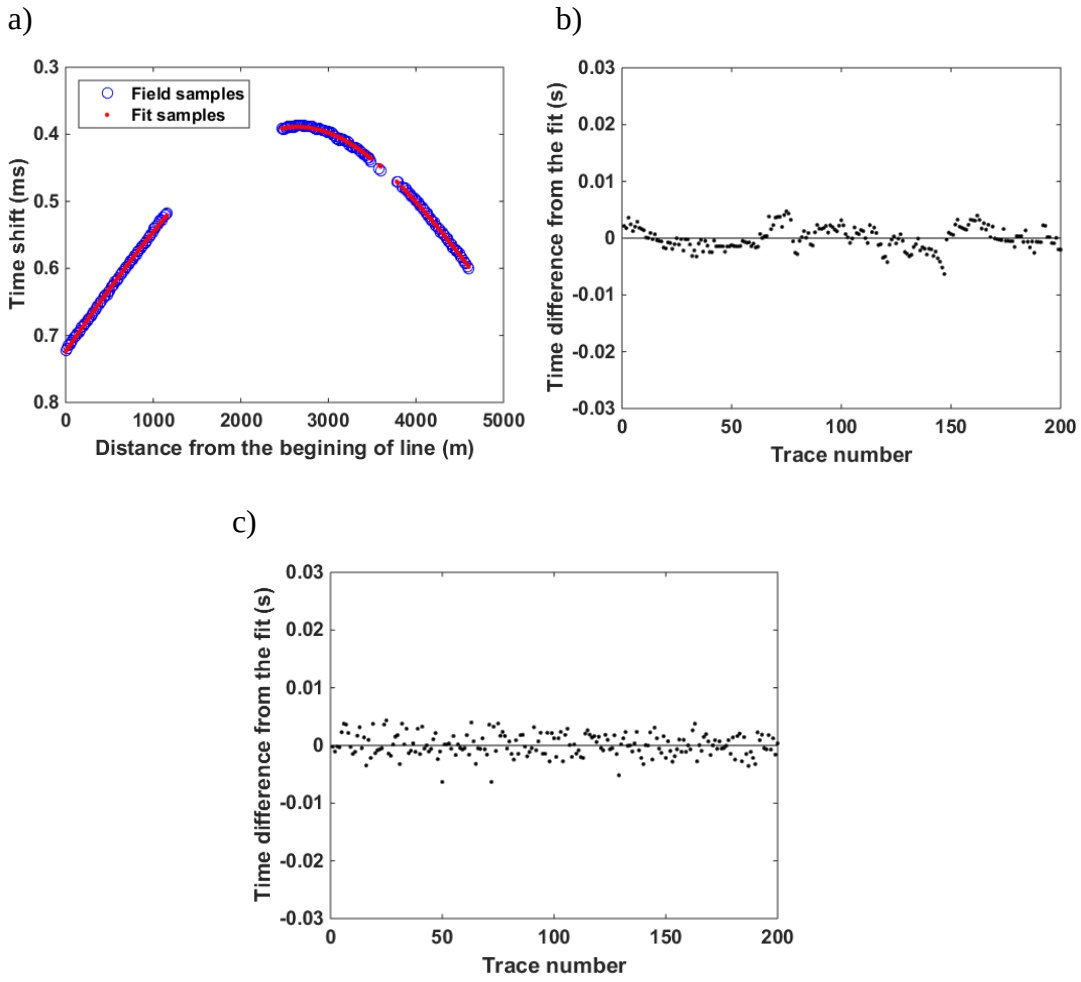

Figure 2.11: a) Comparison between field data samples and the hyperbolic fit, b) moveout corrected data around the fit and c) a bootstrap sample constructed from the original picked samples.

Figure 2.12 shows the results of the bootstrapped uncertainty analysis expressed as a 2D probability-density function (PDF) in the plane of the inline and depth

direction. As is observed, the level of uncertainty, in the 2D plane, is around ± 30 m in the vertical direction and ± 10 m in horizontal direction.

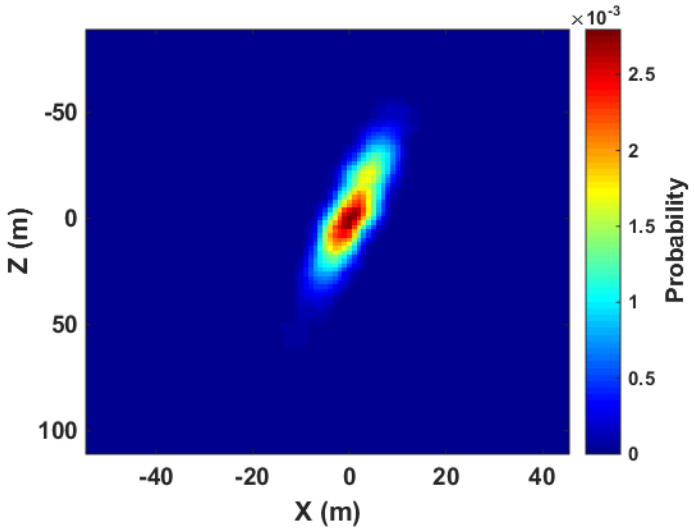

Figure 2.12: Vertical cross-section through PDF around the estimated hypocentre corresponding to the 2D line used for location (Figure 2.11a).

2.6. Discussion

In this study, I have described and applied a procedure for identifying the focal point of a wavefront from a passive seismic source. In the first two synthetic experiments, a constant velocity model and a laterally homogeneous model, the method provides acceptable estimations of focal coordinates of the passive source. Application of the proposed approach to the third synthetic example, a model with lateral velocity variations, showed that the applicability of the proposed technique is limited to horizontally-layered media. Accordingly, some limited knowledge of the size and scale of heterogeneity in an area is required to determine suitability of the method. Such information could be acquired pre-survey from the analysis of the existing bore-holes or 2D active lines in the area of investigation.

For synthetic data examples, it was assumed that the passive records were pre-processed and de-noised. Also, the synthetic sensitivity testing assumed contamination with random noise; however, in practice survey data would be expected to contain noise corresponding to natural and anthropogenic sources which would be correlated between sensors. As such the perturbation analysis can be regarded as a best-case

scenario. It was found that perturbation around true traveltime curve has a greater affect on the precision of the vertical coordinate of the passive seismic source, compared to the horizontal, this is consistent with the previous studies by Eisner et al. (2009) and Mueller (2013). Furthermore, my finding that for perturbation < 0.5 %, the standard deviation passes ±20 m in vertical direction. It may suggests that perturbation of 0.5 % can be defined as the threshold of reliability in the performance of the proposed algorithm; however, it should be noted that this number would be varied if different array geometries or strategies are used for arrival time measurement.

In the analysis of the pre-processed field data example, a small deviation from the previous location was observed. Some variation is to be expected as both techniques contain errors; however, the difference in the derived depths from those obtained by Chambers et al. (2014) is within the grid spacing of the migration operator used in that study (approx. 15 m). As mentioned previously, a single borehole was used to make the velocity model by Chambers et al. (2014), and hence the computed traveltimes follow a hyperbolic trend in their study. That the depth derived in this work corresponds so closely with that of the previous study, provides confirmation that the previous work used a correct estimate of the RMS velocity. Furthermore, that the travel time residuals from the fitted hyperbola solution are less than 0.005s in Figure 2.11b, suggests that in this study area hyperbolic moveout provides an effective representation of the arrival time variations.

An additional complication which arises in microseismic source location compared to reflector mapping is that of the microseismic sources anisotropic radiation pattern. This creates regions with small or zero arrival amplitudes as well as causing polarity reversals in the data. In the present study, it is assumed that these issues are identified and corrected as a part of an effective picking strategy. For example, the stack maximization method utilized absolute value traces; however, in the future other picking techniques such as time-warping (e.g., Burnet and Fomel, 2009b) and event/horizon tracking techniques (e.g., Wu and Hale, 2015), may prove applicable. Additional measure will also be required in cases where arrivals from multiple events intersect, a possibility not allowed for the present formulation.

A notable advantage of the proposed technique is that the focal constraint equations (equations 2.10-2.12) are decoupled from the initial moveout curve that is fit to the arrival times, and could be applied to any moveout relationship which provides the estimates of the minima and gradient of the arrival time. In the cases explored here, a hyperbolic moveout was used for this initial fit in order to smooth the arrival times and provide more robust estimates of local slope information. Hence, one future extension of the presented research is to apply more general descriptions of the moveout trend for the initial fit of the picked arrival times. This may assist in anisotropic settings where non-hyperbolic moveout relationships are required (e.g., Molovichko, 1978; Alkhalifah and Tsvankin, 1995; Fomel and Stovas, 2010).

2.7. Conclusions

In the presented chapter, a surface passive seismic location algorithm proposed. The algorithm does not require a velocity model to be known a priori. The method used local slopes from an initial fit of a moveout equation in order to derive a range of estimates for the source vertical coordinate, origin time and the effective velocity of the medium. These ranges were then used as constraints for a subsequent fit of the moveout relationship which provides the final position and the origin time of the passive seismic source as well as the effective velocity of the medium.

The technique was applied on several synthetic data examples and on a field data set. The results achieved by the application of the proposed technique in a constant velocity model and in a laterally homogeneous examples provided estimates of the source coordinate that were within a small tolerance off the true position. Using another synthetic example, it was shown that the proposed technique is sensitive to situations where there are lateral velocity variations. The technique was also applied to a real data example, finding that the derived location was consistent with the values from a previous study that used a calibrated velocity model form a single borehole. Further development of the proposed approach includes: a) finding/developing robust nonparametric fitting techniques to smooth the picked time arrivals, and b) extending the approach to cases with VTI anisotropy.

2.8. Appendix A

The radius of the curvature of emitted wavefront is derived by the straightforward geometrical principles. Consider the emission ray geometry shown in Figure 2.13. Sine ratio for triangle r_1r_2s is approximately given by

$$\sin\alpha(x) \cong \frac{R'[\alpha(x)-\alpha(x+\Delta x)]}{\Delta x}. \tag{A-1}$$

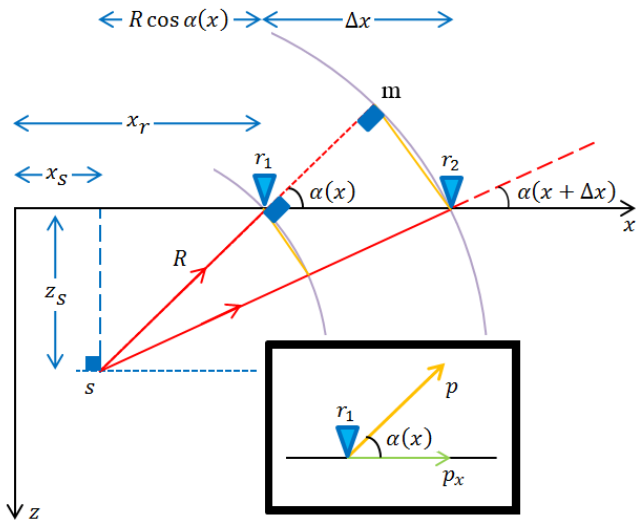

Figure 2.13: Geometry of an emitted wavefront from a passive seismic source.

The limit of the sine function, as Δx approaches to zero, is equal to the differential proportion of the effective emission angle (α) with respect to offset

$$\lim_{\Delta x\to 0}\sin\alpha(x) = R'\frac{d\alpha(x)}{dx} = R\frac{d\alpha(x)}{dx}. \tag{A-2}$$

One can rearrange equation A-2, to obtain the radius (R) in terms of the sine and the derivative of the derivative of emission angle with respect to offset

$$R = R' = -\frac{\sin\alpha(x)}{\frac{d\alpha}{dx}}. \tag{A-3}$$

The trigonometric connections between the effective emission angle (α), the effective slowness (p) and the effective slope (p_x) were given by equations 2.5 and 2.6. Re-arranging equation 2.3 and differentiating the angle with respect to offset gives the derivative of the angle in terms of local slope (p_x), second derivative (p_x') and the effective slowness (p) gives

$$\frac{d\alpha}{dx} = \frac{d}{dx}\left(arc\cos\frac{p_x}{p}\right) = -\frac{{p_x}'}{p\sqrt{1-\left(\frac{p_x}{p}\right)^2}}, \tag{A-4}$$

$$R = \frac{p^2-{p_x}^2}{p{p_x}'}. \tag{A-5}$$

2.9. Appendix B

One can also express the projection of the radius of the curvature of emitted wavefront in both horizontal and vertical directions, from equations 2.2 and 2.3, using a combination of derivatives of the effective slowness. By combining 2.2, 2.3, and A-5 I obtained

$$Rcos\,\alpha(x) = \frac{p^2p_x-{p_x}^3}{p^2{p_x}'}, \tag{B-1}$$

and

$$Rsin\,\alpha(x) = \frac{p^2-{p_x}^2}{p{p_x}'}\sqrt{1-\left(\frac{p_x}{p}\right)^2}. \tag{B-2}$$

However, these expressions still depend upon the unknown effective slowness, p. Here, I derived the projections in terms of first, second and the third derivatives of arrival time with respect to the position of receivers.

I begin with the expressions for the focal point coordinates (x_s , z_s) in equations 2.2 and 2.3. Differentiation of equation 2.2 with respect to offset leads to

$$\frac{d}{dx}\left(Rcos(\alpha)\right) = 1. \tag{B-3}$$

Substitution of equations 2.5 and A-5 in B-3 gives

$$\frac{d}{dx}\left(\frac{p_x}{{p_x}'}\left(1-\frac{{p_x}^2}{p^2}\right)\right) = 1. \tag{B-4}$$

Operating the differentiation in equation A-4 yields

$$\left(\frac{{p_x}'^2-p_x{p_x}''}{{p_x}'^2}\right)\left(1-\frac{{p_x}^2}{p^2}\right)-\frac{2{p_x}^2}{p^2} = 1. \tag{B-5}$$

Finally, substitution of the effective slowness from B-1 into B-5 and simplifying provide the horizontal projections expressed in equations 2.2

$$Rcos(\alpha) = \frac{3p_x p_x'}{3{p_x'}^2 - p_x p_x''}.$$

Differentiation of equation 2.3 with respect to offset and repeating the same steps (B-3 to B-5), provides the vertical projection in terms of the derivatives

$$Rsin(\alpha) = \sqrt{\left(\frac{p_x}{p_x'}\right)^2 - 3\frac{p_x}{p_x''}}\left(\frac{3{p_x'}^2}{p_x p_x'' - 3{p_x'}^2}\right)^{\frac{3}{2}}.$$

2.10. References

Alkhalifah, T., and I. Tsvankin, 1995, Velocity analysis for transversely isotropic media: Geophysics, **60**, 1550–66.

Anikiev, D., F. Staněk, J. Valenta, and L. Eisner, 2013, Imaging microseismic events by diffraction stacking with moment tensor inversion: 83rd Annual International Meeting, SEG, Expanded Abstracts, 2013–2018.

Bancroft, J. C., and X. Du, 2005, Circular Wavefront Assumptions for Gridded Traveltime Computations: CREWES Report, **17**.

----------, 2007, Traveltime Computations for Locating the Source of Micro Seismic Events and for Forming Gridded Traveltime Maps: 69th Conference and Exhibition, EAGE, Extended Abstracts, P332.

Bancroft, J. C., 2010, Estimating an accurate RMS velocity for locating a microseismic event: GeoCanada, Working with the Earth, 1-4.

Bóna, A., 2011. Shot-gather time migration of planar reflectors without velocity model: Geophysics, **76**, no. 2, S93–S101.

Burnett, W., and S. Fomel, 2009b, Moveout analysis by time-warping: 79th Annual International Meeting, SEG, Expanded Abstracts, **28**, 3710–3714.

Casasanta, L., and S. Fomel, 2011, Velocity-independent τ-p moveout in a horizontally layered VTI medium: Geophysics, **76**, no. 4, U45-U47.

Cooke, D., A. Bóna, and B. Hansen, 2009, Simultaneous time imaging, velocity estimation and multiple suppression using local event slopes: Geophysics, **74**, no. 6, WCA65–WCA73.

Chambers, K., J. M. Kendall, S. Brandsberg-Dahl, and J. Rueda, 2010a, Testing the ability of surface arrays to monitor microseismic activity: Geophysical Prospecting, **58**, no. 5, 821– 830.

Chambers, K., J. M. Kendall, and O. Barkved, 2010b, Investigation of induced microseismicity at Valhall using the Life of Field Seismic array: The Leading Edge, **29**, no. 3, 290-295.

Chambers, K., B. D. Dando, G. A. Jones, R. Velasco, and S. A. Wilson, 2014, Moment tensor migration imaging: Geophysical Prospecting, **62**, no. 4, 879-896.

Douma, J., R. Snieder, A. Fish, P. Sava, 2013, Locating a microseismic event using deconvolution: 83rd Annual International Meeting, SEG, Expanded Abstracts, 2206-2211.

Duncan, P. M., and L. Eisner, 2010, Reservoir characterization using surface microseismic monitoring: Geophysics, **75**, no. 5, A139–A146.

Efron, B., and R. Tibshirani, 1993, An introduction to the bootstrap method: Chapman and Hall.

Eisner, L., P. M. Duncan, W. M. Heigl, and W. R. Keller, 2009, Uncertainties in passive seismic monitoring: The Leading Edge, **28**, 648–655, doi: 10.1190/1.3148403.

Eisner, L., A. De La Pena, S. Wessels, W. Barker, and W. Heigl, 2011, Why surface monitoring of microseismic events works: EAGE Third Passive Workshop in Athens.

Fomel, S., 2007, Velocity-independent time-domain seismic imaging using local event slopes: Geophysics, **72**, no. 3, S139–S147, doi: 10.1190/1.2714047.

Fomel, S., and A. Stovas, 2010, The generalized non-hyperbolic moveout approximation: Geophysics **75**, no. 2, U9–U18.

Fomel, S., 2014, Recent advances in time-domain seismic imaging: 84th Annual International Meeting, SEG, Expanded Abstracts, 4400–4404.

Gei, D., L. Eisner, and P. Suhadolc, 2011, Feasibility of estimating vertical transverse isotropy from microseismic data recorded by surface monitoring arrays: Geophysics, **76**, no.6, WC117-WC126.

Glogovsky, V., E. Landa, S. Langman, and T. Moser, 2009, Validating the velocity model: The Hamburg score: First Break, **27**, no. 3, 77–85.

Khoshnavaz, M. J., K. Chambers, A. Bóna, and M. Urosevic, 2015, Passive Seismic Localization Without Velocity Model: Application and Uncertainty Analysis. 85th Annual International Meeting, SEG, Expanded Abstracts, 2467-2472.

Maxwell, S., J. Rutledge, R. Jones, and M. Fehler, 2010, Petroleum reservoir characterization using downhole microseismic monitoring: Geophysics, **75**, no. 5, A129–A137.

Mikula, P., D. Heal, and M. Hudyma, 2008, Generic seismic risk management plan for underground hard rock mines, Technical Report, Australian Centre for Geomechanics.

Mokaramian, A., and V. Rasouli, 2013, Coiled Tube Turbo drilling: A proposed technology to optimise drilling deep hard rocks for mineral exploration: International Journal of Mining and Mineral Engineering, **4**, no. 3, 224-248,

Malovichko, A. A., 1978, A new representation of the traveltime curve of reflected waves in horizontally layered media: Applied Geophysics in Russian, **91**, 47–53 (translation provided by Sword 1987a).

Mueller, M., 2013, Meeting the challenge of uncertainty in surface microseismic monitoring: First Break, **31**, no. 7, 89-95.

Ottolini, R., 1983, Velocity independent seismic imaging: Stanford Exploration Project, 37, 59–68.

Pavlis, G., 1986, Appraising earthquake hypocenter locations errors; a complete practical approach for single event locations: Bulletin of the Seismological Society of America, **76**, no. 6, 1699–1717.

Ronen, J., and J. F. Claerbout, 1985, Surface-consistent residual statics estimation by stack-power maximization: Geophysics, **50**, no. 12, 2759-2767.

Sacchi, M. D., 1998, A bootstrap procedure for high-resolution velocity analysis: Geophysics, **63**, no. 5, 1716–1725, doi:10.1190/1.1444467.

Stovas, A., and S. Fomel, 2016, Mapping of moveout attributes using local slopes: Geophysical prospecting, **64**, no. 1, 31-37, doi: 10.1111/1365-2478.12284.

Sun, B., A. Bóna, A. King, and B. Zhou, 2015, A comparison of coherency measurement using semblance and multiple signal classification, from a seismic-while-drilling perspective: Geophysics, **80**, no. 3, KS27-KS39.

Vidale, J.,1988, Finite-difference calculation of travel times: Bulletin of the Seismological Society of America, **78**, no. 6, 2062-2076.

Wu, X. and D. Hale, 2015, Horizon volumes with interpreted constraints: Geophysics, **80**, no. 2, IM21-IM33.

Yilmaz, Ö., 2000, Seismic data analysis: SEG.

3. Oriented estimation of kinematic attributes in vertical-transverse-isotropy media using local slopes and predictive painting

3.1. Overview

A good seismic velocity model is required for many routine seismic imaging techniques. Velocity model building from seismic data is often labour-intensive and time-consuming, particularly if the geology is complex. The process becomes more complicated by taking non-hyperbolic traveltime estimations into account, where more than a single parameter is required for non-hyperbolic moveout approximations. An alternative to the conventional time-domain seismic imaging algorithms is to use techniques developed based on the local event slopes, which contain sufficient information of the traveltime moveout for velocity estimation and also about the subsurface geological structures. Given the local slopes, there is no need for a prior knowledge of a velocity model. That is why the term oriented/velocity-less is commonly used for such techniques. Previous methodologies suffered from instability due to high order differentiation of traveltime with respect to offset. This research overcome this problem by reducing the order of differentiation from the kinematic attributes (e.g., anisotropy anellipticity coefficient η) and hence providing more stable solution for horizontally layered vertical-transverse-isotropy (VTI) media. These kinematic attributes are derived in terms of the local event slopes and vertical two-way-travel-time (TWTT). Use of predictive painting, which keeps all the attributes independent from the higher order derivatives, is proposed to estimate the vertical TWTT.

The theoretical contents and the performance of the proposed approach are demonstrated to both synthetic and field data examples. The accuracy of moveout attributes for shifted hyperbola, rational, three-parameter and acceleration approximations is also studied and compared on the synthetic example. The results show that regardless of the approximation types, normal moveout (NMO) velocity has

the highest accuracy while the non-hyperbolic attribute is less accurate. Computational time and accuracy in the inversion of the kinematic attributes in VTI media using the proposed approach are compared with routine/conventional multi-parameter semblance inversion and with the previous velocity-independent inversion techniques.

3.2. Introduction

Accurate seismic velocity fields are required for accurate seismic imaging. The model is often built through velocity analysis from seismic data. This is still one of the most critical stages in seismic data processing (Yilmaz, 2001) and the velocity errors influence the accuracy of the final image. The routine velocity analysis methods (e.g., constant velocity stack and semblance), are generally labour-intensive and time-consuming. An experienced processor is required to pick the proper velocities in the velocity spectrum. Velocity analysis is often more time-consuming by taking the anisotropy and/or lateral inhomogeneity into account, when more than a single parameter is required for non-hyperbolic moveout approximations (Alkhalifah and Tsvankin, 1995).

Oriented/velocity-independent time-domain seismic imaging using local event slopes is an alternative to the routine imaging workflows. Local slopes represent the apparent ray parameter or apparent slowness in a seismic record. They carry information of the local traveltime moveout that is defined by the subsurface geological structures (Fomel, 2007a). Over the past 80 years, many advances have been done in oriented seismic imaging. The idea of using local slops from prestack data goes back to the works done by Rieber (1936) and Riabinkin (1957). Ottolini (1983) derived the migration velocity for each point in the registered seismic data in order to apply it on his velocity-independent migration algorithm for horizontal interfaces. Fomel (2007a) generalized this idea by developing analytical velocity-independent techniques to transform seismic data from prestack domain to the image domain for different time-domain seismic imaging operators. Cooke et al. (2009) further developed a local slope based prestack time migration technique and used the oriented migration velocities to remove multiples. Bóna (2011) developed another oriented/velocity-independent prestack time migration technique for planar reflectors

in common-source domain. He used the local slopes and the second derivatives of two-way-travel-time (TWTT) with respect to offset. All these techniques are developed based on the time-domain seismic imaging assumption of hyperbolic traveltime moveout.

Direct use of local slopes in the estimation of interval velocity for anisotropic media with polar anisotropy (VTI) was proposed by Fowler et al. (2008). Velocity-independent time-domain seismic imaging was extended to anisotropic medium by Burnett and Fomel (2009a, 2009b). Their technique is designed for 3D elliptically anisotropic media. Casasanta and Fomel (2011) developed another velocity-independent time-domain imaging technique for VTI medium in the slant-stack (τ-p) domain. Stovas and Fomel (2016) proposed the use of local slopes to obtain kinematic attributes, including NMO velocity, anisotropy anellipticity coefficient (η) and zero-offset TWTT, for different non-hyperbolic approximations. These include shifted hyperbola approximation (Malovichko 1978; de Bazelaire 1988; Castle 1994), rational non-hyperbolic approximation (Alkhalifah and Tsvankin, 1995) and generalized moveout approximation (Fomel and Stovas, 2010). To find the parameters describing the different moveout approximations, Stovas and Fomel (2016) proposed to estimate the curvature of the wavefront, or equivalently the second derivative of the traveltime with respect to offset; however, the curvature estimation is very difficult to achieve with the required accuracy. The difficulties are described in the Discussion section of this chapter.

To avoid the curvature estimation, this research further developed the analysis done by Stovas and Fomel (2016) and derived the kinematic attributes, inhomogeneity parameter and NMO velocity, in terms of local slopes and zero-offset TWTTs for different non-hyperbolic approximations, including shifted-hyperbola (Malovichko 1978; de Bazelaire 1988; Castle 1994), rational (Alkhalifah and Tsvankin, 1995), three-parameter (Blias, 2009), and acceleration approximations (Taner et al., 2005). For rational approximation, the expressions derived by Stovas and Fomel (2016) is used in this research. Here, curvature estimation is replaced by the estimation of zero-offset TWTTs using predictive painting approach (Fomel, 2010); therefore, all kinematic attributes stay independent curvature independent.

Since the generalized moveout approximation requires more parameters than the other approximations, Stovas and Fomel (2016) proposed to use a two-point-to-point mapping technique where the slopes and curvatures are computed at two points on the same wavefront; however, having the zero-offset TWTT of the wavefront, it is possible to use a one-point-to-point scanning similar to the approach I proposed for other approximations in this chapter.

To show the applicability of the proposed approach to the various approximations, I compare the accuracy of the estimated moveout attributes on a synthetic multilayered VTI CMP gather. Regardless of the approximation type, NMO velocity has the highest accuracy while non-hyperbolic attribute (η) is less accurate. Similar to the observations of Asgharzadeh et al. (2014), I find that among the tested approximations the rational approximation has the highest accuracy, while approximation of Taner et al. (2005) has the lowest. Computational time and accuracy in the inversion of kinematic attributes in VTI media using the proposed approach are compared with routine/conventional multi-parameter semblance inversion and with the previous velocity-independent inversion techniques. In order to estimate the local event slopes, I used plane wave destructor technique (Fomel, 2002) available in Madagascar Open-Source multidimensional data analysis package (Fomel et al., 2013).

3.3. Predictive painting

The main concept of predictive painting is to predict each seismic event from its neighbours, which is shifted along the event local slopes (Fomel, 2010). Local slopes are often estimated by measuring the time difference or time shift between two points carrying by a seismic wavefront. Given the local slopes, one can implement an inverse process to find the time shift between two neighbouring traces.

Figure 3.1 shows a typical seismic event that can be either hyperbolic or non-hyperbolic. The event can be located in any seismic domain (e.g., CMP or common-source domain). Consider a sample located at trace number i with the TWTT of t_i.

Finding the TWTT of the seismic event at trace number *i-n* is desired. The first step is to predict the TWTT of the event at the trace number *i-1*. It is done by defining a predictive operator, which is in terms of the local slope (*p*) between the two samples. Δt and Δx denote the sampling interval and receiver spacing, respectively. The slope is shown by the red line in Figure 3.1.

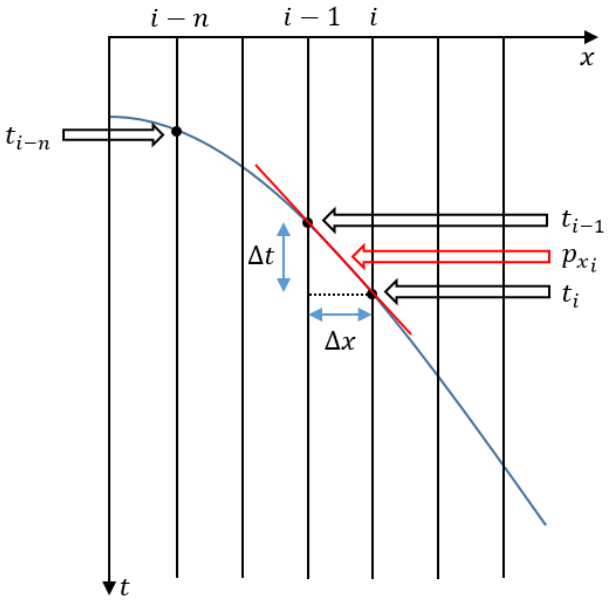

Figure 3.1: Predictive panting of a seismic event using local event slopes

The tangent of the angle between the slope and the horizontal dashed line determines the predictive operators

$$\tan\gamma = p_{x_i} = \frac{\Delta t}{\Delta x} = \frac{t_i - t_{i-1}}{\Delta x}, \tag{3.1}$$

$$t_{i-1} = t_i - p_{x_i}\Delta x. \tag{3.2}$$

Writing and repeating the above operator until the desired trace (*i-n*), summation and simplification of the results gives the general predictive operator that is given by

$$t_{i-n} = t_i - \left(\sum_{k=0}^{n-1} p_{x_{i-k}}\right)\Delta x. \tag{3.3}$$

For vertical TWTT, the predictive operator corresponds to

$$t_{0i} = t_i - \left(\sum_{k=0}^{n-1} p_{x_{i-k}}\right)\Delta x. \tag{3.4}$$

In this case, *n* denotes the trace number difference between the zero-offset trace and the i^{th} trace. This velocity-independent moveout equation remains the same for all hyperbolic and non-hyperbolic events.

3.4. Kinematic attribute estimation

3.4.1. Shifted hyperbola approximation

Shifted hyperbola approximation (Malovichko 1978; de Bazelaire 1988; Castle 1994) is one of the popular moveout approximations for approximating non-hyperbolic moveouts and is given by

$$t \cong t_0 \left(1 - \frac{1}{s}\right) + \frac{1}{s}\sqrt{{t_0}^2 + \frac{sx^2}{v^2}}, \tag{3.5}$$

where *t*, t_0 and *v* denote TWTT, vertical TWTT and the NMO velocity, respectively. Parameter *s* is related to anisotropy and/or heterogeneity of seismic structures and velocities. Differentiation of equation 3.5 gives the local event slope (*p*)

$$p = \frac{x}{v^2\sqrt{{t_0}^2 + \frac{sx^2}{v^2}}}. \tag{3.6}$$

Equations 3.5 and 3.6 construct a system of equations with two unknown variables, *s* and *v*. Solution of the system gives *s* and *v* in terms of zero-offset TWTT and the local slopes

$$s = -\frac{t_0(xp - 2t + 2t_0)}{(t - t_0)(xp - t + t_0)}, \tag{3.7}$$

$$v^2 = \frac{x(xp - t + t_0)}{t_0 p(t - t_0)}. \tag{3.8}$$

Golikov and Stovas (2012) rearranged different moveout approximations in terms of η for VTI medium. For shifted hyperbola approximation, η is expressed by

$$\eta = \frac{s-1}{8}. \tag{3.9}$$

3.4.2. Rational approximation

Rational moveout approximation (Alkhalifah and Tsvankin, 1995), has the form of

$$t^2 \cong {t_0}^2 + \frac{x^2}{v^2} - \frac{2\eta x^4}{v^4 {t_0}^2\left[1+(1+2\eta)\frac{x^2}{v^2 {t_0}^2}\right]}. \tag{3.10}$$

Kinematic attributes derived by Stovas and Fomel (2016) are given by

$$\eta = \frac{{t_0}^2\left(1+R^2\right)\left(t^2-{t_0}^2-pxt\right)}{2R^2\left(t^2-{t_0}^2\right)^2}, \tag{3.11}$$

$$v^2 = \frac{Rx^2}{{t_0}^2}, \tag{3.12}$$

where

$$R = \frac{pxt{t_0}^2+t_0\sqrt{(pxtt_0)^2-4\left(t^2-{t_0}^2\right)^2\left(t^2-{t_0}^2-pxt\right)}}{2\left(t^2-{t_0}^2\right)^2}. \tag{3.13}$$

In their technique, zero-offset TWTT that is in terms of the wavefront curvature or the second derivative of TWTT with respect to offset, must first be estimated in order to estimate the other kinematic attributes. It is done by solving a complicated quadratic equation for ${t_0}^2$. This need is replaced by the estimation of the zero-offset TWTT using predictive painting in this chapter.

3.4.3. Three-parameter approximation

Blias (2007, 2009), introduced several three-parameter non-hyperbolic moveout approximations for inhomogeneous medium. I formulated all of them in terms of local slopes and zero-offset TWTT. For summarization, his second approximation is included in this work. The moveout approximation is expressed by

$$t^2 \cong \frac{{t_0}^2}{2} + \frac{x^2}{v^2} + \frac{1}{2}\sqrt{{t_0}^4 + \frac{2Ax^4}{v^4}}, \tag{3.14}$$

where *A* defines the inhomogeneity. The kinematic attributes are derived by a similar analysis to shifted hyperbola approximation. The attributes are given by the following equations

$$A = \frac{2(2tpxc-1)\left(2bc-x^2\right)}{x^2}, \tag{3.15}$$

$$v^2 = 2x^2c, \tag{3.16}$$

where

$$b = t^2 - \frac{{t_0}^2}{2}, \tag{3.17}$$

$$c = \frac{2(ptx - t^2) + {t_0}^2}{4(ptbx - t^4 + t^2{t_0}^2)}. \tag{3.18}$$

Based the reformulation of the moveout approximation by Golikov and Stovas (2012), η is explained by

$$\eta = -\frac{A}{4}. \tag{3.19}$$

3.4.4. Acceleration approximation

Increase of velocity with offset is interpreted as acceleration by Taner et al. (2005, 2007). They provided two non-hyperbolic moveout approximations by adding an extra term (acceleration) to the classic NMO equation. The accuracy of the proposed approximations are comparable with three-parameter non-hyperbolic approximations (Golikov and Stovas, 2012). The second moveout approximation from Taner et al. (2005) is expressed by

$$t^2 \cong {t_0}^2 + \frac{x^2}{v^2\left(1 + \frac{2\eta x^2}{v^2{t_0}^2}\right)}. \tag{3.20}$$

Following a similar analysis to the previous part, the kinematic attributes are derived and expressed by

$$\eta = -\frac{1}{2}\,\frac{{t_0}^2\left(ptx + {t_0}^2 - t^2\right)}{\left({t_0}^2 - t^2\right)^2}, \tag{3.21}$$

$$v^2 = \frac{ptx^3}{\left({t_0}^2 - t^2\right)^2}. \tag{3.22}$$

3.5. Application to a synthetic data example

In this example, the proposed inversion technique is applied to a synthetic CMP gather from a horizontally layered model including 12 VTI layers. NMO-velocities increase linearly with depth/time with the range of 1800-2300 m/s and the effective inhomogeneity parameter (η) varies between 0.04-0.16 (Table 3.1).

Interface	V_{NMO} (m/s)	η
1	1800	0.04
2	1850	0.071
3	1900	0.062
4	1950	0.093
5	2000	0.084
6	2050	0.115
7	2100	0.106
8	2150	0.137
9	2200	0.128
10	2250	0.159
11	2300	0.15

Table 3.1: NMO velocities and inhomogeneity parameters (η) used in forward modelling to generate the VTI anisotropic CMP gather shown in Figure 3.2b.

Figures 3.2a-3.2c show the zero-offset isotropic CMP gather, zero-offset anisotropic CMP gather and the amplitude difference between them, respectively. The traveltimes used to generate the gather were computed from effective VTI ray velocities corresponding to the given ηs following a similar approach described in Bóna et al. (2008). Figures 3.2d-3.2e show the local event slopes and zero-offset TWTTs estimated by plane wave destructor and predictive painting in Madagascar Open-Source multidimensional data analysis package (Fomel et al., 2013). Figure 3.2f shows the result of flattening of the anisotropic gather shown in Figure 3.2b by the application of the predictive painting technique. It is seen that the anisotropic data is well flattened.

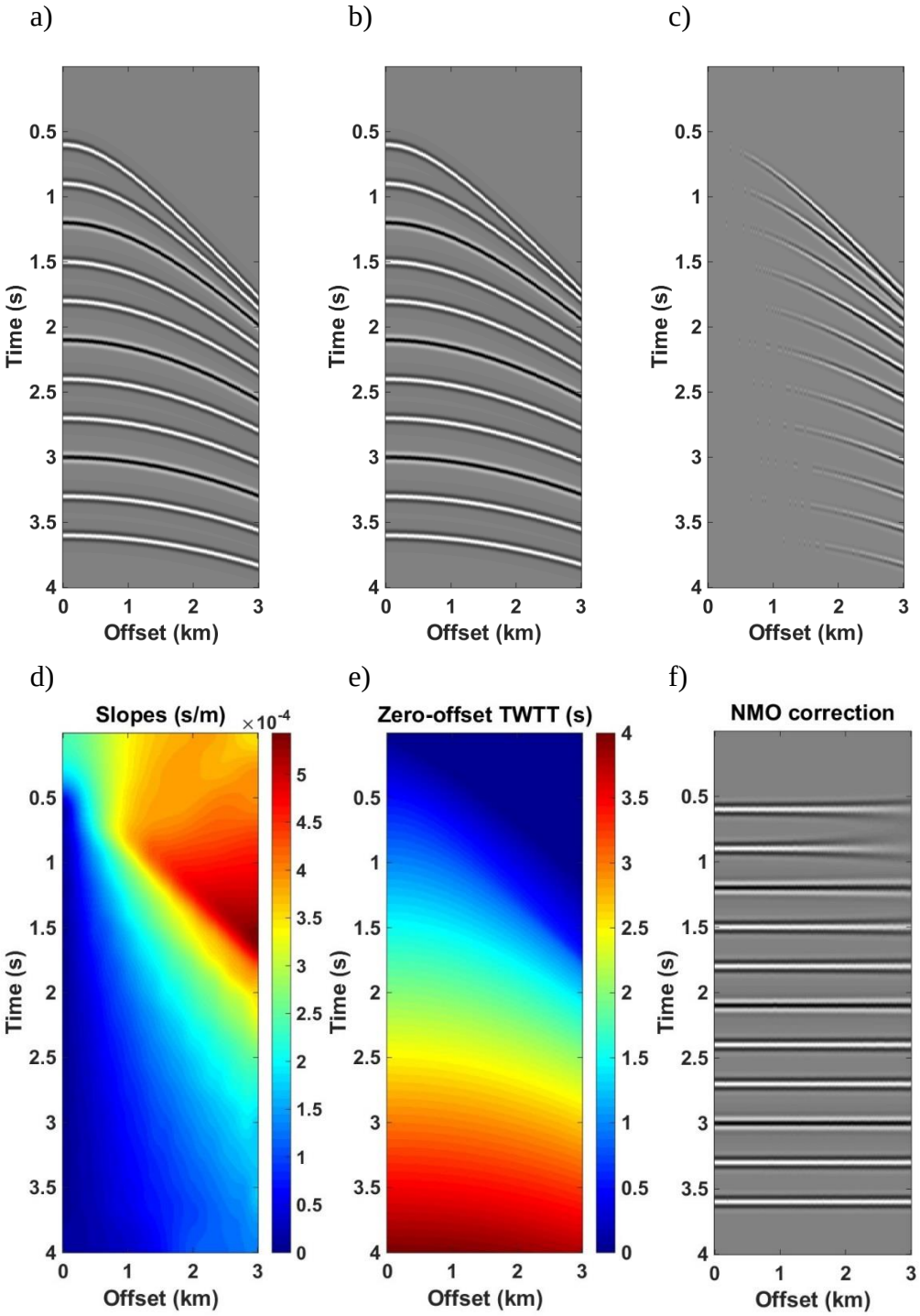

Figure 3.2: Generated a) isotropic and b) anisotropic CMP gather based on the kinematic attributes expressed in Table 3.1, c) the amplitude difference between the isotropic and anisotropic CMP gathers, d) local event slopes estimated by plane wave destructor, e) zero-offset TWTTs by predictive painting, and f) flattened data using the estimated zero-offset TWTT for the anisotropic CMP gather.

To quantify the accuracy of the predicted TWTTs, including the zero-offset TWTT, the exact TWTT curve at interface 5 obtained by forward modelling is compared with its corresponding predicted TWTT in Figure 3.3. Predicted TWTT is obtained by the subtraction of TWTT index in each point and the corresponding zero offset TWTT. This procedure is also known as time-warping. The standard error around the exact curve is less than 0.1% in this example.

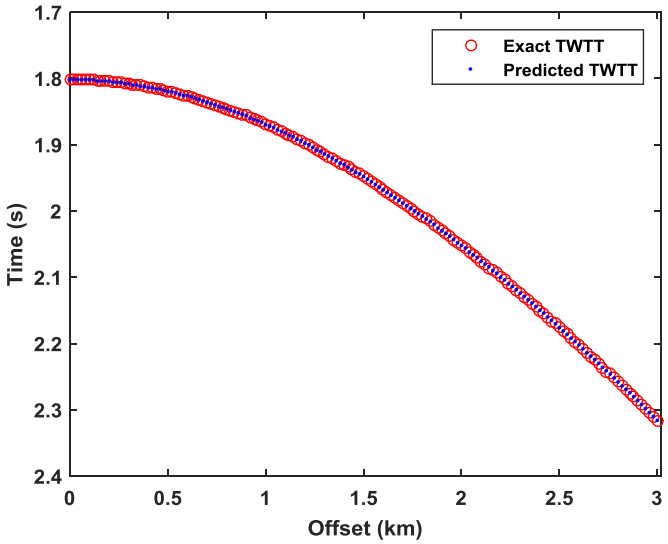

Figure 3.3: Comparison between the exact arrival times and the predicted arrival times for interface 5 of the model expressed in Table 3.1 and Figure 3.2b.

In the next step, the estimated local slopes and zero-offset TWTTs are used to measure the anisotropy anellipticity coefficient (η) and NMO velocity from the above approximations. Figures 3.4a-3.4d and 3.4e-3.4h demonstrate the corresponding estimated spectra for η and NMO velocity from shifted hyperbola approximation (equations 3.8 and 3.9), rational approximation (equations 3.11 and 3.12), three-parameter approximation (equations 3.16 and 3.19) and acceleration approximation (equations 3.21 and 3.22), respectively. Due to the numerical artefacts resulting from small local slopes at small offsets, I filtered out the small-offset estimates. The yellow and red dots indicate the exact effective ηs and the exact effective NMO velocities used for forward modelling, respectively.

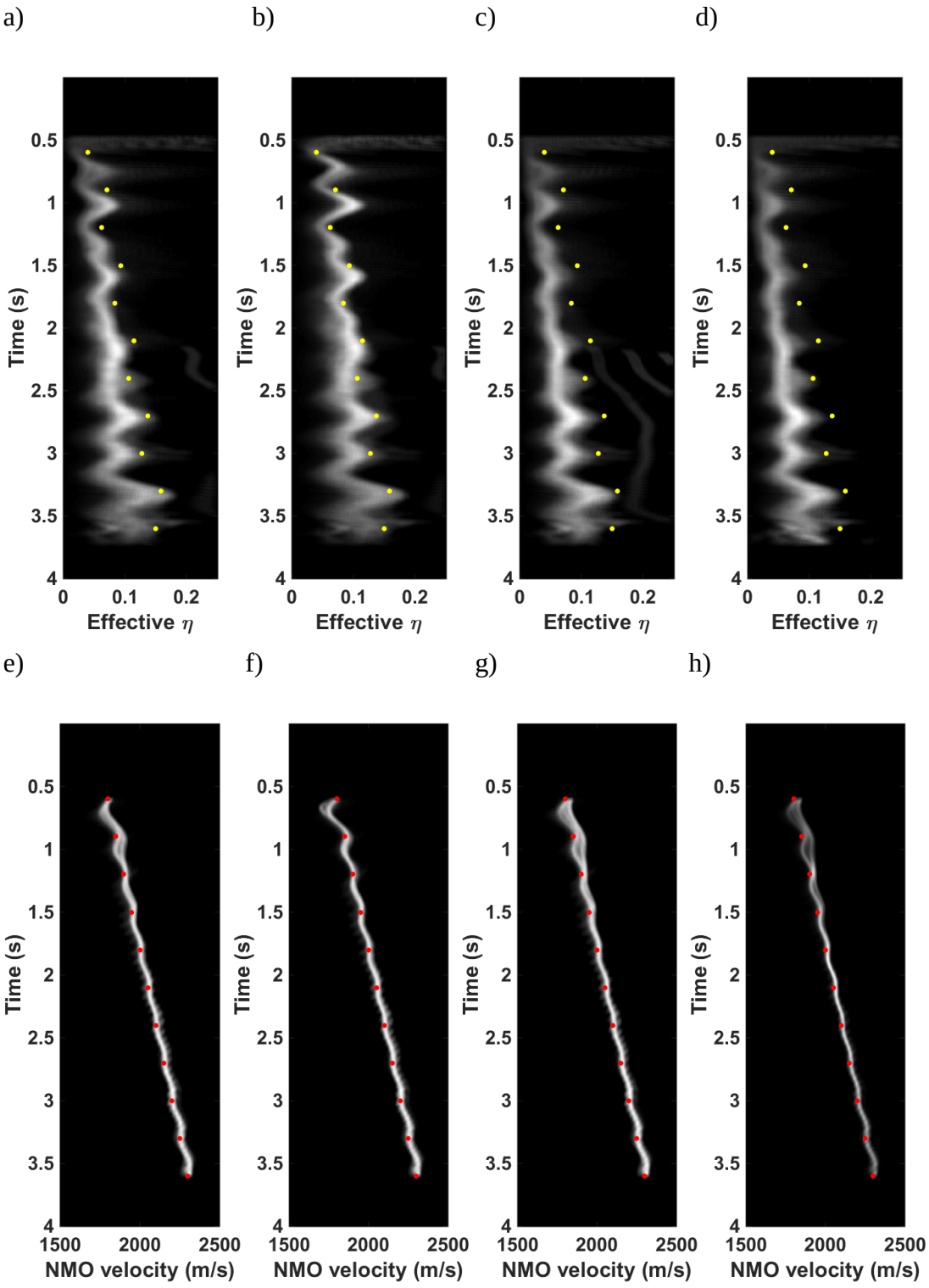

Figure 3.4: Estimated η from a) shifted hyperbola, b) rational, c) three-parameter and d) acceleration approximations, and estimated NMO velocity from e) shifted hyperbola, f) rational, g) three-parameter and h) acceleration approximations, by the application of the proposed technique for the anisotropic CMP gather shown in Figure 3.2b. Yellow and red dots indicate the exact effective ηs and NMO velocities used for forward modelling, respectively.

To have a better accuracy comparison between the estimated kinematic attributes from different approximations, I picked the maximum estimated attributes for the main time horizons in each spectrum and compared them with the exact values used in forward modelling. Figures 3.5a and 3.5b show the comparison of effective ηs and the effective NMO velocities obtained by the application of different approximations.

a)

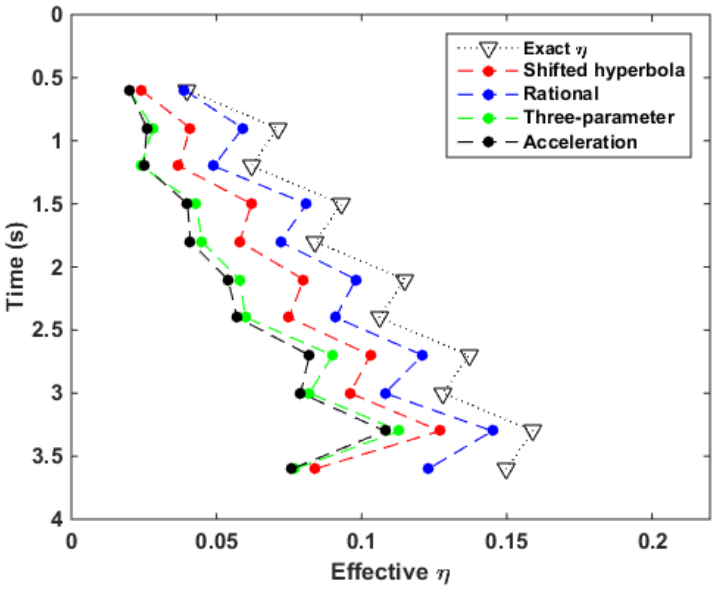

b)

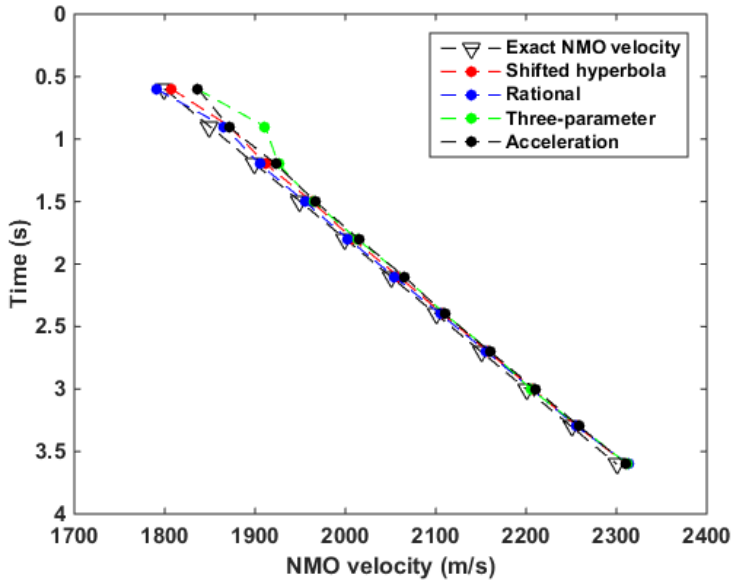

Figure 3.5: Comparison of a) η and b) NMO velocities estimated from different approximations by the implementation of the proposed technique to the anisotropic CMP gather shown in Figure 3.2b.

It is observed that the application of all approximations result in underestimated ηs and overestimated NMO velocities. Rational approximation has the highest accuracy while the acceleration approximation has the lowest accuracy. The error in effective η estimates increases with time/depth, whereas the error in NMO velocity estimates decreases with time/depth for all the approximations presented in this chapter. It is different from the observations of Stovas and Fomel (2016) stating that "the error in normal moveout velocity increases with depth for all approximations". The obtained results confirm the comparable accuracy of acceleration approximation with three-parameter approximation, as pointed out by Golikov and Stovas (2012).

3.6. Comparison with multi-parameter semblance

In the previous section, the proposed approach was evaluated on a synthetic data example. The accuracy of different approximations was also compared using the proposed approach. In this section, the computational time and the accuracy of the results obtained by multi-parameter semblance inversion technique and the results from the proposed approach are compared.

For simultaneous search/inversion of the kinematic attributes using multi-parameter semblance inversion, I defined 50 values for NMO velocity in the range of 1000-2500 m/s and 50 values for η in the range of 0.01-0.25. Figure 3.6 shows four NMO velocity-η spectra, indicating the inversion results for four different times using rational approximation. It is difficult to recognise the maximum semblance values by the visual observation within the spectra. The maximum values are chosen by automatic picking and are indicated by the red dots in the spectra. It is observed that the width of NMO velocities in each spectrum is noticeably narrower than the width of η. It confirms that the uncertainty in the inversion of NMO velocity is less than the uncertainty in the inversion of η.

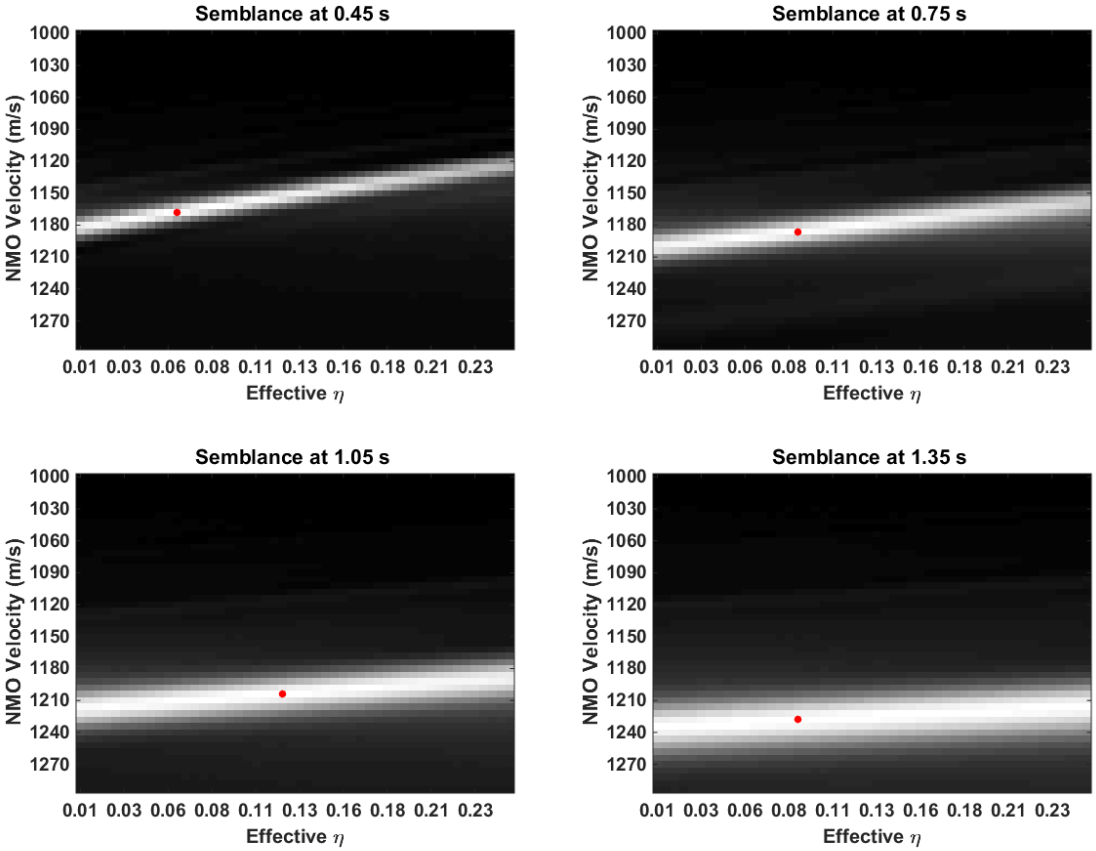

Figure 3.6: Inversion results of NMO velocity and effective η for four different times by the application of multi-parameter semblance inversion to the anisotropic CMP gather shown in Figure 3.2b using rational approximation. Red dots denote maximum semblance value picked in each spectrum.

Similar to the previous section, to quantify the accuracy of the estimated kinematic attributes from different approximations using multi-parameter semblance inversion, automatically picked values corresponding to the main time horizons in each spectrum are used to compare with the exact values used in forward modelling. Figures 3.7a and 3.7b show the comparison of the effective η estimates and the NMO velocity estimates obtained by the application multi-parameter semblance inversion for shifted hyperbola approximation (equations 3.5 and 3.9), rational approximation (equations 3.10), three-parameter approximation (equations 3.14 and 3.19) and acceleration approximation (equations 3.20).

a)

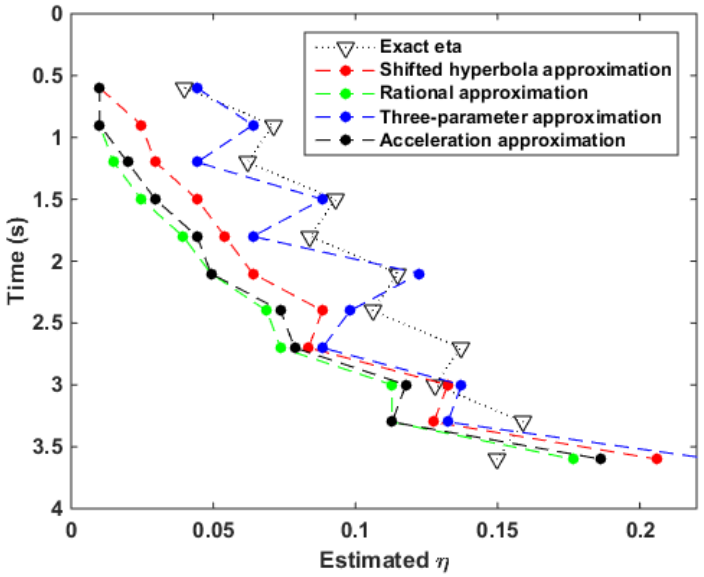

b)

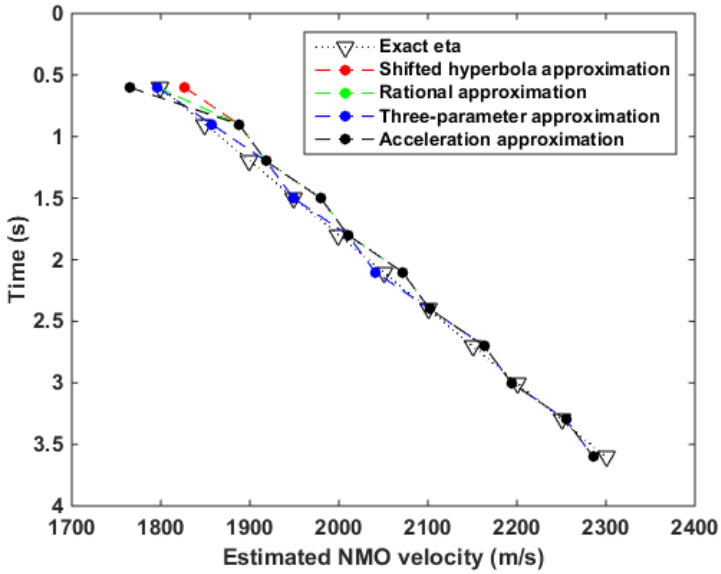

Figure 3.7: Comparison of a) η and b) NMO velocities estimated from different approximations, by the application of multi-parameter semblance to the anisotropic CMP gather shown in Figure 3.2b.

Based on the obtained results shown in Figure 3.7, rational approximation has the highest accuracy while the acceleration approximation has the lowest. The errors in the estimated effective ηs are not stable with time/depth (there is no a specific trend), whereas the error in NMO velocity decreases with time/depth for all approximations. The estimations from multi-parameter semblance inversion confirm the estimations from the proposed approach.

Recognition of the accuracy and/or error of the results from the both proposed and multi-parameter semblance inversion techniques (Figures 5 and 7) is difficult by visual observation. Therefore, I computed the relative errors in the estimation of kinematic attributes using both techniques for different approximations. Tables 3.2 and 3.3 show the computed errors in the estimation of η and NMO velocity, respectively. It is shown that the overall relative error using the proposed inversion technique is less than the multi-parameter semblance inversion technique.

	Shifted hyperbola	Rational	Acceleration	Three-parameter
Semblance inversion	40	18	49	51
Proposed inversion	32	13	49	46

Table 3.2: Relative error (%) in the estimation of η for the CMP gather shown in Figure 3.2b using the proposed and multi-parameter semblance inversion techniques.

	Shifted hyperbola	Rational	Acceleration	Three-parameter
Semblance inversion	0.85	0.4	0.9	0.75
Proposed inversion	0.51	0.35	1	0.82

Table 3.3: Relative error (%) in the estimation of NMO velocity for the CMP gather shown in Figure 3.2b using the proposed and multi-parameter semblance inversion techniques.

The most important advantage of oriented imaging/inversion techniques over the traditional techniques is related to their time-efficiency. Oriented techniques can be orders of magnitudes faster than the traditional techniques. Table 3.4, which shows the comparison of the computational times by the application of the proposed technique and semblance inversion using the same desktop computer, confirms it.

	The proposed oriented technique	Semblance technique
Computational time	*15 seconds* (including slope estimation and zero-offset estimation using predictive painting)	*Two hours*

Table 3.4: Comparison of computational time between the proposed and multi-parameter semblance inversion techniques, for the whole CMP gather (Figure 3.2b).

3.7. Comparison with the previous oriented techniques

In the previous sections, it was claimed that the proposed technique is the further improved and simplified version of the previous oriented/velocity-independent inversion techniques for the estimation of kinematic attributes in VTI media. In this section, I used the same synthetic anisotropic CMP gather (Figure 3.2b) and quantified the accuracy in the inversion of the attributes using the proposed and previous techniques. Shifted hyperbola and rational approximations, which are considered in both presented and previous approaches (Fomel, 2007a; Stovas and Fomel, 2016), are used for the demonstration.

3.7.1. Shifted hyperbola approximation

The second derivative of TWTT with respect to offset (curvature), which is the derivative of local sloes with respect to offset, is one of the inputs for the estimation of kinematic attributes using shifted hyperbola approximation in the previous velocity-independent inversion techniques (Fomel, 2007; Stovas and Fomel, 2016). The curvature is estimated by the application of chain rules (Bóna, 2011; Casasanta and Fomel, 2011):

$$q = \frac{\partial p}{\partial x} + p\frac{\partial p}{\partial t}, \tag{3.23}$$

where q denotes the second derivative of TWTT with respect to offset. The gradient components of local slopes in both offset and time directions $(\frac{\partial p}{\partial x}, \frac{\partial p}{\partial t})$ are estimated using numerical differentiation. The curvatures estimated from equation 3.23 are shown in Figure 3.8a. Another way to estimate the curvature is to use semblance analysis (see Discussion). The kinematic attributes, including zero-offset TWTT, derived by Fomel (2007), and Stovas and Fomel (2016) for shifted hyperbola approximation are expressed by

$$t_0 = t - \frac{px}{1+\sqrt{\frac{qx}{p}}}, \tag{3.24}$$

$$s = 1 + \frac{p(t-px)-qxt}{\sqrt{qp^3x^3}}\,, \tag{3.25}$$

$$v^2 = \frac{1}{t_0}\sqrt{\frac{qx^3}{p^3}}. \tag{3.26}$$

In the above equations, p, q, x, t, t_0, v and s denote local slope, curvature, offset, TWTT, zero-offset TWTT, NMO velocity and anisotropic parameter, respectively. The relation between s and anisotropy anellipticity coefficient (η) is given by equation 3.9 (Golikov and Stovas, 2012). Figure 3.8b shows the estimated zero-offset TWTT using equation 3.24. Figure 3.8c shows the result of flattening of the anisotropic gather shown in Figure 3.2b, using the estimated zero-offset TWTTs. It is observed that the data is not properly flatted in far-offsets, where is the area of interest for the study of anisotropy.

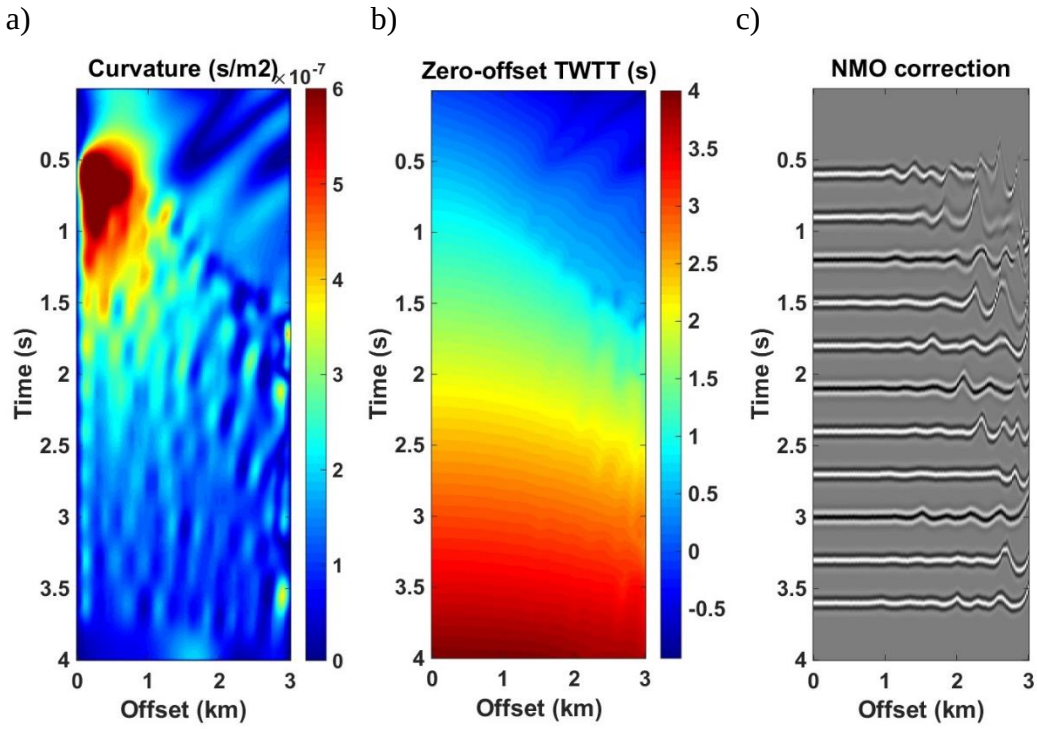

Figure 3.8: a) Curvatures estimated form equation 3.23, b) zero-offset TWTTs estimated from equation 3.24 (Fomel, 2007; Stovas and Fomel, 2015), and c) the NMO corrected CMP gather using the estimated zero-offset TWTTs.

Figures 3.9a and 3.9b show the estimated effective η and the estimated NMO velocity for shifted hyperbola approximation from equations 3.25 and 3.26 (Fomel, 2007; Stovas and Fomel, 2016), respectively.

a) b)

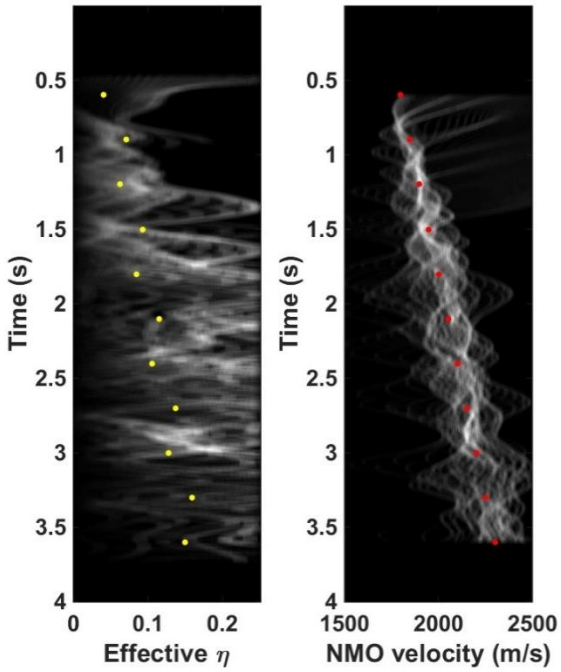

Figure 3.9: Estimated a) effective η and b) NMO velocity for shifted hyperbola approximation by the application of equations 3.25 and 3.26, respectively. The indicated dots show the exact values of the kinematic attributes used for forward modelling to generate the anisotropic CMP gather shown in Figure 3.2b.

Comparison between the estimated attributes by the proposed technique (Figures 3.2a and 3.2e) and by the previous techniques (Figures 3.9a and 3.9b) shows that the accuracy of the proposed technique is noticeably higher than the accuracy of the previous techniques for shifted hyperbola approximation. This is due to the curvature independence of the proposed technique.

3.7.2. Rational approximation

The kinematic attributes (η and NMO velocity), derived by Stovas and Fomel (2016) for rational approximation are given by equations 3.10-3.13. In their approach, zero-offset TWTT (t_0) is estimated by solving the following equation:

$$t_0{}^2 = \tau_0{}^2 + t^2 - ptx. \tag{3.27}$$

${\tau_0}^2$ must be estimated by solving the following equation:

$$a{\tau_0}^8 + b{\tau_0}^6 + c{\tau_0}^4 + d{\tau_0}^2 + e = 0, \tag{3.28}$$

where

$$a = 16, \tag{3.29}$$

$$b = -8Dx, \tag{3.30}$$

$$c = 12Dptx^2, \tag{3.31}$$

$$d = Dt^2x^2[-D + 4p(t - px)], \tag{3.32}$$

$$D = pt - p^2x - qtx. \tag{3.33}$$

Two possible solutions for ${\tau_0}^2$ are given by

$${\tau_0}^2{}_{1,2} = \frac{b}{4a} - z \pm \frac{1}{2}\sqrt{-4z^2 - 2m - \frac{n}{z}}, \tag{3.34}$$

$${\tau_0}^2{}_{3,4} = \frac{b}{4a} - z \pm \frac{1}{2}\sqrt{-4z^2 - 2m + \frac{n}{z}}. \tag{3.35}$$

z is derived by he solving the following equation

$$z = \frac{1}{2}\sqrt{-\frac{2}{3}m + \frac{1}{3a}\left(l + \frac{w}{l}\right)}, \tag{3.36}$$

where

$$l = \sqrt[3]{\frac{y + \sqrt{y^2 - 4w^3}}{2}}. \tag{3.37}$$

w and *y* are given by

$$w = c^2 - 3bd + 12ae, \tag{3-38}$$

$$y = 2c^3 - 9bcd + 27b^2e + 27ad^2 - 72ace, \tag{3-39}$$

where

$$m = \frac{8ac - 3b^2}{8a^2}, \tag{3-40}$$

$$n = \frac{b^3 - 4abc + 8a^2d}{8a^3}, \tag{3-41}$$

Figure 3.10a shows the estimated zero-offset TWTT from equation 3.27. Figure 3.10b shows the result of flattening of the anisotropic CMP gather shown in Figure 3.2b, from the estimated zero-offset TWTTs. It is observed that the data is not properly flatted in both near and far-offsets.

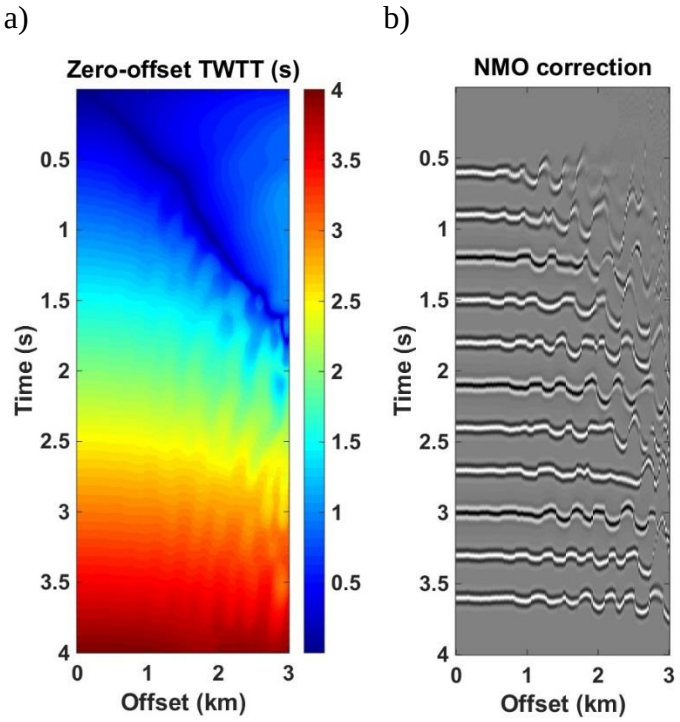

Figure 3.10: a) Zero-offset TWTTs estimated from equation 3.27 (Stovas and Fomel, 2015) and c) the corresponding NMO corrected CMP gather using the estimated zero-offset TWTTs.

Figures 3.11a and 3.11b show the estimated effective η and the estimated NMO velocity for rational approximation from equations 3.11 and 3.12 (Stovas and Fomel, 2016), respectively. Accuracy in the inversion of the kinematic attributes using the proposed technique is noticeably higher than the previous technique for rational approximation. This higher resolution is due to: a) the curvature dependence of the proposed approach, and b) unique estimated values for zero-offset TWTT (t_0), rather than non-unique answers obtained by the solution of a complicated equation for ${t_0}^2$ proposed in the previous technique.

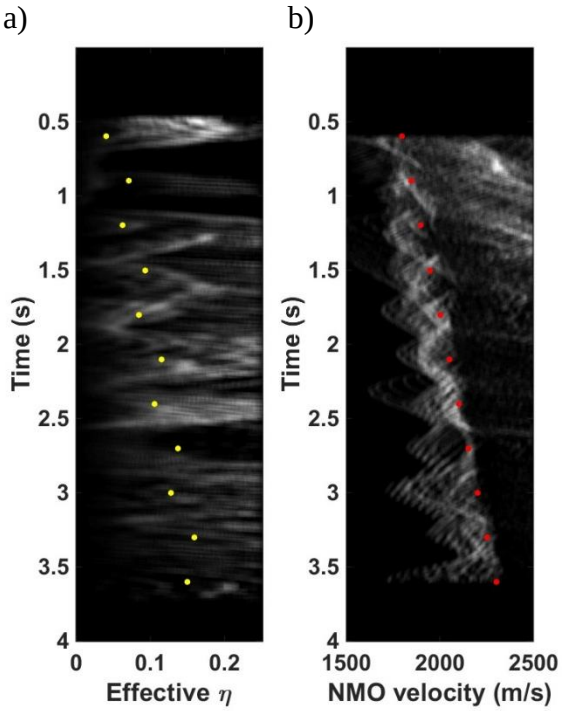

Figure 3.11: Estimated a) effective η and b) NMO velocity for rational approximation by the application of equations 3.10-3.13, respectively. The indicated dots show the exact values the kinematic attributes used for forward modelling.

3.8. Application to a real data example

Since I did not have access to a proper anisotropic CMP gather, I modified an isotropic CMP gather from a 2D marine data recorded by Geoscience Australia in 1996 over North West Shelf, Western Australia, shown in Figure 3.12a. The modified gather was used to examine the performance of the proposed algorithm in real data situation. The following steps are considered for the modification:

1- NMO velocities of the data (Figure 3.12a) were manually and precisely picked,
2- NMO correction was applied to the data by the application of predictive painting (Figure 3.12b).
3- A range of η between 0-0.2 was defined,
4- Given the NMO velocities and the defined values for η, I did anisotropic modelling (Bóna, 2008) to design an inverse NMO operator (Figure 3.12c).
5- The anisotropic data was made by the application of the inverse NMO operator shown in Figure 3.12d.

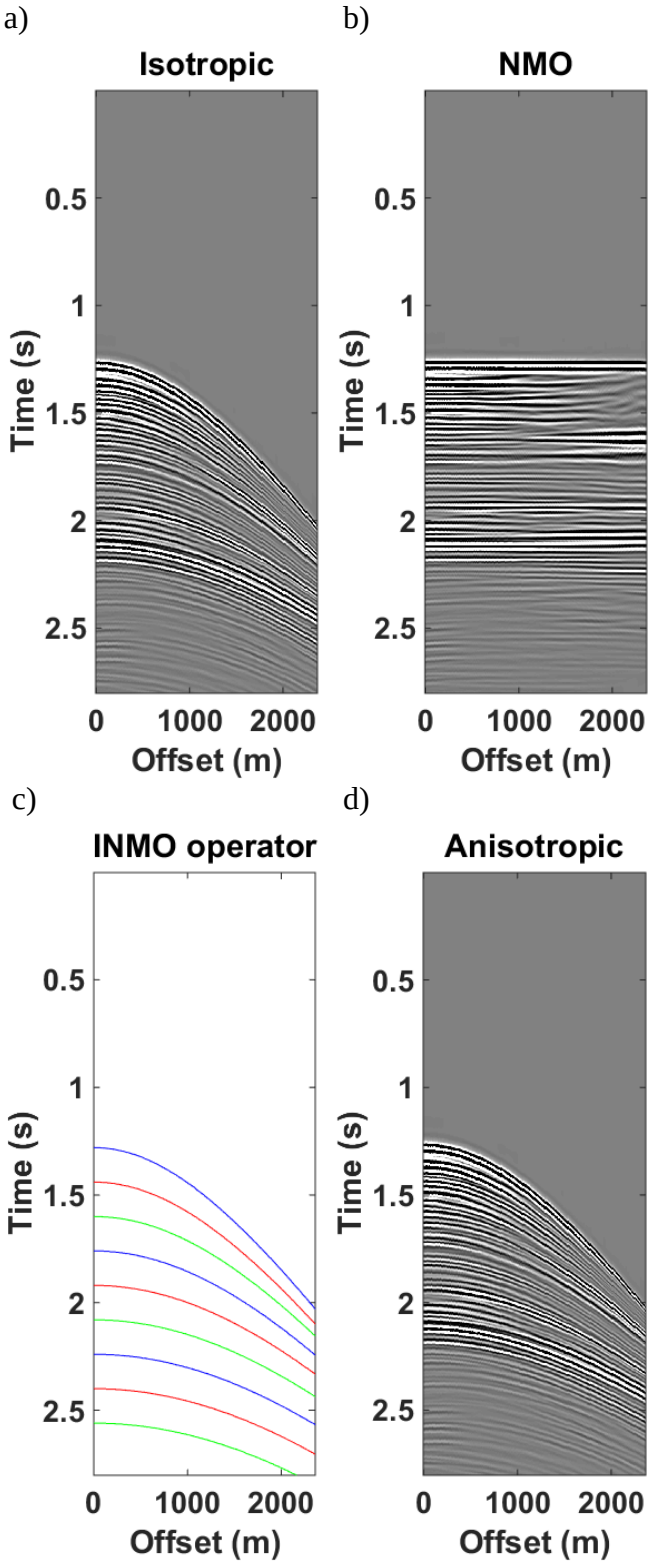

Figure 3.12: a) Original CMP gather from North West Shelf, Western Australia b) velocity-independent NMO corrected CMP gather by the application of predictive painting c) anisotropic inverse NMO operator and d) inverse NMO corrected (anisotropic) CMP gather by the application of the anisotropic operator.

The modified CMP gather is proper to examine the performance of the proposed inversion technique in real data situation. Another advantage in the use of the CMP gather regards to the primary knowledge of the NMO velocity and the effective η; it helps to judge and quantify the final results. Herein, I estimated the kinematic attributes by implementing the proposed technique and multi-parameter semblance inversion for rational approximation that had the highest accuracy among the other approximations presented in this chapter. Then, I compared the accuracy of the obtained results by the application of both techniques.

Figures 3.13a and 3.13b show the local slopes and the zero-offset TWTTs estimated using plane wave destructor and predictive painting, respectively.

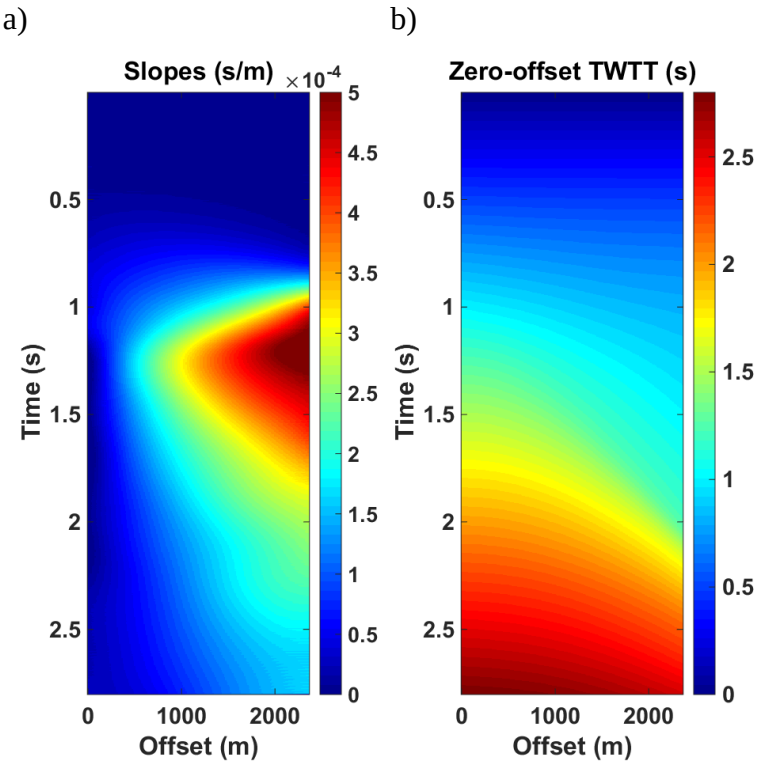

Figure 3.13: a) Local slopes estimated by plane wave destructor and e) zero-offset TWTTs estimated by predictive painting, for the marine CMP gather shown in Figure 3.12d.

Figures 3.14a and 3.14b show the corresponding spectra for the inversion of the effective/NMO velocity and the effective η, respectively. The green lines indicate the exact values of the attributes, the red lines indicate the highest probable values

estimated by the application of the proposed technique, and the yellow lines show the estimated values from multi-parameter semblance inversion.

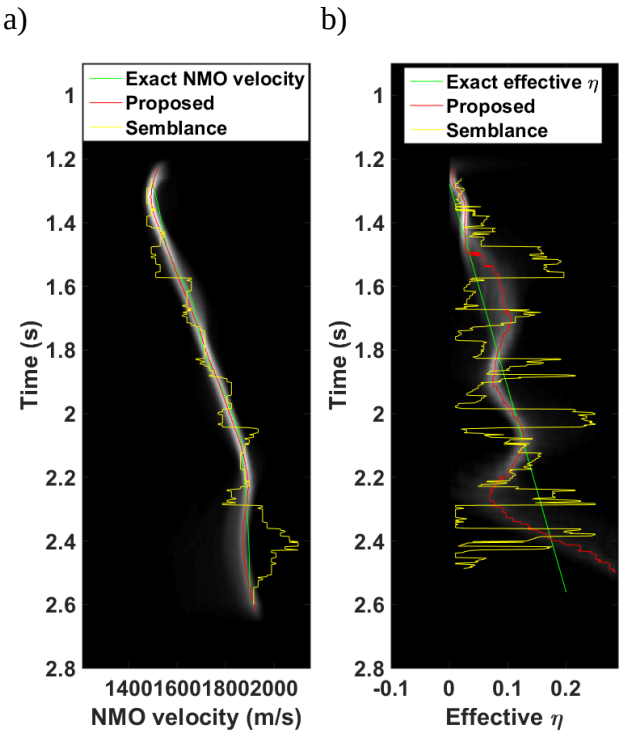

Figure 3.14: a) Effective η and b) NMO velocity estimated using rational approximation for the CMP gather shown in Figure 3.12d. Green lines indicate the exact values, red lines indicate the estimated values by the application of the proposed technique, and yellow lines indicate the values estimated by the application of routine multi-parameter semblance analysis.

Tables 3.5 shows the computed relative errors in the estimation of NMO velocity and effective η, respectively. Based on the achieved results, the overall relative error using the proposed inversion technique is less than the multi-parameter semblance inversion technique. Computational time by the use of the proposed technique was around 10 s, whereas it was approximately two hours for the semblance inversion technique.

	NMO velocity	Effective η
Semblance inversion	4.5	111
Proposed inversion	0.006	57

Table 3.5: Relative error (%) in the estimation of NMO velocity and effective η for the field CMP gather (Figure 3.12d) by the proposed and conventional techniques.

3.9. Sensitivity to noise

Accuracy of any local slope based velocity-independent imaging technique, depends on the precision of the estimated local slopes. I used plane wave destructor to estimate the local slopes. Plane wave destructor is not as sensitive as other local slope estimation techniques (e.g., Schleicher et al., 2009) that use numerical differentiation. It is because plane wave destructor relies on: a) smoothing the seismic data, and b) the use of regularisation (Fomel, 2002); however, if the level of noise is high, the accuracy of the local slopes estimated by plane wave destructor would be affected.

To examine the performance of the technique in the presence of noise, I contaminated the synthetic CMP gather used in the first example (Figure 3.2b) with band limited white noise with the frequency range of 5-150 Hz so that the signal-to-noise ratio (S/N) is 10. This level of S/N is fairly acceptable for the residual noise left in a gather/section after pre-processing and denoising. I used the following equation to scale the S/N

$$\frac{S}{N} = \frac{E_S}{E_N} = \frac{\sum_{-m}^{m}\sum_{-n}^{n} {A_S}_{i,j}{}^2}{\sum_{-m}^{m}\sum_{-n}^{n} {A_N}_{i,j}{}^2}, \tag{3.42}$$

where A_S and A_N denote the amplitude of signal and noise in each sample, respectively. i and j are counters for trace and sample number in each trace within the window of each seismic event ($2m$). As the purpose of this example is to study the sensitivity of the proposed technique to noise, I only used the rational approximation that had the highest accuracy within the other presented approximations in this work. Figures 3.15a-3.15c show the noisy synthetic data, the corresponding estimated local slopes and zero-offset TWTTs using plane wave destructor and predictive painting, respectively. To have higher accuracy in the estimation of local slopes, the differentiation order was raised from 6 to 14.

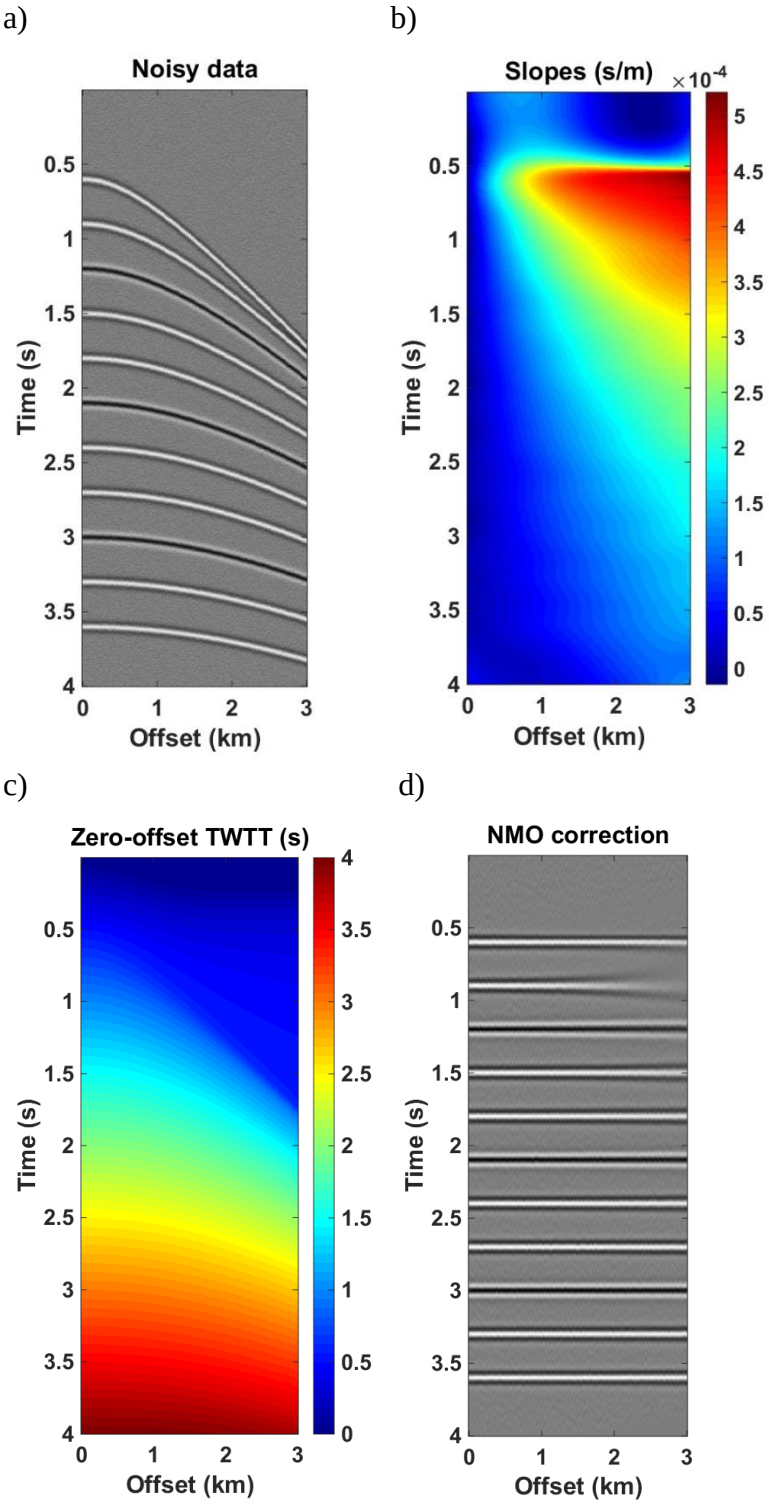

Figure 3.15: a) Noisy CMP gather generated based on the kinematic attributes in Table 3.1 and contaminated with band limited white noise (S/N=10), b) local slopes estimated by plane wave destructor, c) zero-offset TWTTs by predictive painting, and d) the corresponding NMO corrected CMP gather.

Figure 3.16a and 3.16b show the estimated NMO velocity and effective η for the noisy CMP gather shown in Figure 3.15a from the proposed technique, respectively.

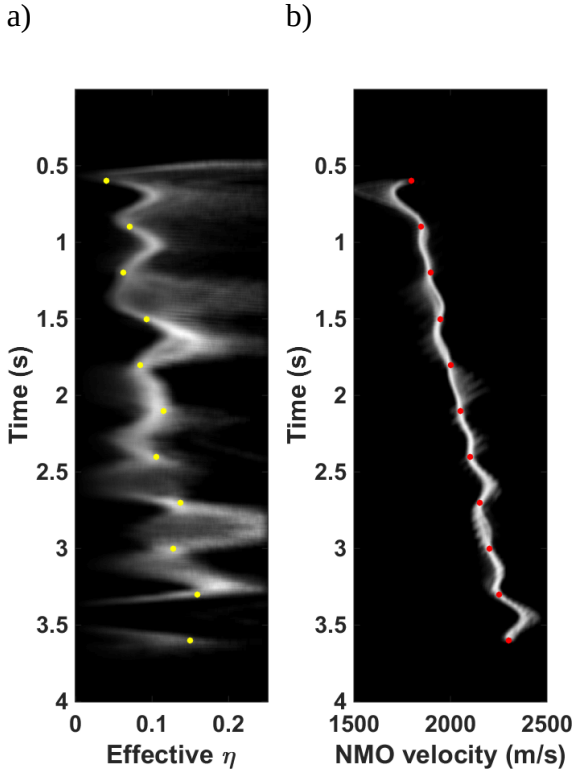

Figure 3.16: Estimated a) effective η and b) NMO velocity for rational approximation by the application of equations by the application of the proposed technique to the noisy CMP gather shown in Figure 3.15a. The indicated dots show the exact values the kinematic attributes used for forward modelling.

Comparison of the results from the noise-free and the noisy CMP gathers show that the proposed technique is not noticeably affected by the use of local slopes estimated with higher order differentiation (14). To quantify this difference, the relative error in the estimation of kinematic attributes using the presented technique for both noise-free and the noisy data is compared and shown in Table 3.6.

	NMO velocity	Effective η
Noise-free data	0.35	13
Noisy data	0.44	12.08

Table 3.6: Relative error in the estimation of NMO velocity and effective η (%) for noise-free and noisy synthetic data shown in Figures 3.2b and 3.15a.

3.10. Discussion

In the presented research, it was shown that removing the second derivative of TWTT with respect to offset (curvature) leads to more accurate estimations of kinematic attributes in VTI media. The reason for the higher accuracy in the estimation of the attributes is the reduction of numerical errors caused by the calculation of curvatures.

Estimation of curvature using numerical differentiation (equation 3.23) is unstable because finite differences made by the implementation of numerical differentiation act as high-pass filters, which create the high-frequency artefacts, especially in the presence of noise (Casasanta and Fomel, 2011). In other words, there are enough samples in time direction and differentiability condition is satisfied; however, in offset direction, it is not the case, specifically in far-offsets that are more important for the study of seismic anisotropy. In the presence of spatial aliasing, curvature estimation will be even a more challenging task. To overcome the effect of spatial aliasing, seismic interpolation must be applied to the data prior to curvature estimation.

The study of different techniques for curvature estimation, specifically in the presence of noise, is still an open task (Bóna, 2011). Semblance analysis using the Taylor Expansion is another possibility for the curvature estimation. To do so, TWTT must be expanded around the each point of a gather. A scanning window with a defined number of traces should be defined and used. The expansion is given by

$$t(h \pm \Delta x) = t(h) + p\Delta x + \frac{1}{2} q\Delta x^2 + \cdots \tag{3.25}$$

herein, $t(h)$ is the TWTT in a given offset (h) in a seismic gather/record that is located at the centre of the scanning window, $t(h \pm \Delta x)$ is the expanded TWTT with a certain distance (Δx) from the central trace in the scanning window, p is the estimated slopes by plane wave destructor or by other slope estimation techniques, and q denotes the desired curvature. Analogous to the procedure previously explained for multi-parameter semblance analysis, a range of possible curvatures should be defined for

scanning. There are the following limitations in curvature estimation using semblance analysis and Taylor Expansion. They are due to

- Computational time that is very high,
- Sensitivity to the number of traces chosen in the scanning window,
- Instability in the estimation of curvature in far-offsets, where curvature almost disappears from the seismic events.

Considering the limitations and difficulties in the estimation of curvature with high accuracy, developing new curvature-independent imaging/inversion techniques that uses local slopes, which carry complete information of the subsurface structures (Fomel, 2007a), would be easier, time-efficient, more accurate and more applicable in comparison with curvature-dependent techniques. The presented research in this chapter tried to improve the resolution by removing the curvature from the previous researches.

The input of the algorithm must be pre-processed and denoised data; however, it is potentially still possible to perform the proposed algorithm to a data containing higher level of band-limited white noise. To do so, one can update the estimated slopes, by the use of predictive painting and estimation of traveltime curves using time-warping, explained in section 3.5. This process can be repeated, and in principle the higher the number of iterations, the higher the accuracy of the updated local slopes. Note that the higher accuracy in the estimation of traveltime curves belongs to the use of seismic regularization and coherency analysis of the regulated data in predictive painting (Fomel, 2007b; Fomel et al., 2013).

Zero-offset TWTT (t_0) is an input of the proposed approach that was computed by predictive painting in this chapter. One can use another horizon picking techniques (e.g., Lomask et al. 2006; Wu and Hale, 2014) that are equivalently capable of providing the zero-offset TWTT.

3.11. Conclusions

I proposed an oriented algorithm for the inversion of kinematic attributes in VTI media. The algorithm builds on the previous anisotropy algorithms. The algorithm does not require a prior knowledge of a velocity model. The main advantages of the algorithm are its time-efficiency and curvature independence. The presented method can be orders of magnitudes faster than the routine multi-parameter semblance inversion for the estimation of kinematic attributes in VTI media. The only initial requirements of the technique are the local slopes in each point and the corresponding zero-offset TWTTs. Curvature dependence of the previous techniques was replaced by the use of predictive painting technique to estimate the zero-offset TWTTs.

Comparison of the inverted kinematic attributes obtained by the application of the proposed technique to a numerical transversely isotropic model from shifted-hyperbola approximation, rational approximation, three-parameter approximation, and acceleration approximation shows that the rational approximation has the highest accuracy while the acceleration approximation has the lowest accuracy for both η and NMO velocity. Regardless of approximation type, it is demonstrated that the accuracy in the inversion of NMO velocity is higher than the accuracy in the inversion of η. As opposed to some previous observations, the results show that error in NMO velocity inversion does not necessarily increase with depth.

Based on the promising results obtained by the application of the proposed technique to different scenarios, including synthetic, noisy and real data examples, the proposed technique can be used as an alternative for the inversion of the kinematic attributes in VTI media, specifically for offshore data that does not contain considerable level of noise. Further development of the technique involves extension of the approach to generalized moveout approximation and estimate of the interval parameters (in both time and depth) from the effective estimated parameters.

3.12. References

Alkhalifah, T., and I. Tsvankin, 1995, Velocity analysis for transversely isotropic media: Geophysics, **60**, 1550–1566, doi:10.1190/1.1443888.

Asgharzadeh, M., D. Nadri, and A. Bóna, 2014, Inversion Based Accuracy Comparison of Nonhyperbolic Moveout Approximations for P-waves in VTI Media, 76th Conference and Exhibition, EAGE, Extended Abstracts, doi: 10.3997/2214-4609.20140989.

Blias, E., 2007, Long-spread length approximations to NMO function for a multi-layered subsurface: Recorder, **3**, 36–42.

Blias, E., 2009, Long-offset NMO approximations for a layered VTI model. Model study: 79th Annual International Meeting, SEG, Expanded Abstracts, 3475–3479.

Bóna, A., I. Bucataru, and A. Slawinski, 2008, Inversion of ray velocity and polarization for elasticity tensor; Journal of applied Geophysics, **65**, 1-5.

Bóna, A., 2011. Shot-gather time migration of planar reflectors without velocity model: Geophysics, **76**, no. 2, S93–S101.

Burnett, W., and S. Fomel, 2009a, 3D velocity-independent elliptically anisotropic moveout correction: Geophysics, **74**, no. 5, WB129–WB136, doi: 10.1190/1.3184804.

Burnett, W., and S. Fomel, 2009b, Moveout analysis by time-warping: 79th Annual International Meeting, SEG, Expanded Abstracts, **28**, 3710–3714.

Casasanta, L., and S. Fomel, 2011, Velocity-independent τ-p moveout in a horizontally layered VTI medium: Geophysics, **76**, no. 4, U45-U47.

Castle, R. J., 1994, Theory of normal moveout: Geophysics, **59**, 983–999.

Cooke, D., A. Bóna, and B. Hansen, 2009, Simultaneous time imaging, velocity estimation and multiple suppression using local event slopes: Geophysics, **74**, no. 6, WCA65–WCA73.

De Bazelaire, E., 1988, Normal moveout revisited: Inhomogeneous media and curved interfaces: Geophysics, **53**, 143–157.

Fomel, S., 2002, Applications of plane-wave destruction filters: Geophysics, **67**, 1946–1960, doi:10.1190/1.1527095.

----------, 2007a, Velocity-independent time-domain seismic imaging using local event slopes: Geophysics, **72**, no. 3, S139–S147, doi:10.1190/1.2714047.

----------, 2007b, Shaping regularization in geophysical-estimation problems, Geophysics, **72**, no. 2, R29–R36, doi:10.1190/1.2433716.

----------, 2010, Predictive painting of 3D seismic volumes: Geophysics, **75**, no. 4, A25–A30, doi: 10.1190/1.3453847.

Fomel, S., and A. Stovas, 2010, Generalized nonhyperbolic moveout approximation: Geophysics, **75**, no. 2, U9–U18, doi:10.1190/1.3334323.

Fomel, S., P. Sava, I. Vlad, Y. Liu, and V. Bashkardin, 2013, Madagascar: open-source software project for multidimensional data analysis and reproducible computational experiments. Journal of Open Research Software 1 (1): e8, doi: http://dx.doi.org/10.5334/jors.ag.

Fowler, P. J., A. Jackson, J. Gaffney and D. Boreham, 2008, Direct nonlinear traveltime inversion in layered VTI media. 78th annual international meeting, SEG, Expanded Abstracts, 3028–3032.

Golikov, P., and A. Stovas, 2012, Accuracy comparison of nonhyperbolic moveout approximations for qP-waves in VTI media: Journal of Geophysics and Engineering, **9**, 428-432.

Lomask, J., A. Guitton, S. Fomel, J. Claerbout, and A. A. Valenciano, 2006, Flattening without picking: Geophysics, 71, no. 4, P13–P20, doi: 10.1190/1.2210848.

Malovichko, A. A., 1978, A new representation of the traveltime curve of reflected waves in horizontally layered media: Applied Geophysics (in Russian), **91**, 47–53. English translation in C. H. Sword, 1987, A Soviet look at datum shift, SEP-51: Stanford Exploration Project, 313–316, accessed 26 January 2010; http://sepwww.stanford.edu/data/media/public/oldreports/sep51/51_22.pdf.

Ottolini, R., 1983, Velocity independent seismic imaging: Technical report, Stanford Exploration Project, SEP-37: Stanford University.

Riabinkin, L. A., 1957, Fundamentals of resolving power of controlled directional reception (CDR) of seismic waves, in L. Lu, ed., Slant-stack processing, 1991, SEG, 36–60. (Translated and paraphrased from Prikladnaya Geofiizika, 16, 3–36).

Rieber, F., 1936, A new reflection system with controlled directional sensitivity: Geophysics, **1**, 97–106, doi: 10.1190/1.1437082.

Schleicher, J., J. C. Costa, L. T. Santos, A. Novais, and M. Tygel, 2009, On the estimation of local slopes: Geophysics,

Stovas, A., and S. Fomel, 2016, Mapping of moveout attributes using local slopes: Geophysical prospecting, **64**, no. 1, 31-37, doi: 10.1111/1365-2478.12284.

Taner, M. T., S. Treitel, and M. Al-Chalabi, 2005, A new travel time estimation method for horizontal strata: 75th Annual International Meeting, SEG, Expanded Abstracts, 2273–2276.

Taner, M. T., S. Treitel, M. Al-Chalabi, and S. Fomel, 2007, An offset dependent NMO velocity model: 69th Conference and Exhibition, EAGE, P036.

Wu, X., and D. Hale, 2014, Horizon volumes with interpreted constraints: Center for Wave Phenomena, Report CWP-812.

Yilmaz, O., 2001, Seismic data analysis, processing, inversion, and interpretation of seismic data: Investigations in Geophysics Series no. 10, SEG.

4. Oriented prestack time migration using local slopes and predictive painting in common-source domain for planar reflectors

4.1. Overview

Velocity analysis is one of the most critical stages in seismic data processing. Standard ways to find the velocity model are constant velocity stack and semblance velocity analysis, which can be time-consuming and labour-intensive. Oriented/velocity-less imaging using local event slopes is an alternative to conventional imaging techniques. In some previous oriented techniques, seismic data must be sorted in two different domains while seismic data is not always available in both domains and the use of interpolation in inevitable in such case. Other methods are developed in terms of higher order derivatives of traveltime with respect to offset while estimation of the higher order derivatives is difficult to achieve with the required accuracy. In this work, improvements are achieved by proposing a local slope based prestack time migration technique in only one domain: common source domain. The migration technique is developed for planar reflectors. In the proposed approach, the need for estimation of higher order derivatives is replaced by a point-to-point mapping of seismic data using predictive painting technique. The theoretical possibility of the proposed technique is first demonstrated on a simple synthetic data example and then applied to a field data set.

4.2. Introduction

In many routine seismic data processing and imaging techniques, a seismic velocity model must be provided prior to imaging. The velocity model can be built through seismic velocity analysis; however, seismic velocity analysis is still one of the most critical stages in seismic data processing (Yilmaz, 2001). The conventional seismic velocity analysis workflows, are generally labour-intensive and time-consuming (Yilmaz, 2001, Fomel, 2007). Such workflows are often designed for only layered models and an experienced processor is required to pick the velocities in the velocity spectrum. Taking anisotropy into account, where more than a single parameter is required for higher-order traveltime approximations (e.g. Alkhalifah and Tsvankin, 1995; Landa et al., 1999; Fomel and Stovas, 2010), velocity analysis is even more time-consuming.

An alternative to the conventional time-domain imaging techniques is to develop time-effective imaging techniques that do not require an input velocity model for image construction. These techniques are known as velocity-independent, velocity-less or oriented imaging techniques. They typically use local event slopes and the derivatives of traveltime with respect to the position of the receivers on the surface (Fomel, 2007, Cooke et al., 2009, Bóna, 2011, Khoshnavaz et al., 2015). Local slopes in seismic data carry complete information about the reflection geometry (Fomel, 2007b). The first idea of local slopes estimation and employing them to make seismic velocity models goes back to the researches done by Rieber (1936), Ottolini (1983b) and Riabinkin (1991). Ottolini (1983b) derived the migration velocity for each point in the registered seismic data using local slopes in order to apply it on his velocity-less migration algorithm for horizontal interfaces. Fomel (2007b) generalized this idea by developing analytical velocity-less techniques to transform seismic events from prestack domain to the image domain for different time-domain imaging operators. His work includes migration to zero offset (DMO) and prestack time migration. In his proposed techniques, recorded seismic data should be sorted in common midpoint and common offset domains and the corresponding local slopes must be measured in these domains. Cooke et al. (2009) designed an analogous oriented migration technique that

used local slopes estimated in common-source and common-receiver domains. They used this technique to migrate seismic data and remove multiples.

There are two limitations in the use of oriented imaging techniques presented by Fomel (2007a) and Cooke et al. (2009). First, interpolation of shots and/or receivers is likely required before calculation of local sloes (Cooke et al., 2009). For example, the spacing between sources can be too large while there can be only few sources available. Second, sorting the data in two domains and estimating the slopes can be time-consuming. To address these limitations, Bóna (2011) developed an oriented prestack time migration technique for planar continuous reflectors with small curvature. In his technique, seismic data needs only be sorted in one domain: common source domain. To estimate the migration attributes for each point in his technique, the first (local slopes) and the second (curvatures) derivatives of two-way-traveltime with respect to offset in common-source domain are required. The velocity estimation and migration is done simultaneously. The main limitation of his technique is the estimation of the second derivatives of two-way-travel-time with respect to offset is difficult to achieve with the required accuracy.

In this chapter, the work by Bóna (2011) is further developed by removing one order of differentiation from his technique. Instead of using the second derivatives, the use of two separate points on the seismic wave-front is proposed. This point-to-point mapping is done by the application of predictive painting technique as discussed in Chapter 3, see also Fomel (2010). Similar to Bóna (2011), the proposed migration technique is developed for specular continuous reflectors. The theoretical contents of the proposed technique is first verified on a simple synthetic data example and then applied to a 2D marine seismic data set.

4.3. Predictive painting

The use of predictive painting technique to connect two points on a seismic wavefront was explained in detail in Chapter 3. The main objective of predictive painting is to predict each seismic event from that same event on adjacent traces, which are shifted along the local event slopes (Claerbout, 1992; Burnet and Fomel, 2009; Fomel, 2010).

Local slopes are often estimated by measuring the time difference or time shift between two points carrying by a seismic wavefront. Given the local slopes, one can implement an inverse process to find the time shift between two neighbouring traces. The following equation expresses the predictive operator I use to connect the two points (Figure 4.1)

$$t_{i-n} = t_i - \left(\sum_{k=0}^{n-1} p_{x\,i-k}\right)\Delta x. \tag{4.1}$$

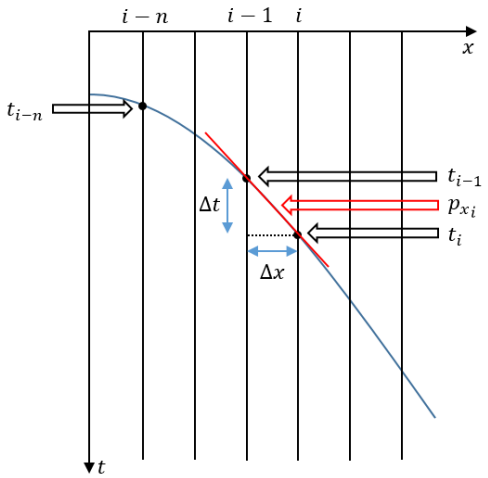

Figure 4.1: Predictive panting of a seismic event using local slopes.

4.4. Oriented velocity analysis

Consider the geometry of reflected wavefront from two separate points of the same wavefront coming from a planar reflector shown in Figure 4.2. Cosines of α_i and α_{i-n}, the angles between the observation line on the surface and the direction of the emergence rays of the two receivers, are given by

$$cos\ \alpha_i = \frac{p_{x_i}}{p} \tag{4.2}$$

$$cos\ \alpha_{i-n} = \frac{p_{x_{i-n}}}{p} \tag{4.3}$$

where n is the trace number difference between the two discrete receivers, and p_x is the horizontal component of the slowness vector p.

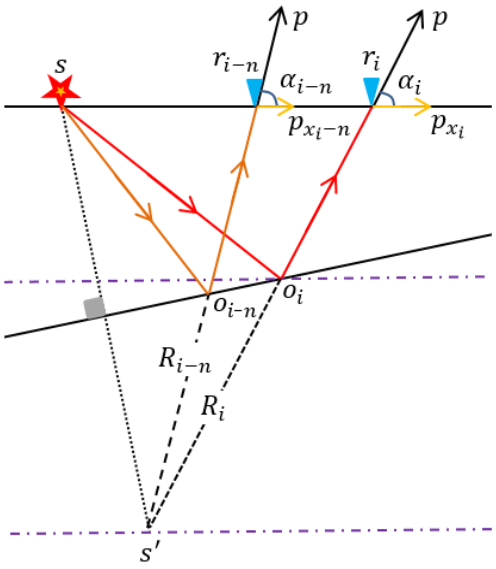

Figure 4.2: Geometry of reflected wavefront at two separate reflection points.

Writing the offsets between the seismic source and both receivers (x_{ri} and x_{ri-n}) in terms of the cosines, gives the horizontal coordinate of the image source ($x_{s'}$)

$$x_{s'} = x_{r_i} - \frac{t_i}{p} cos\, \alpha_i \tag{4.4}$$

$$x_{s'} = x_{r_{i-n}} - \frac{t_{i-n}}{p}\, cos\, \alpha_{i-n}. \tag{4.5}$$

t denotes the two-way-traveltime of the reflected wave in the above equations. Substituting equations 4.2 and 4.3 into equations 4.4 and 4.5, and equating the results gives the imaging slowness/velocity

$$p^2 = \frac{t_i p_{x_i} - t_{i-n} p_{x_{i-n}}}{x_{r_i} - x_{r_{i-n}}}. \tag{4.6}$$

An important aspect of this expression is that for a planar reflector we can compute the migration velocity (inverse of slowness) from data at many neighbouring points by varying their distance *n*. This extra "fold" can give us potentially more robust estimates of the velocity through the averaging process.

4.5. Oriented prestack time migration

In this section, I derived the oriented prestack time migration equations in order to migrate seismic data in common-source domain. As with the other time-domain migration methods, it is assumed that seismic wavefront propagates/emits through a constant velocity medium. This assumption is valid for many geological structures whose curvature of layering and sedimentations are small.

Consider the geometry of reflected wavefront through a constant velocity medium shown in Figure 4.2. Two-way-traveltime of seismic reflections and diffractions in a homogeneous medium is given by double square root equation (Claerbout, 1985)

$$\frac{t}{p} = \sqrt{(x_o - x_s)^2 + (z_o - z_s)^2} + \sqrt{(x_r - x_o)^2 + (z_r - z_o)^2}. \quad (4.7)$$

(x_s, z_s), (x_r, z_r) and (x_o, z_o) denote the spatial coordinates of the seismic source, receiver and the reflection point, respectively. Source gathers are treated independently in here. Hence, it is possible to zero out the *x* coordinate of the seismic source (x_s). Similarly, it is possible to assume that the z coordinates of the source and receivers are zero ($z_s = z_r = 0$). Then, the simplified double square root equation is given by

$$\frac{t}{p} = \sqrt{{x_o}^2 + {z_o}^2} + \sqrt{(x_r - x_o)^2 + {z_o}^2}. \quad (4.8)$$

The trigonometric functions of α, the angle between the observation line on the surface and the direction of the emergence ray at the receiver, are given by

$$cos\,\alpha = \frac{p_x}{p}, \quad (4.9)$$

$$sin\,\alpha = \left[1 - \left(\frac{p_x}{p}\right)^2\right]^{\frac{1}{2}}, \quad (4.10)$$

$$tan\,\alpha = \frac{z_o}{x_r - x_o} = \frac{\sin\alpha}{\cos\alpha} = \left[\left(\frac{p}{p_x}\right)^2 - 1\right]^{\frac{1}{2}}. \quad (4.11)$$

From equation 4-11, the vertical coordinate of the reflection point (z_o) is expressed by

$$z_o = (x_r - x_o)\,tan\,\alpha. \quad (4.12)$$

Substitution of equation 4-12 in 4-8 gives the following equations

$$\frac{t}{p} = \sqrt{{x_o}^2 + (x_r - x_o)^2 tan^2(\alpha)} + \sqrt{(x_r - x_o)^2 + (x_r - x_o)^2 tan^2(\alpha)} \tag{4.13}$$

$$\frac{t}{p} = \sqrt{{x_o}^2 + (x_r - x_o)^2 tan^2(\alpha)} + (x_r - x_o)\sqrt{1 + tan^2(\alpha)} \tag{4.14}$$

$$\frac{t}{p} = \sqrt{{x_o}^2 + (x_r - x_o)^2 tan^2(\alpha)} + \frac{x_r - x_o}{cos(\alpha)}. \tag{4.15}$$

Substitution of trigonometric ratios from equations 4-9 and 4-12 in 4-15, applying some algebra and simplifications lead to the horizontal coordinate of the reflection point in terms of two-way-traveltime, effective slowness, local slopes and offset

$$x_o = \frac{-t^2 p_x + p^2(2t x_r - {x_r}^2 p_x)}{2p^2(t - x_r p_x)}. \tag{4.16}$$

Substitution of equations 4-11 and 4-16 in 4-12 gives the vertical coordinate of the reflection point

$$z_o = \left[x_r - \frac{-t^2 p_x + p^2(2t x_r - {x_r}^2 p_x)}{2p^2(t - x_r p_x)}\right]\left[1 - \left(\frac{p}{p_x}\right)^2\right]^{\frac{1}{2}} \tag{4.17}$$

$$z_o = \frac{(t^2 - p^2 {x_r}^2)({p_x}^2 - p^2)^{\frac{1}{2}}}{2p^2(t - x_r p_x)}. \tag{4.18}$$

Vertical two-way-traveltime of the reflection point is given by

$$t_o = \frac{2z_o}{v} = 2pz_o \tag{4.19}$$

Substitution of equations 4-19 into 4-18 gives the vertical two-way-traveltime of the reflection point in terms of offset, traveltime, effective slowness and local slopes

$$t_o = \frac{(t^2 - p^2 {x_r}^2)(p^2 - {p_x}^2)^{\frac{1}{2}}}{p(t - x_r p_x)}. \tag{4.20}$$

Using the migration coordinates/attributes (x_o, t_o), the oriented migration simply maps seismic data from the shot gather, where seismic amplitudes are a function of arrival time and receiver location, to the image gather, where amplitudes are sorted by the x_o and t_o attributes.

As mentioned before, given the imaging attributes (i.e. local slopes, two-way-traveltime, offset and local slopes) there is no need to extract imaging velocity and implement imaging, separately. It is done by the substitution of the effective slowness (equations 4.6) in the imaging equation (Equations 4-16 and 4-20). It maps seismic data from prestack domain to image domain, directly.

$$x_{o_i} = \frac{\frac{-{t_i}^2 p_{x_i}(x_{r_i}-x_{r_{i-n}})}{t_i p_{x_i}-t_{i-n}p_{x_{i-n}}} + 2t_i x_{r_i} - {x_{r_i}}^2 p_{x_i}}{2\left(t_i - x_{r_i}p_{x_i}\right)} \tag{4.21}$$

$$t_{o_i} = \frac{\left({t_i}^2 - \frac{t_i p_{x_i}-t_{i-n}p_{x_{i-n}}}{x_{r_i}-x_{r_{i-n}}}{x_{r_i}}^2\right)\left(\frac{t_i p_{x_i}-t_{i-n}p_{x_{i-n}}}{x_{r_i}-x_{r_{i-n}}} - {p_{x_i}}^2\right)^{\frac{1}{2}}}{\left(t_i - x_{r_i}p_{x_i}\right)\left(\frac{t_i p_{x_i}-t_{i-n}p_{x_{i-n}}}{x_{r_i}-x_{r_{i-n}}}\right)^{\frac{1}{2}}} \tag{4.22}$$

4.6. Implementation of the technique

Implementation of the proposed migration technique includes the following steps:

- Estimation of local event slopes (p_x) for each sample of every trace in a shot record,
- Estimation of migration slowness/velocity (p), by point-to-point mapping of data corresponding to the same wavefront using predictive painting technique,
- Estimation of migration attributes (x_o,t_o) in each shot record,
- Migration of seismic data in each shot record, and
- Stack of the all migrated shot gathers.

4.7. Application to a synthetic data example

To demonstrate separate steps involved in the proposed oriented prestack time migration technique, I applied it on a simple synthetic data example that includes one interface, generated by convolutional modelling. The velocity model used for modelling is shown in Figure 4.3. 50 synthetic shot records were generated using the acquisition parameters shown in Table 4.1.

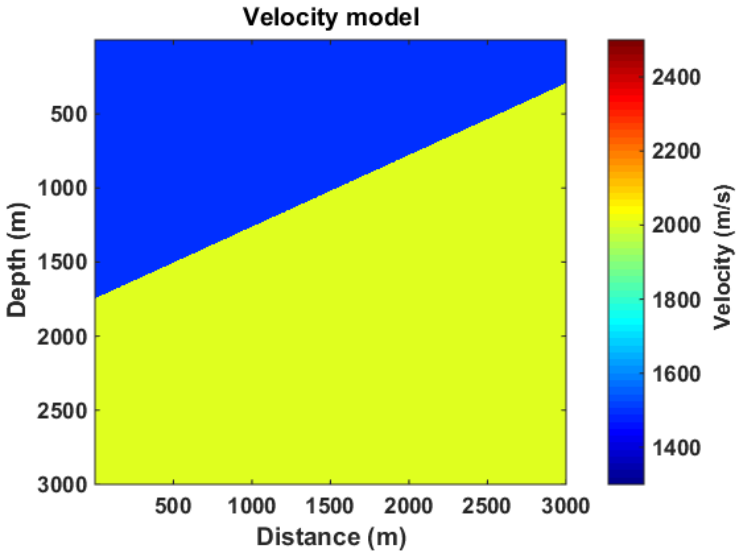

Figure 4.3: Velocity model used to generate synthetic data. Compressional velocities from top to bottom are 1500 and 3000 (m/s).

Maximum depth (m)	1745
Maximum distance (m)	3000
Sampling interval (ms)	2
Geophone spacing (m)	20
Number of receives per shot	101
Number of shot records	50
Maximum time in each record (s)	2.2
Ricker wavelet- Dom. Freq. (Hz)	15
Acquisition type	Off-end
Dip (degree)	16

Table 4.1: Acquisition parameters used to generate synthetic dataset by convolutional modelling.

Figures 4.4a-4.4b show the first shot record and the corresponding local slopes estimated by the application of global plane wave destructor, described in Fomel (2002). Figures 4.4c-4.4.d show the imaging slowness (p) and velocity (v) obtained by the application of equation 4.6, respectively. The distance between two traces were chosen (20-1)×receiver interval (n=20), for the point-to-point scanning using predictive painting. Given the estimated local slopes and imaging slowness (p), the migration attributes (x_o, t_o) were estimated, shown in Figure 4.4e-4.4f. Note that since the interface is linear the slowness computation is not affected by choice of n.

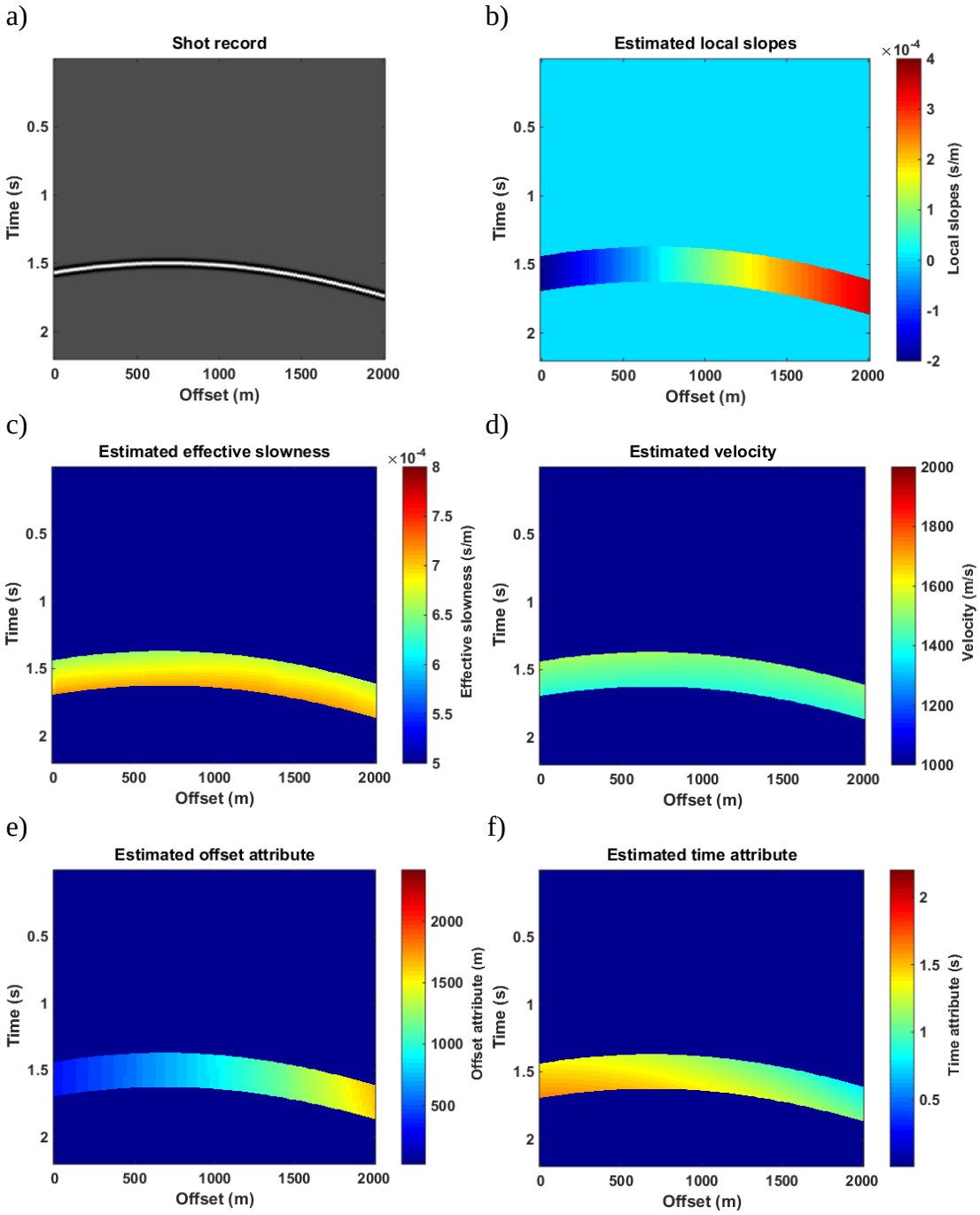

Figure 4.4: a) First shot record generated for the velocity model show in Figure 4.3 and the corresponding b) estimated slopes, c) effective slowness, d) effective velocity, e) offset and f) time attribute.

Using the estimated attributes computed by equations 4.16 and 4.20, seismic energy is migrated/mapped into image domain shown in Figure 4.5a. It is observed that the seismic event corresponding to the dipping reflector is very well imaged.

In the previous sections, it was mentioned that the proposed technique is the improved version of the previous oriented technique in common-source domain by Bóna (2011). To quantify this, I also included the results obtained by the application the previous approach, where migration slowness is given by

$$p^2 = {p_x}^2 + tp_{xx}\,. \tag{4.24}$$

Herein, p_{xx} denotes the second derivative of two-way-traveltime with respect to offset (curvature). The second derivative, which is the derivative of local slope with respect to offset, can be estimated by the straightforward application of chain rules (Bóna, 2011; Casasanta and Fomel, 2011), as follows:

$$p_{xx} = \frac{\partial p_x}{\partial x} + p_x \frac{\partial p_x}{\partial t}. \tag{4.25}$$

Given the local slopes and estimated curvatures, I estimated the migration slowness (p) using equation 4.24 followed by mapping the seismic data using migration equations 4.16 and 4.20. Figure 4.5b shows the corresponding migration results obtained by the application of the previous technique.

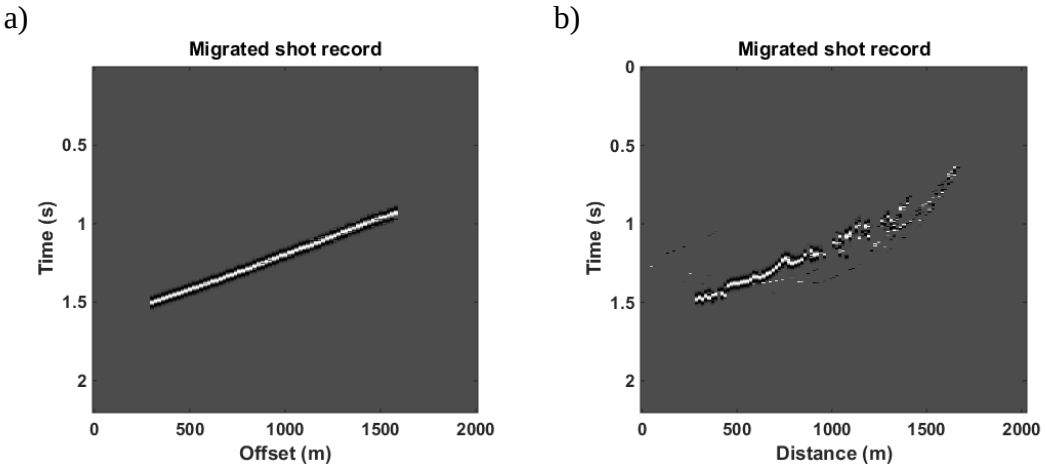

Figure 4.5: Migration results of a single common-shot record by implementing the a) proposed technique and b) previous technique (Bóna, 2011).

Based on the theory presented above, shot gathers are independent of each other in the proposed migration technique. Migration is applied to each shot gather separately; then, the migrated records are stacked to obtain the final image. Similar to normal-moveout correction, shallower events in longer offsets are stretched out in all oriented migration techniques. To preserve the frequency components of the migrated

events, one can mute the stretched energy by defining a certain threshold. In this example, I muted the migrated data by defining a migration aperture of 65 degree. Figures 4.6a-4.6b show two migrated sections by the application of the proposed technique and the previous technique, respectively. Each migration section is obtained by stacking of all 50 migrated shot records.

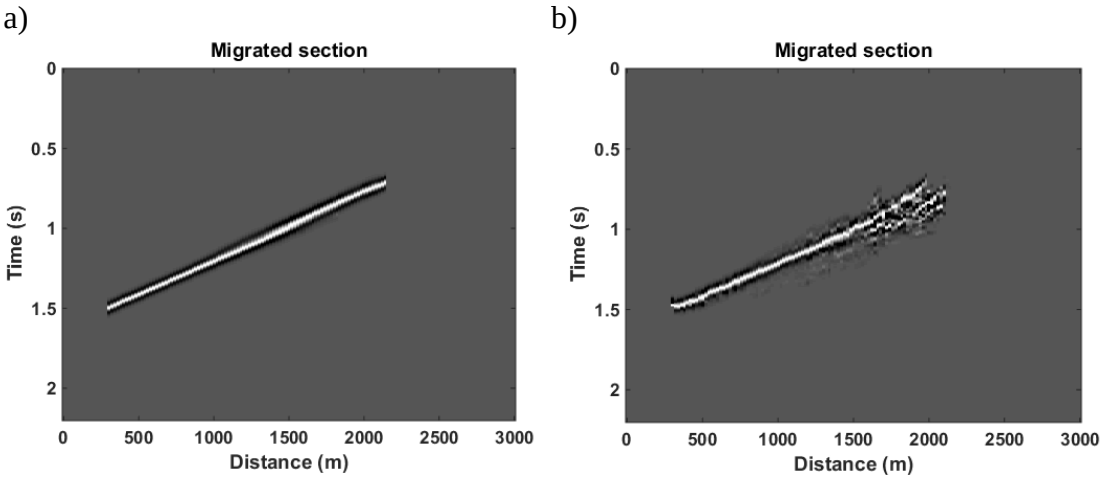

Figure 4.6: Migration sections after stack of all migrated common-shot records by implementing a) the proposed technique and b) the previous technique (Bóna, 2011).

Comparison of the results shows that the proposed technique aligns the seismic energy to the appropriate position of the dipping geological interface, whereas the previous technique does not completely map the interface to its position and distributes the seismic energy in the image space. More dispersion is expected to occur with offset due to larger errors in the estimation of the curvature in the previous approach (specifically by using numerical differentiation to estimate curvature).

The numerical errors in curvature estimation are due to the finite differences made by the use of numerical differentiation to estimate the spatial gradient components of the local slopes ($\frac{\partial p_x}{\partial x}$). The finite differences act as high-pass filters and increase the high-frequency noises, especially if the initial seismic data is noisy (Casasanta and Fomel, 2011). In other words, sampling along time axis is correct and differentiability condition is satisfied; however, in offset direction, it is not the case, specifically in far offset, where the curvature of the seismic events becomes linear. Taking spatial aliasing into account, curvature estimation will become more challenging.

4.8. Application to a field data example

Applicability of the proposed migration technique to field data is demonstrated on a 2D marine data recorded by Geoscience Australia in 1996 over North West Shelf, Western Australia. The 2D line includes 1371 shot records. The sampling interval was 2 ms and the record length is cut down to 2.7 s. Figure 4.7 shows the related zero offset section obtained by sorting the zero offset traces from each shot in the survey. To be consistent with the presented by Khoshnavaz et al. (2015) that used the same data set, the zero offset section and also all stacked migration sections are flipped.

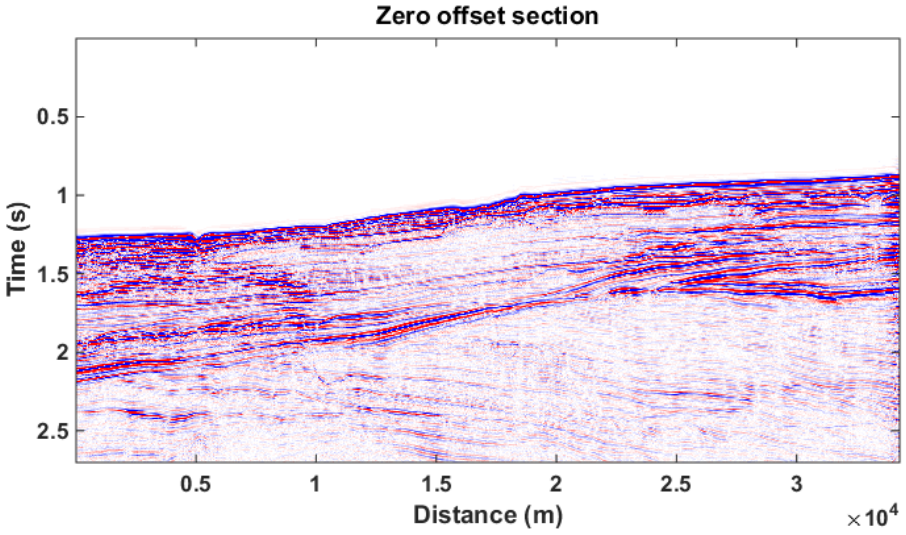

Figure 4.7: Zero offset section of the 2D marine data recorded by Geoscience Australia at North West Shelf, Western Australia by sorting the zero offset traces from each shot in the survey.

Figures 4.8a-4.8c show one of the 1371 shot gathers of the seismic survey, the corresponding estimated local slopes (p_x), and the estimate migration velocity, respectively. Figures 4.9a–4.9c show the estimated migration coordinates/ attributes (x_o, t_o), and the corresponding migrated shot record, respectively.

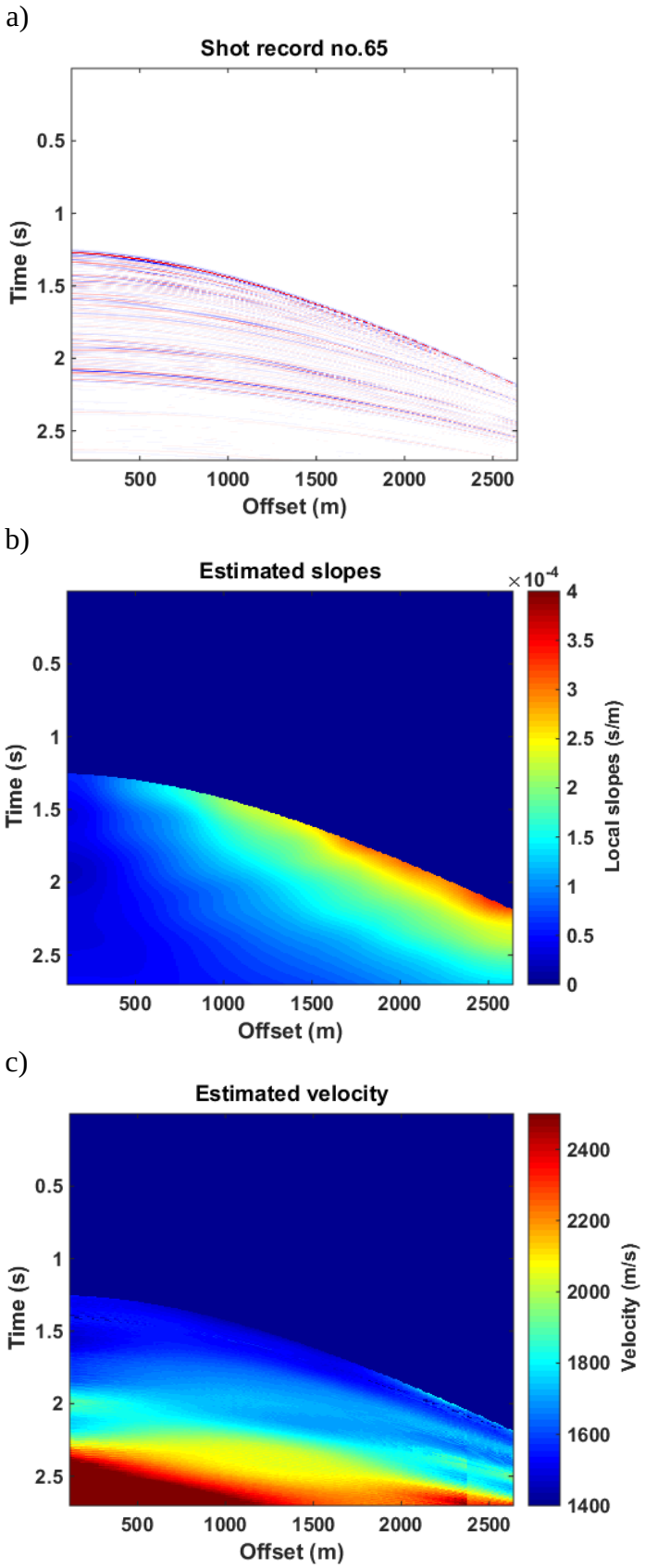

Figure 4.8: a) a shot record within the 2D marine acquisition, b) the estimated local slopes using plane wave destructor and c) the estimated migration velocity.

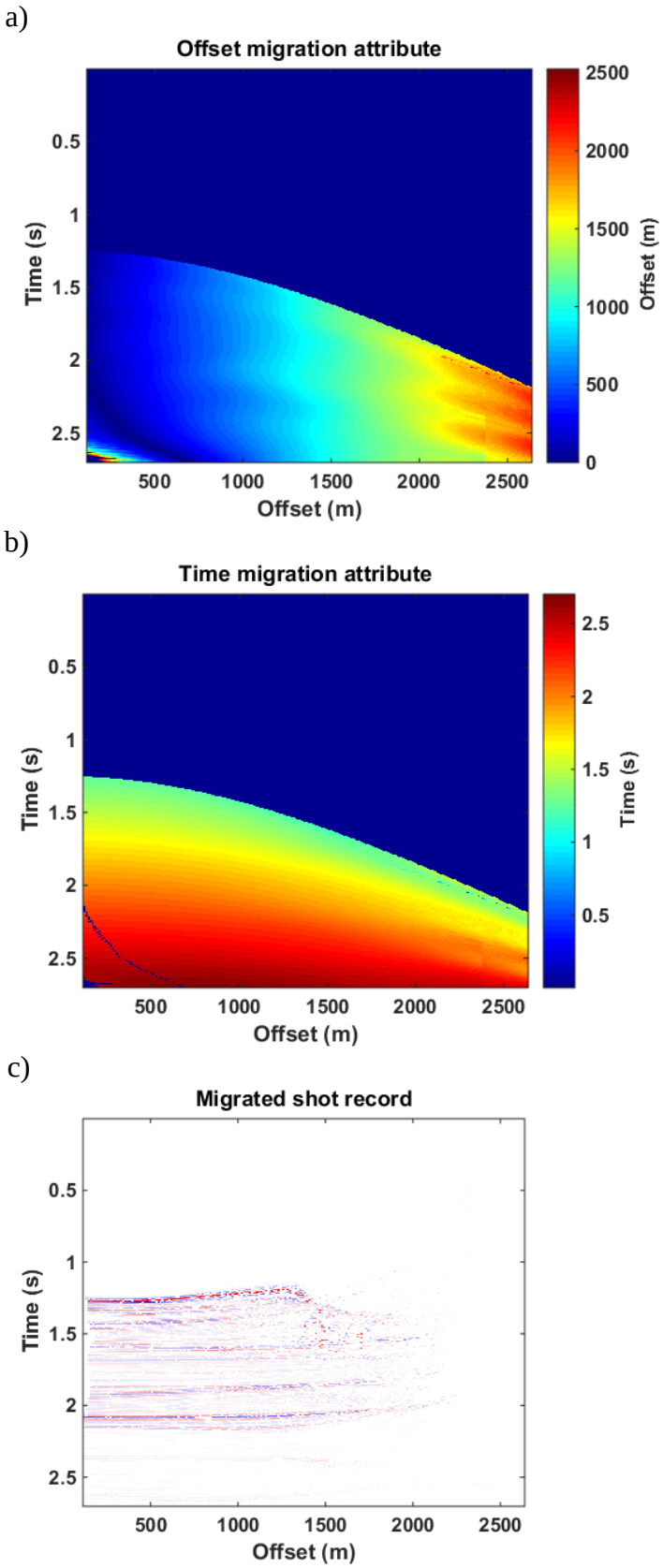

Figure 4.9: Migration a) time and b) offset attributes for the shot record shown in Figure 4.8a, and c) the corresponding migrated common-shot gather

Figure 4.10 shows the final migrated section obtained by stacking of all 1371 migrated shot gathers and Figure 4.11 shows the corresponding migration velocity, plotted the at the position of zero offset traces. I used a migration aperture of 50 degree.

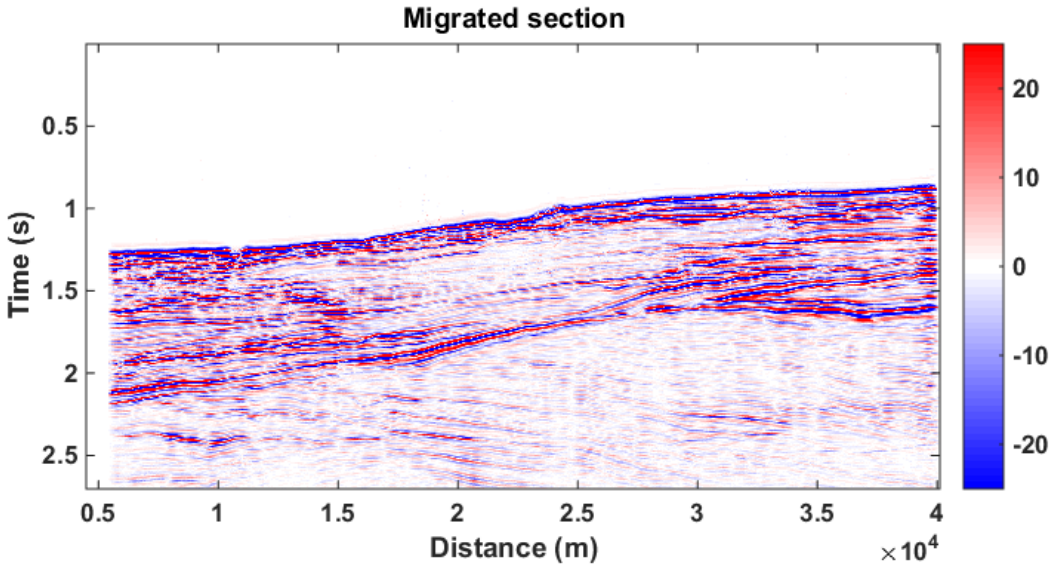

Figure 4.10: Final migrated section obtained by stacking of all 1371 migrated shot gathers in the survey.

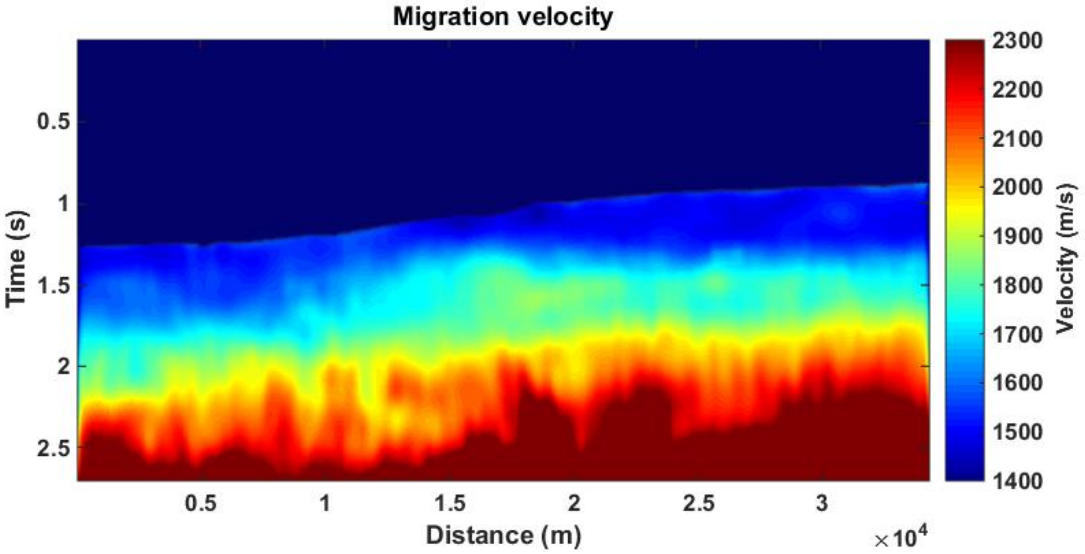

Figure 4.11: Smoothed migration velocity at the position of zero offset traces by the application of the proposed technique (equation 4.6).

Figures 4.12a-4.12b show the migrated sections by the application of the previous technique (Bóna, 2011); numerical differentiation (Bóna, 2011) and plane wave destructor (Fomel, 2002) were used to estimate the local slopes to obtain the migrated sections shown in Figures 4.12a and 4.12b, respectively.

a)

b)

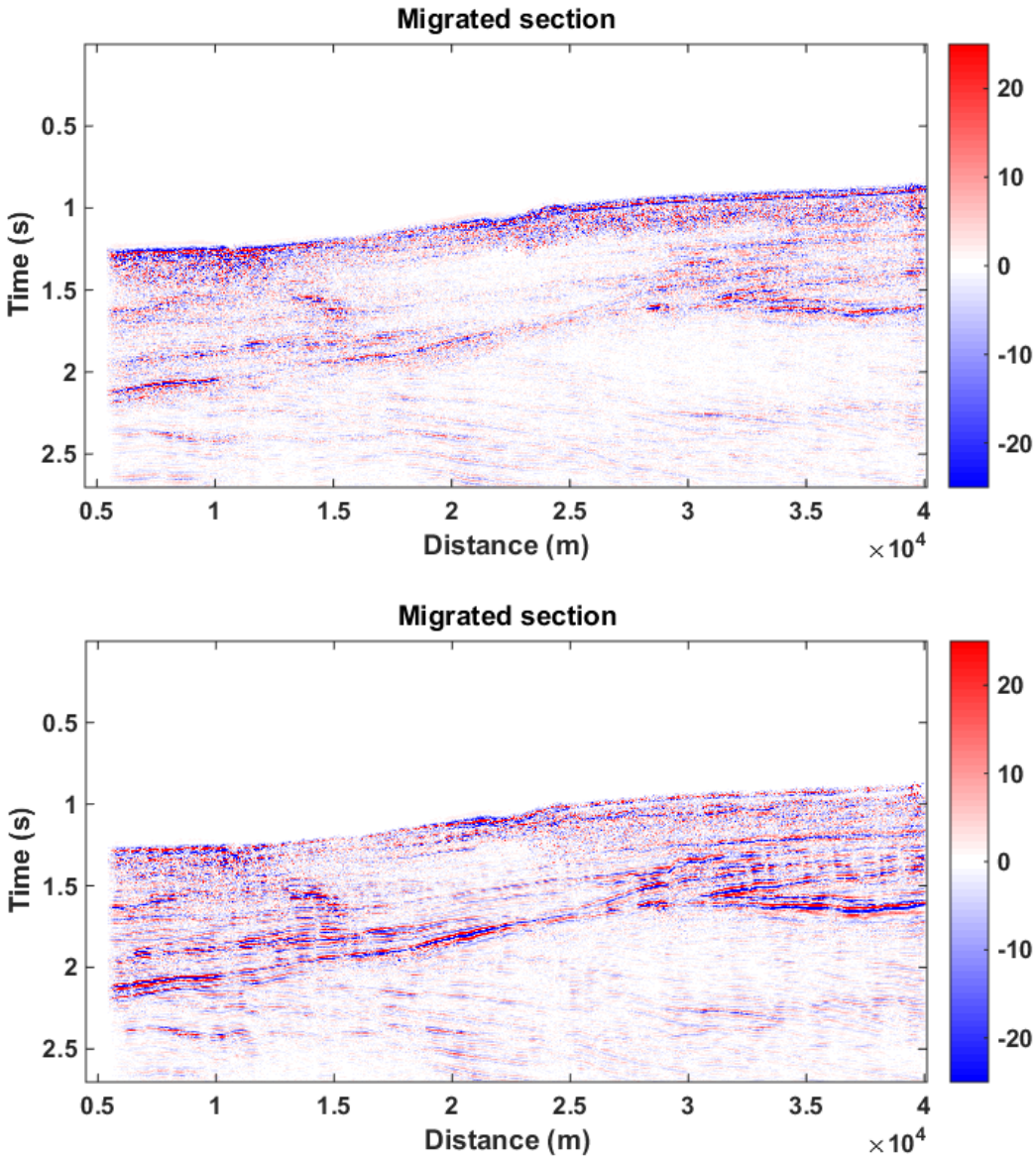

Figure 4.12: Final migrated sections by the application of previous technique (Bóna, 2011). Slopes were estimated by a) numerical gradient and b) plane wave destructor.

The standard Kirchhoff prestack time migration technique is also applied to the marine data set presented above. Figure 4.13a and 4.13b show the corresponding migration section and velocity model, respectively.

a)

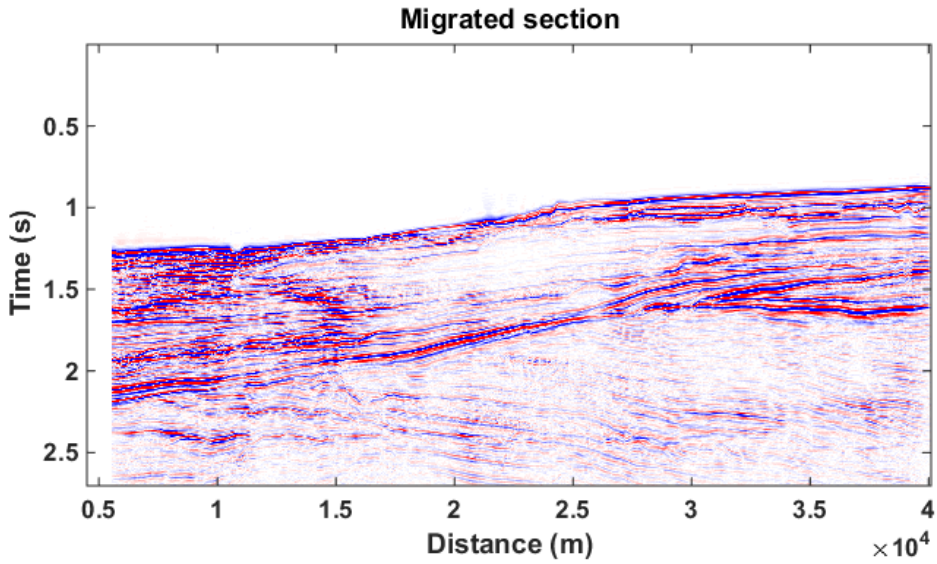

b)

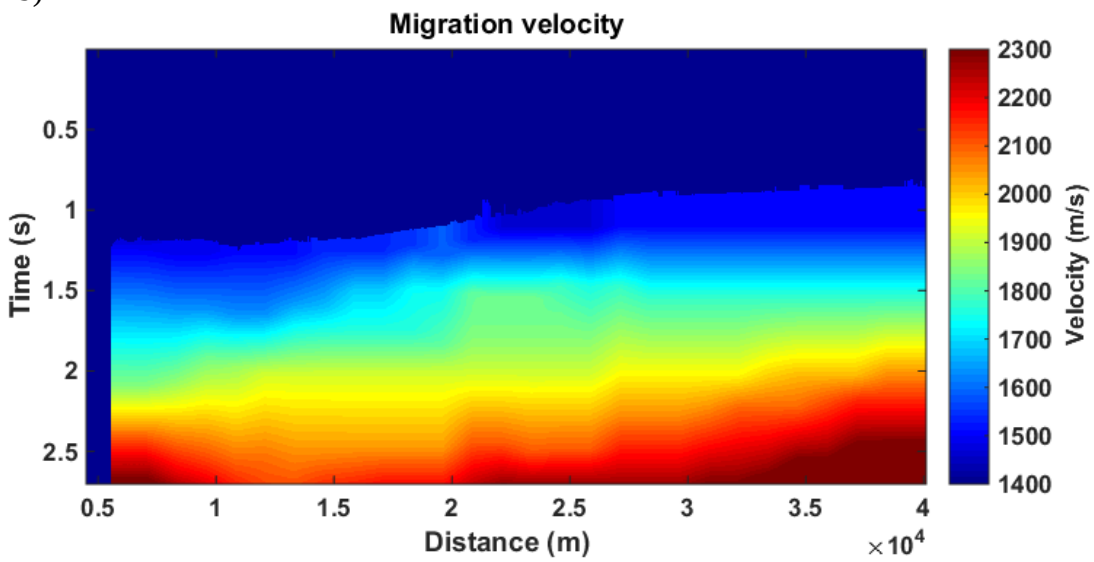

Figure 4.13: a) Migrated sections by the application of standard Kirchhoff prestack time migration technique and b) the corresponding smoothed velocity model.

In order to have a better comparison between the results, the upper-right side of the migrated sections are enlarged and shown in Figure 4.14.

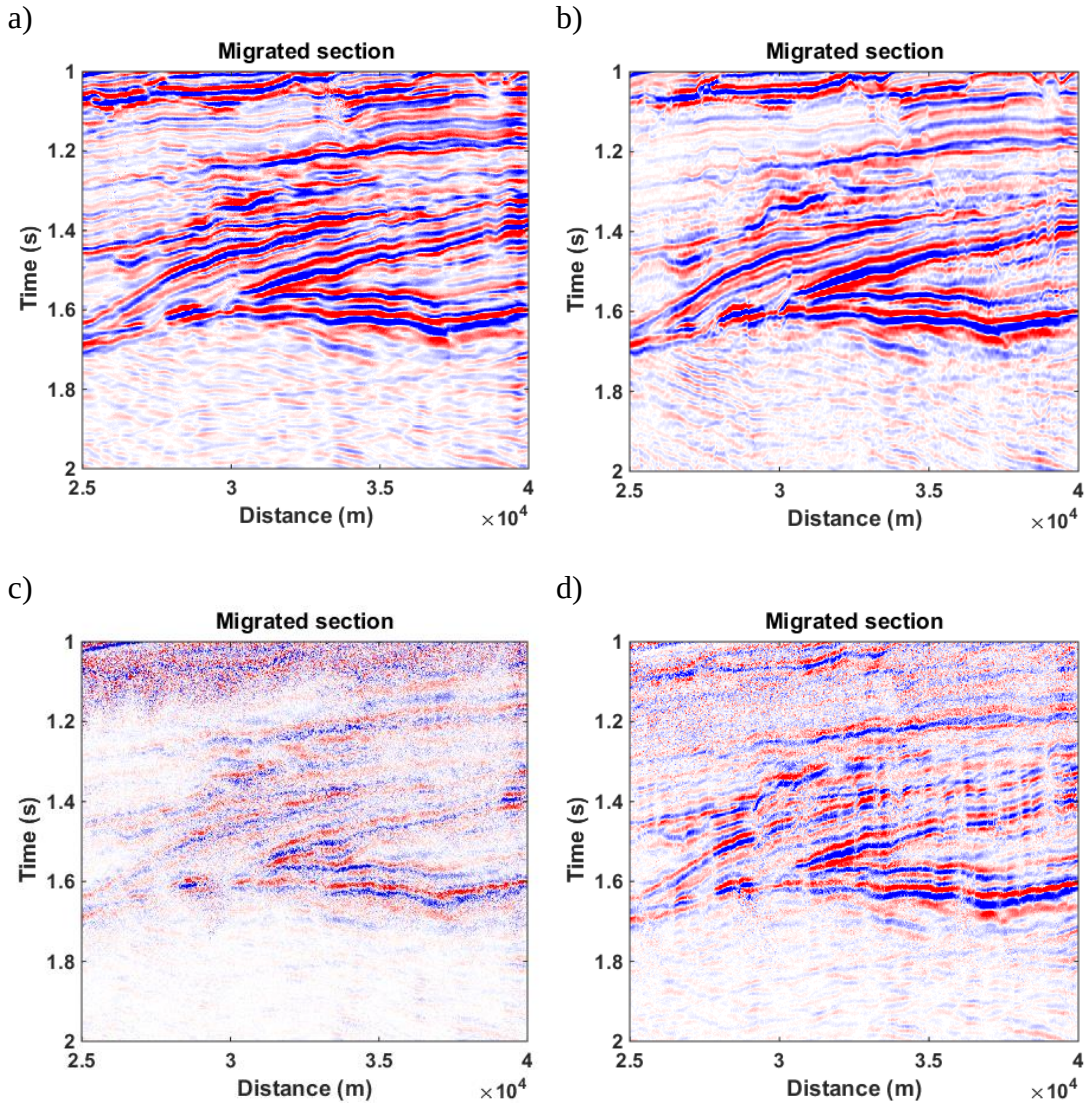

Figure 4.14: Enlarged migrated sections by the application a) proposed technique, b) standard Kirchhoff migration, and the previous oriented technique (Bóna, 2011) where local slopes were estimated by c) numerical gradient and d) plane wave destructor.

Comparison of the results presented above, demonstrates that the proposed migration technique produces better results than the method proposed by Bóna (2011). The continuity is greatly improved while high-frequency migration noise is reduced. It is also observed that the results obtain by the proposed migration technique are comparable with the results by standard Kirchhoff migration technique.

Estimation of local slopes using plane wave destructor improved the resolution of the final image obtained by the application of the previous technique (Figures 4.12b and 4.14d) over the use of numerical differentiation for local slope estimation (Figures 4.12a and 4.14c). It is because plane wave destructor relies on smoothing of the input seismic data and regularizing of the seismic data (Fomel, 2002).

4.9. Discussion

The proposed oriented migration technique was developed for imaging single common source gathers under the assumption of reflectors with small curvature in a common source gather. The estimation of migration velocity is done by point-to-point mapping of reflections corresponding to the same seismic wavefront. Seismic data used in the technique must be a pre-processed, excluding coherent noises/artifacts such as surface waves. Tangency between reflections and the coherent noises (and also strong diffractions) can cause partially over and/or under estimation of migration velocity, estimated by the application of predictive painting. One strategy that can increase the applicability of the proposed technique and increase the resolution of the final image is to use an oriented technique that separates diffractions and reflections in common-source domain (e.g., Taner et al., 2006), which was not the main concern of this chapter.

The presented technique is developed for continuous planar reflectors. Application of the technique for the situations with sharp faults and discontinuities may result in blur images in the area of discontinuity in each migrated shot record. It fairly addressed after stacking the migrated shot records; however, the seismic amplitudes would not be totally preserved in those areas.

The migration technique deals with direct arrivals. Consider equation 4.6 that explains the effective slowness of an event. For direct arrivals, the effective slowness would be equal to the local slopes and direct arrivals are dispersed in the image space.

Although there was no need for removing the direct arrivals from the shot records, we muted them from the field data to improve the performance of the plane wave destructor.

The velocity model, constructed by the application of the technique to the field data set was comparable with velocity model obtained by application standard Kirchhoff migration. In principle, there is a possibility to use the velocity model to remove/attenuate multiples, analogous to the algorithm described in Cooke et al. (2009). This remains to be tested in future. Another direct application of the presented method is to use the estimated velocity model as input to a standard time migration methods, or as a starting model for more modern imaging/inversion methods.

4.10. Conclusions

Local slopes in seismic data carry complete information to construct the migrated image. Given the local slopes, imaging velocities and attributes can be estimated to direct mapping of seismic data from prestack domain to image domain. A local slope based prestack time migration algorithm for planer reflectors in common-source domain was developed and successfully applied.

Important development achieved in this research is related to removing higher order derivatives of traveltime with respect to offset from the previous techniques. The need for higher order derivatives estimation is replaced by point-to-point mapping using predictive painting technique. The proposed technique is verified with numerical tests and field data. As the implementation of the techniques is relatively fast, a possible application is for real time imaging or imaging during acquisition. The road ahead is to remove coherent artefacts from data prior to application of the proposed technique.

4.11. References

Alkhalifah, T., and I. Tsvankin, 1995, Velocity analysis for transversely isotropic media: Geophysics, **60**, 1550–1566, doi:10.1190/1.1443888.

Bóna, A., 2011. Shot-gather time migration of planar reflectors without velocity model: Geophysics, **76**, no. 2, S93–S101.

Burnett, W., and S. Fomel, 2009b, Moveout analysis by time-warping: 79th Annual International Meeting, SEG, Expanded Abstracts, **28**, 3710–3714.

Casasanta, L., and S. Fomel, 2011. Velocity-independent τ-p moveout in a horizontally layered VTI medium, Geophysics, **76**, no. 4, U45-U47.

Claerbout, J. F., 1992, Earth soundings analysis: Processing versus inversion: Blackwell Scientific Publications.

Cooke, D., A. Bóna, and B. Hansen, 2009, Simultaneous time imaging, velocity estimation and multiple suppression using local event slopes: Geophysics, **74**, no. 6, WCA65–WCA73.

Fomel, S., 2002, Applications of plane-wave destruction filters: Geophysics, **67**, 1946–1960.

----------, 2007b, Velocity-independent time-domain seismic imaging using local event slopes: Geophysics, **72**, no. 3, S139–S147, doi: 10.1190=1.2714047.

----------, 2010, Predictive painting of 3D seismic volumes: Geophysics, **75**, no. 4, A25–A30, doi: 10.1190=1.3453847.

Fomel, S., and A. Stovas, 2010, Generalized nonhyperbolic moveout approximation: Geophysics, **75**, no. 2, U9–U18, doi:10.1190/1.3334323.

Khoshnavaz, M. J., Bóna, A., and Urosevic, M., 2015, Pre-stack time migration in common source domain without velocity model: In 77th EAGE Conference and Exhibition.

Landa, E., B. Gurevich, S. Keydar, and P. Trachtman, 1999, Application of multifocusing for subsurface imaging: Applied Geophysics, **42**, 283–300.

Ottolini, R., 1983, Velocity independent seismic imaging: Stanford Exploration Project, **37**, 59–68.

Riabinkin, L. A., 1957, Fundamentals of resolving power of controlled directional reception (CDR) of seismic waves, in L. Lu, ed., Slant-stack processing, 1991, SEG, 36–60. (Translated and paraphrased from Prikladnaya Geofiizika, 16, 3–36).

Rieber, F., 1936, A new reflection system with controlled directional sensitivity: Geophysics, 1, 97–106.

Schleicher, J., J. C. Costa, L. T. Santos, A. Novais, and M. Tygel, 2009, On the estimation of local slopes: Geophysics,

Taner, M.T., S. Fomel, and E. Landa, 2006, Separation and imaging of seismic diffractions using plane-wave decomposition: In 2006 SEG Annual Meeting. Society of Exploration Geophysicists, 2401-2405.

Yilmaz, O., 2001, Seismic data analysis: SEG.

5. Comparison of different traveltime approximations for vertical-transverse-isotropy media in context of poststack diffraction imaging

5.1. Overview

Diffractions carry valuable information about local discontinuities and small scale objects in the subsurface. They are typically not often used in the process of geological interpretation. Many diffraction imaging techniques have been developed and applied for isotropic media while relatively few techniques have been developed for anisotropic media. Ignoring anisotropy can result in low resolution images with wrongly positioned or spurious diffrators. Hence, I suggest to take anisotropy into account, initially in 2D poststack domain by considering P-wave non-hyperbolic diffraction traveltime approximations for vertical-transverse-isotropy media. Accuracy of final images is directly connected to the accuracy of diffraction traveltime approximations. Therefore, accuracy of six different approximations, including hyperbolic normal moveout approximation, is quantified by numerical experiments.

5.2. Introduction

Other than the reflected seismic energy traditionally used in exploration seismology, there is also scattered/diffracted energy or simply diffractions present in seismic data. Diffractions carry valuable information about the local discontinuities and small scale objects; however, they are rarely used in the process of geological interpretation. In conventional seismic methods, diffractions are often identified by visual observation of an interpreter and the reliability of such identification is low and very subjective (Landa and Keydar, 1998). Therefore, it is important to use more objective process that would utilise the information carried by diffractions.

Several diffraction imaging techniques have been developed and applied based on the assumption of wave propagation through isotropic media (e.g., Khoshnavaz et al., 2015; Bóna et al., 2015); however, in presence of anisotropy the assumption fails and results in low resolution images with wrongly positioned or spurious diffrators. Therefore, anisotropy should be considered in diffraction imaging. Dell et al., (2013) developed a general double-square-root equation to estimate diffraction traveltime for anisotropic media that requires three inputs, all in terms of the second derivatives of ray velocity with respect to its ray angle. Although their technique is developed for arbitrary and strong anisotropy, the second derivative estimation is difficult to achieve with great accuracy.

I first evaluate the accuracy of 2D post-stack diffraction imaging using different non-hyperbolic diffraction traveltime approximations for vertical-transverse-isotropy (VTI) media. The analysis includes shifted hyperbola approximation (Malovichko, 1978), acceleration approximation (Taner et al., 2005), three-parameter approximation (Blias, 2009), rational approximation (Alkhalifah and Tsvankin, 1995) and generalized moveout approximation (GMA), developed by Fomel and Stovas (2010). These approximations have an extra term (η) that is related to the anellipticity of seismic wavefront caused by anisotropy. Among all the approximations, it was observed that application of GMA (Fomel and Stovas, 2010) results in the highest accuracy. This was previously observed by Asgharzadeh et al. (2014) in the inversion of NMO velocity and η. Similar to Landa and Keydar (1998), I compute semblance (Taner and Koehler, 1969) along diffraction traveltime curves to search for diffracted energy in seismic data. I applied the diffraction imaging technique with and without separation of diffractions and reflections. I separated them by dip filtering using plane wave destructor (Fomel, 2002).

5.3. Methodology

The first step was to compute anisotropic diffraction traveltime using the NMO velocity (v_{nmo}) and anellipticity parameter (η) estimated from reflection seismic. The approximations evaluated here are

- Hyperbolic normal moveout:

$$t^2 = {t_0}^2 + \frac{x^2}{{v_{nmo}}^2} \tag{5.1}$$

- Shifted hyperbola, Malovichko (1978):

$$t = t_0 \left[1 + \frac{\sqrt{1+(1+8\eta)\tilde{x}^2}-1}{1+8\eta}\right] \tag{5.2}$$

- Acceleration, Taner et al. (2005):

$$t^2 = {t_0}^2 \left(1 + \frac{\tilde{x}^2}{1+2\tilde{x}^2\eta}\right) \tag{5.3}$$

- Three-parameter, Blias (2009):

$$t^2 \cong \frac{{t_0}^2}{2} + \frac{x^2}{v^2} + \frac{1}{2}\sqrt{{t_0}^2 + \frac{8\eta x^4}{v^4}} \tag{5.4}$$

- Rational, Alkhalifah and Tsvankin (1995):

$$t^2 = {t_0}^2 \left(1 + \tilde{x}^2 - \frac{2\tilde{x}^4\eta}{1+(1+2\eta)\tilde{x}^2}\right) \tag{5.5}$$

- GMA, Fomel and Stovas (2010):

$$t^2 = {t_0}^2 \left(1 + \tilde{x}^2 - \frac{4\tilde{x}^4\eta}{1+B\tilde{x}^2+\sqrt{1+2B\tilde{x}^2+C\tilde{x}^4}}\right) \tag{5.6}$$

herein, t_0 and x denote vertical two-way-travel-time and offset, $\tilde{x} = x/v_{nmo}t_0$ is normalized offset (Golikov and Stovas, 2012), and $B = \frac{1+8\eta+8\eta^2}{1+2\eta}$ and $C = \frac{1}{(1+2\eta)^2}$ in equation 5.6. If the separation of diffracted and reflected energy is important, e.g. for migration of diffractions, the next step is to separate them. In the second example, I separate them using dip filtering by the application of plane wave destructor (Fomel, 2002). The final step is to search for diffracted energy using semblance proposed by

Taner et al. (1969). The graph of semblance, obtained by scanning all the space for all possible diffractors, is called D-section. The higher the semblance, the higher the diffractivity in D-section.

5.4. Synthetic data example 1

In this example, following similar approach described in Bóna et al. (2008), I generated a zero-offset section for a point diffractor fixed in a constant velocity medium with the P-velocity of 2000 m/s and the effective η of 0.2 (Figure 5.1). The apex of the diffraction is at t=0.5 s and x=1500 m. Sampling interval and geophone spacing of 1 ms and 25 m were used to generate the data, respectively. A Ricker wavelet with the dominant frequency of 30 Hz is used for modelling.

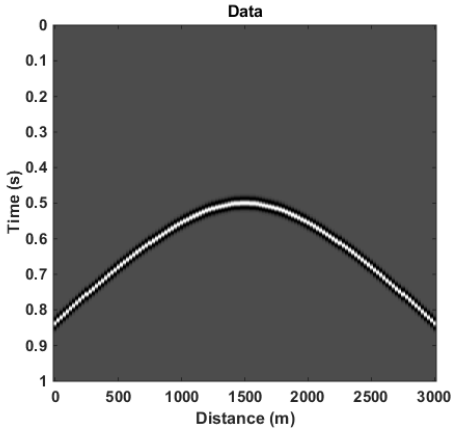

Figure 5.1: A synthetic non-hyperbolic zero offset record including a diffraction.

Figures 5.2a-5.2f show the D-sections obtained by the application of 2D poststack diffraction imaging using hyperbolic normal moveout, shifted hyperbola, rational, acceleration, three-parameter and GMA approximations, respectively.

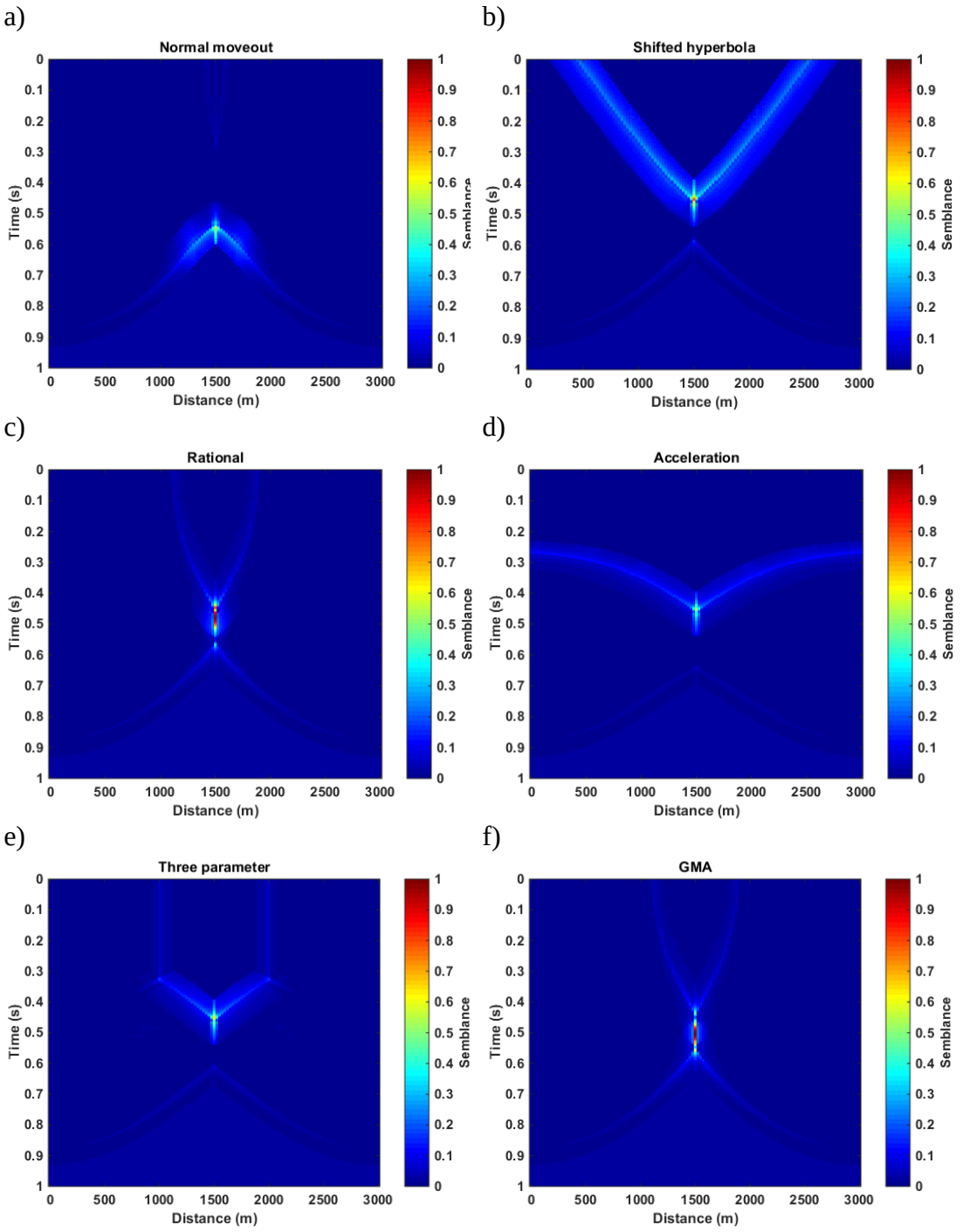

Figure 5.2: D-sections computed f a) hyperbolic moveout, b) shifted hyperbola, c) rational, d) acceleration, e) three-parameter, and f) GMA approximations.

Based on the results shown in Figure 5.2, diffractivity is weak and the diffractor is misplaced by the application of hyperbolic normal moveout, shifted hyperbola, acceleration and three-parameter approximations. The result obtained from rational and GMA approximations have higher diffractivity compared to other approximations.

However, the only approximation that locates the diffractor correctly is GMA approximation while rational approximation shifts the diffractor up in time.

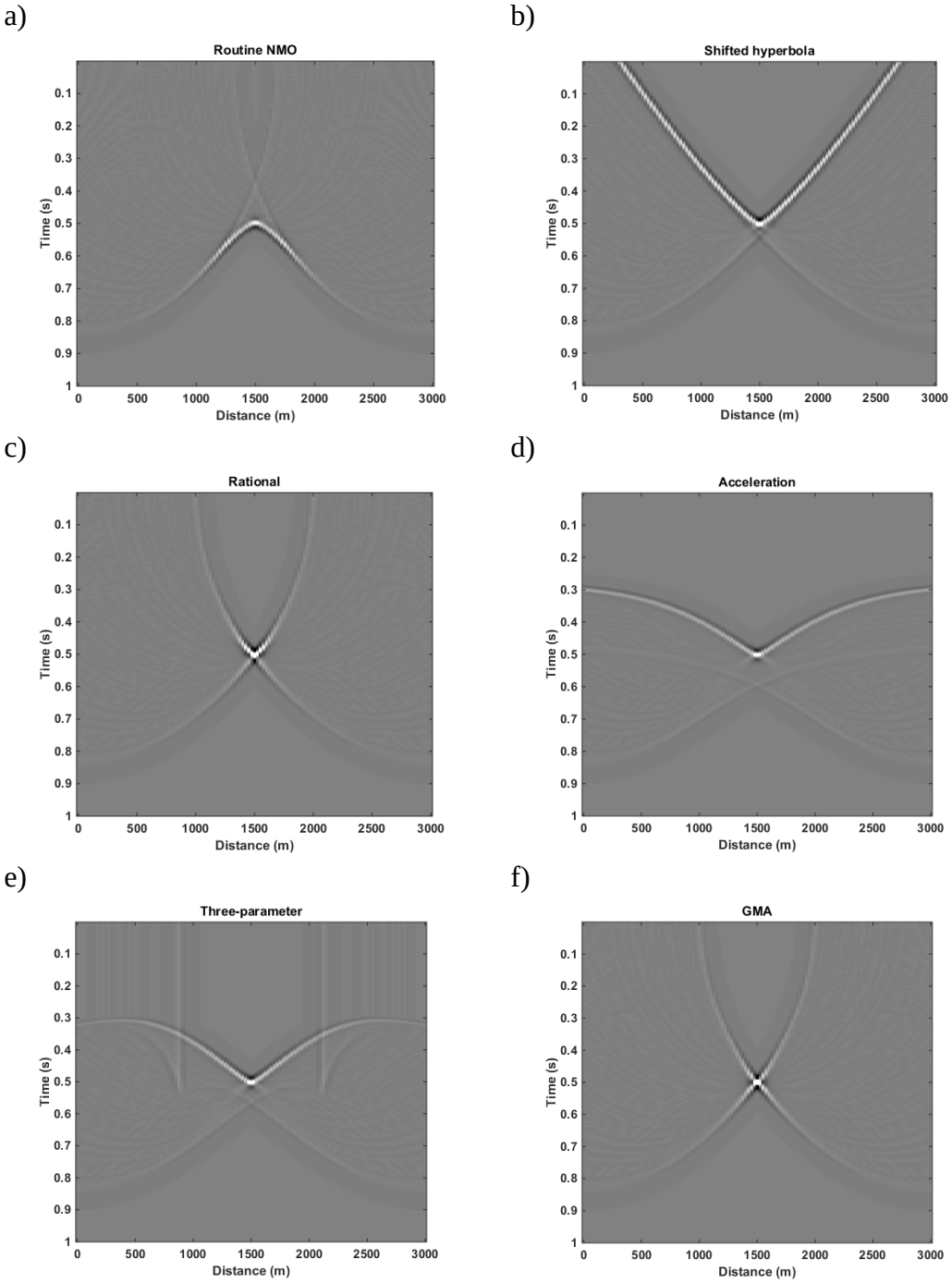

Figure 5.3: Migration results based on a) hyperbolic moveout, b) shifted hyperbola, c) rational, d) acceleration, e) three-parameter, and f) GMA approximations.

In the next part, I migrated the diffraction by Kirchhoff approach. Figures 5.3a-5.3f show the application of 2D poststack diffraction imaging using hyperbolic normal moveout, shifted hyperbola, rational, acceleration, three-parameter and GMA

approximations, respectively. The migration results from rational and GMA approximations show that the diffracted energy is better focused in comparison with to other approximations. To have a better comparison and to quantify the accuracy of different approximations, I plotted the diffraction traveltime curves computed for the point located at the position of the diffractor in time (Figure 5.4a).

a)

b)

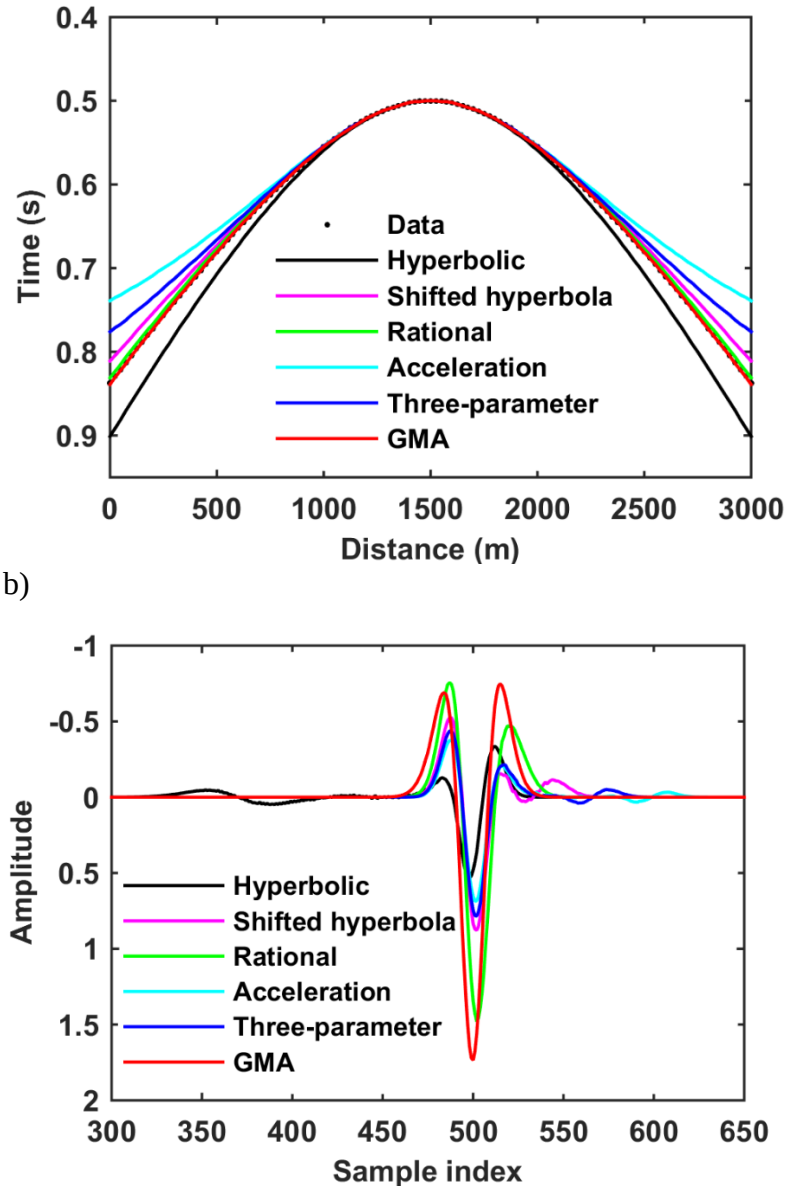

Figure 5.4: a) Diffraction traveltime curves using different approximations for the point located at the position of the diffractor in time and b) the central seismic traces of the migration sections.

Traveltimes computed from GMA and Rational approximation have the best fit to the true traveltime curve computed in forward modelling, respectively. Figure 5.4b shows the plot of the central seismic trace of the migration sections. The ultimate observation is that application of GMA preserve both phase and amplitude of the diffracted energy. Hence, once the most accurate approximation (GMA) is identified, it will be used for further analysis.

5.5. Synthetic data example 2

The second 2D numerical experiment includes a multi-layered model. Hyperbolic normal moveout and GMA approximations are used to compute diffraction traveltime and the corresponding results. Figures 5.5a-5.5c show interval velocity and interval η, respectively.

a)

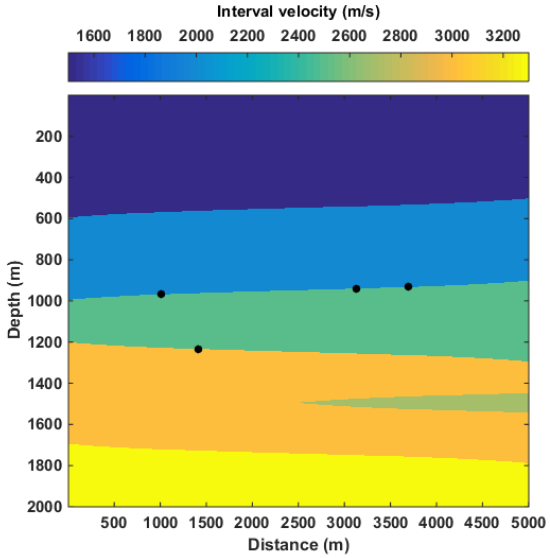

b)

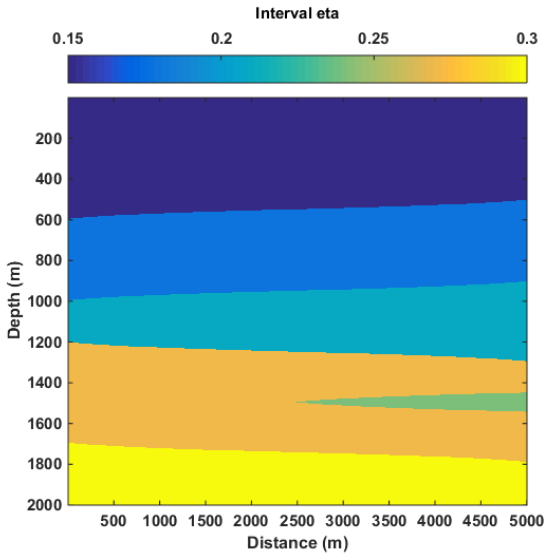

Figure 5.5: Interval a) velocity and b) η used to generate synthetic data. Black dots indicate point diffractors located on the layers.

Figure 5.6 shows the corresponding zero-offset modelled data. Using the interval parameters, RMS/effective velocity and η were measured for diffraction traveltime computation.

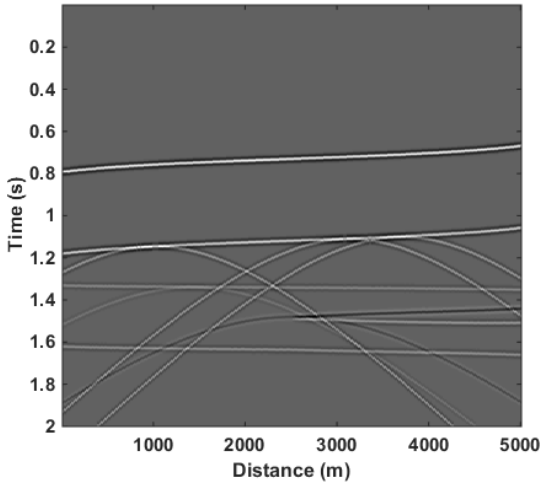

Figure 5.6: Zero offset section generated based on the interval velocities and interval ηs shown in Figure 5.5.

Figures 5.7a and 5.7b show the application of the technique to the data using hyperbolic normal moveout and GMA approximations, respectively. It is observed that the result obtained from GMA approximation have higher diffractivity with better localization in comparison with hyperbolic normal moveout approximation. Using GMA, I also applied the technique to the separated diffractions from reflections that were separated by dip filtering using plane wave destructor (Fomel, 2002). Figure 5.7c shows the corresponding result. Although separation of diffractions and reflections removes the effect of reflections in D-section, however, some useful information will also be removed from data. The two diffractors located in the bottom part of the data in Figure 5.7c have weaker semblance in comparison to Figure 5.7b.

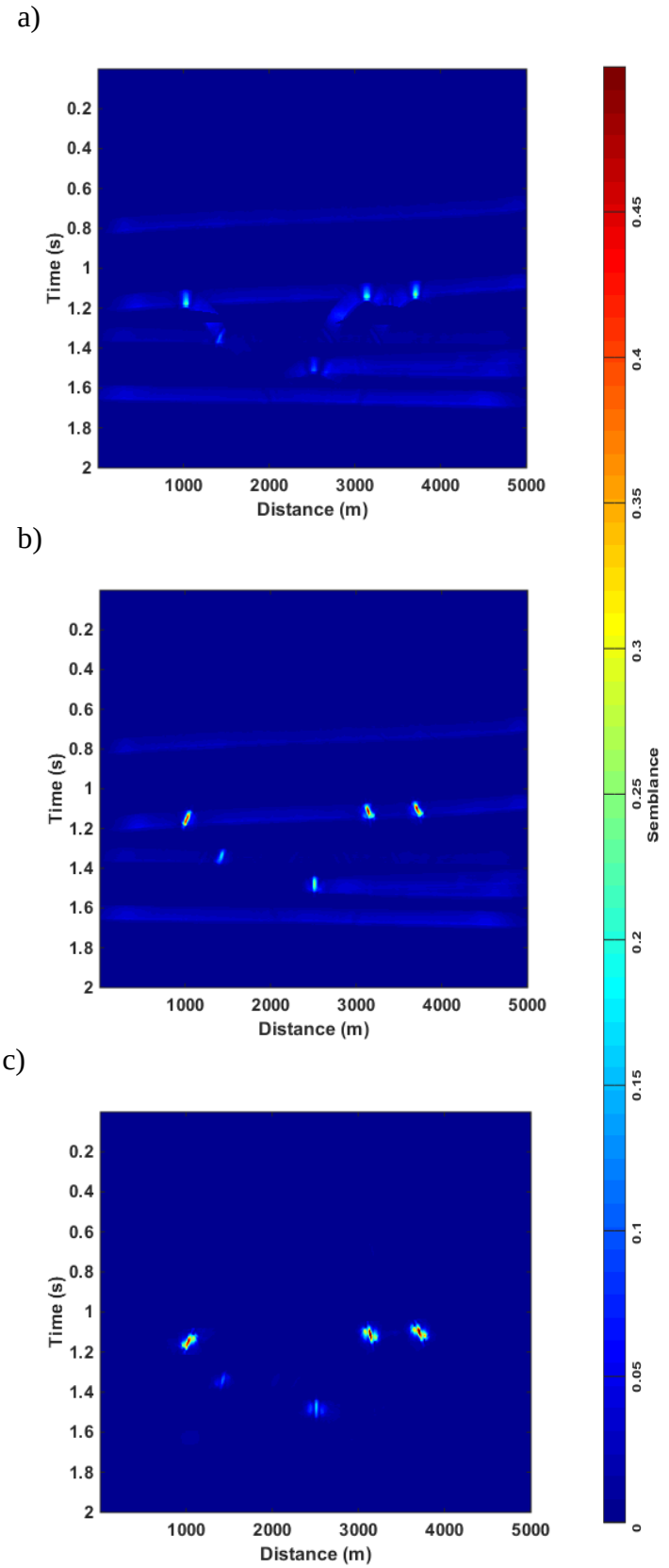

Figure 5.7: a) D-section computed based on hyperbolic moveout approximation. D-section computed for GMA b) without and c) with separation of diffractions and reflections.

5.6. Conclusions

It is suggested to consider anisotropy in post-stack domain by considering P-wave non-hyperbolic diffraction traveltime approximations for VTI media. It is shown that application of hyperbolic normal moveout traveltime approximation in the presence of anisotropy results in low resolution image, weak diffractivity and misplacement of diffractors in D-sections. I also compared the accuracy of different anisotropic diffraction traveltime approximations. Among the approximations presented in the main text, GMA has the highest accuracy while acceleration approximation has the lowest. Although separation of diffractions and reflections removes the effect of reflections in D-section, it leads to lose of useful energies omitted at the apexes of diffraction curves. The next step is to apply the presented approach to field data sets.

5.7. References

Alkhalifah, T., and Tsvankin, I. [1995] Velocity analysis for transversely isotropic media. *Geophysics*, **60**(5), 1550–1566.

Asgharzadeh, M., Nadri, D., and Bóna, A. [2014]. Inversion Based Accuracy Comparison of Nonhyperbolic Moveout Approximations for P-waves in VTI Media. *76th EAGE Conference & Exhibition*, Extended Abstracts, We D201 06.

Blias, E. [2009] Long-offset NMO approximations for a layered VTI model. Model study: *79th SEG Technical program*, Expanded Abstracts, 3475–3479.

Bóna, A., and Pevzner, R., [2015] Using Fresnel Zone to Characterise and Image Different Types of Diffractors in Low S/N Situations., *77th EAGE Conference & Exhibition* Extended Abstracts.

Bóna, A., Bucataru, I., and Slawinski, A. [2008] Inversion of ray velocity and polarization for elasticity tensor. *Journal of applied Geophysics*, **65**, 1-5.

Dell, S., Pronrvich, A., Kashtan, B., and Gajewski, D. [2013] Diffraction traveltime approximation for general anisotropic media. *Geophysics* **78**(5), WC15-WC23.

Fomel, S. [2002] Applications of plane-wave destruction filters. *Geophysics*, **67**, 1946–1960.

Fomel, S., and Stovas, A. [2010] Generalized nonhyperbolic moveout approximation: Geophysics, **75** (2), U9–U18.

Golikov, P. and Stovas, A. [2012] Accuracy comparison of nonhyperbolic moveout approximations for qP-waves in VTI media. *Journal of Geophysics and Engineering*, **9**, 428-432.

Khoshnavaz, M.J., Bóna, A., Urosevic, M., Ziramov, S. and Ahmadi P. [2015] Pre-stack diffraction imaging and its application in hard rock environment. *77th EAGE Conference & Exhibition*, Extended Abstracts.

Landa, E., and Keydar, S. [1998] Seismic monitoring of diffraction images for detection of local heterogeneities. *Geophysics*, **63**(3), 1093-1100.

Malovichko, A.A. [1978] A new representation of the traveltime curve of reflected waves in horizontally layered media: *Applied Geophysics* (in Russian), **91**, 47–53. English translation in C. H. Sword, 1987, A Soviet look at datum shift, SEP-51: Stanford Exploration Project, 313–316, accessed 26 January 2010.

Taner, M.T., and Koehler, M. [1969] Velocity spectra-digital computer derivation applications of velocity functions. *Geophysics* **34**(6), 859-881.

Taner, M. T., Treitel, S., and Al-Chalabi, M. [2005] A new travel time estimation method for horizontal strata. *75th SEG Technical program*, Expanded Abstracts, 2273–2276.

6. Diffractivity, another attribute for the interpretation of seismic data in hard rock environment

6.1. Overview

The concept of diffractivity presented in the previous chapter is of particular interest to the application of seismic for the mineral as well as the oil and gas exploration. In this environment, here for simplicity referred to as “hard rock” environment, the complex and in general “fractal” characteristic of the geology typically produces significant quantity of scattered seismic energy. These could be used to detect and analyse fracture zones, small-scale geobodies, intrusions and steeply dipping structures that are often associated with mineral deposits. Prospecting in such environments using seismic reflection methods is more challenging than in sedimentary settings due to high degree of heterogeneity causing lack of continuous reflector and steeply dipping formations and structures causing scattering of seismic energy. These scatterers can be traced back to irregular and often “sharp-shaped” mineral bodies, magmatic intrusions, faults and complex and heterogeneous shear zones.

Due to the natural lack of reflectors and abundant number of diffractors, there are only few case studies of diffraction imaging in hard rock environments. There are with almost no theoretical models or field examples of diffraction imaging in prestack domain. The research presented attempts to utilise diffractions for an improved rock characterisation. For that purpose, I calculated the diffractivity by computing the semblance of seismic data along diffraction traveltime curves in prestack domain. The performance of the method is demonstrated on a synthetic case and a field seismic data set collected over Kevitsa mineral deposit in the northern Finland. The high resolution results obtained by the application of prestack diffraction imaging suggest that diffractivity is a robust attribute that can be used in addition to other seismic attributes for the interpretation of seismic data in hard rock environment.

6.2. Introduction

In routine seismic exploration, reflections are used to infer subsurface structures and stratigraphy. Diffractions that carry valuable information about the local discontinuities and small scale objects of different shapes, are rarely used in the process of geological interpretation (Papziner and Nick 1998). In conventional seismic methods, diffractions are often identified by visual observation of an interpreter and the reliability of such identification is low and very subjective (Landa and Keydar 1998). Therefore, it is important to develop more objective methods to identify and interpret the information carried by diffractions present on 2D seismic sections or 3D data volumes.

The aim of diffraction imaging is to detect diffractors formed by small scale objects and sharp geological discontinuities such as termination of mineralized rocks and edges. Diffraction imaging can be performed in both post and prestack domain. Within the last few decades, a massive volume of literature has been done in diffraction imaging in the context of velocity analysis, seismic imaging and interpretation (e.g., Trorey, 1977; Harlan et al., 1983; Landa et al., 1987; Kanasewich and Phadke, 1988; Landa and Keydar, 1998; Khaidukov et al., 2004; Veeken et al., 2004; Sava et al., 2005; Vermeulen et al., 2006; Fomel et al., 2007; Klem-Musatov, 2008; Moser and Howard, 2008; Dell and Gajewski, 2011; Alonaizi et al., 2013; Rauch-Davieset et al., 2013; Merzlikin and Fomel, 2015). Importance of diffraction imaging to detect small scale objects and local discontinuities in the exploration of mineral deposits was first studied by Bóna et al. (2013). They applied a poststack diffraction imaging technique proposed by Landa and Keydar (1998) to a data set collected in hard rock terrains. In such technique a common-diffractor image, which is also known as D-section or D-volume (Landa et al., 1987), is constructed by computing semblance along diffraction traveltime curves.

In sedimentary basin settings, diffractions are mostly masked by reflections in seismic data. Several techniques have been proposed to separate diffracted energy from reflected energy in seismic data in both post and prestack domains (e.g., Taner et al., 2006; Fomel et al., 2007; Klokov and Fomel, 2012). However, in hard rock

environments the acquired seismic data is not often dominated by reflections. Hard rock environments are characterized by very complex structural and tectonic setting comprising numerous steeply dipping to vertical faults, fractures, shear zones, alterations and a variety of intrusions with complex shapes and various compositions. Lack of prominent marker horizons and intrinsic heterogeneity of the hard rock media cause the seismic waves to scatter in all directions and this often obscures the primary reflections received from the target of interest (L'Heureux et al., 2005). The spatial dimensions of the ore-bodies are often smaller than the Fresnel zone associated with the seismic source frequencies and depth of the deposit (Eaton et al., 2003). Consequentially, ore deposits generally fall within the Mie-scattering domain. Adam et al. (1997), Milkereit et al. (2000), Gingerich et al. (2002) and Eaton et al. (2003) showed that a concentrated ore deposit could behave as a prominent seismic scatterer. Whilst Milkereit et al. (1996) also observed diffraction-like events caused by ore lens. Eaton (1999) and Salisbury et al. (2000) showed that in hard rock terrains, the steeply dipping targets typically behave as point sources or scatterers rather than continuous reflectors. That is why separation of diffractions from reflections may not be necessary in hard rock environment.

In hard rock environments, there is often no considerable lateral velocity change and the assumption of waves propagating with a constant effective velocity is valid for these environments. In these situations, scattering of seismic energy is due to the relatively large contrast in density (Gibson, 2011; Urosevic et al., 2012; Harrison et al., 2012).

Khoshnavaz et al. (2015) applied a 2D prestack diffraction imaging method to a hard rock seismic data set. Their 2D analysis results in low resolution images as limited amount of seismic data was used. In this chapter, similar technique is applied, but to a 3D data set collected over hard rock environment. Given the observable lack of strong reflectors in the data, I did not separate diffractions from reflections. In so doing, I computed the diffractivity by computing the semblance of the seismic data along diffraction traveltime curves in prestack domain. I showed that the diffractivity obtained from 3D diffraction imaging is a robust attribute for identifying, detecting and locating the source of diffractions generated from highly fractured zones, termination of mineralized rocks and the edges of vertical intrusions.

6.3. Methodology

The 3D prestack diffraction imaging technique used in this chapter followed the two steps:

- Computation of diffraction traveltime using known imaging velocity, and
- Construction of diffraction image gather (D-section) using semblance.

The diffraction traveltimes are computed by considering the diffraction ray path for a point diffractor (*D*) fixed in a constant velocity medium shown in Figure 6.1, diffraction traveltime in the source-receiver-offset space is given by the double square root equation for all possible sources and receivers in a 3D seismic survey (Claerbout 1985)

$$t = \sqrt{\frac{{t_0}^2}{4} + \left(\frac{x_D - x_S}{v}\right)^2 + \left(\frac{y_D - y_r}{v}\right)^2} + \sqrt{\frac{{t_0}^2}{4} + \left(\frac{x_D - x_S}{v}\right)^2 + \left(\frac{y_D - y_r}{v}\right)^2}. \quad (6.1)$$

Herein, (x_S, y_S), (x_R, y_R) and (x_D, y_D) denote the horizontal coordinates of sources, receivers and the point diffractor, respectively. v and t_0 are effective velocity and vertical two-way-travel-time, respectively. The effective velocity (v) can be estimated through seismic velocity analysis of reflection data (e.g., semblance analysis and constant velocity stack).

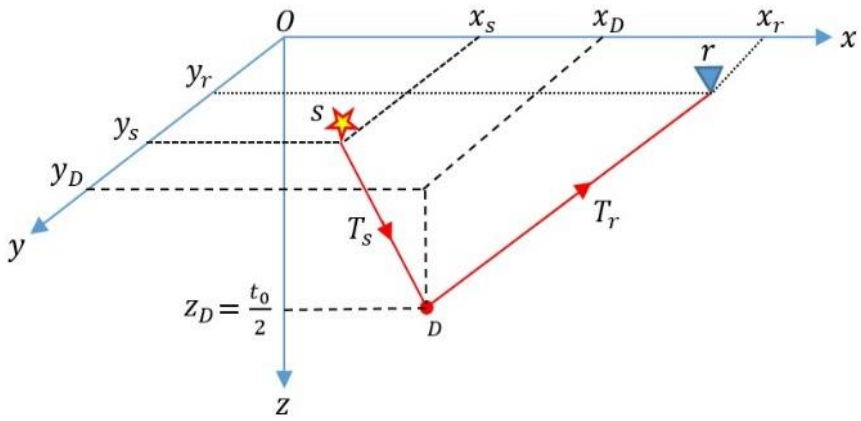

Figure 6.1: 3D geometry of diffraction traveltime ray path.

Diffractivity at an image point is obtained through the computation of semblance along diffraction traveltime curves, where the semblance function is defined according to Taner and Koehler (1969) as

$$S = \left[\sum_{t=-m}^{m}\left(\sum_{i=1}^{N} f_{it}\right)^2\right] \Big/ \left(N \sum_{t=-m}^{m}\sum_{i=1}^{N} {f_{it}}^2\right) \tag{6.2}$$

where f_{it} is the i^{th} sample at a given time t within window of length $2m$ samples and N is the number of considered traces. The diffractivity graph (or D-volume/ D-section) consist of the values of the above semblance stack at each image point. Figure 6.2 shows the schematic steps for the prestack diffraction imaging technique. In this study, the goal was to search only for point diffractors and as such phase change associated with diffractions from edges were not considered.

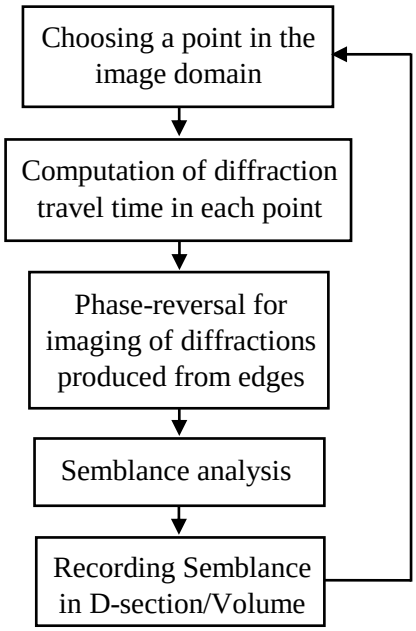

Figure 6.2: The schematic steps in the 3D prestack diffraction imaging technique.

6.4. Application to a 3D synthetic data example

To demonstrate the method for the readers not familiar with diffraction imaging, I began with a simple synthetic test. The 3D velocity model used to generate the synthetic data was a constant velocity cube with the size of 600×600×700 m^3 including several point diffractors at the depth of 400 m (Figure 6.3a). To have higher resolution

images, 14400 receivers and 121 shots were used in the survey. Location of shots used in the survey is shown in Figure 6.3b.

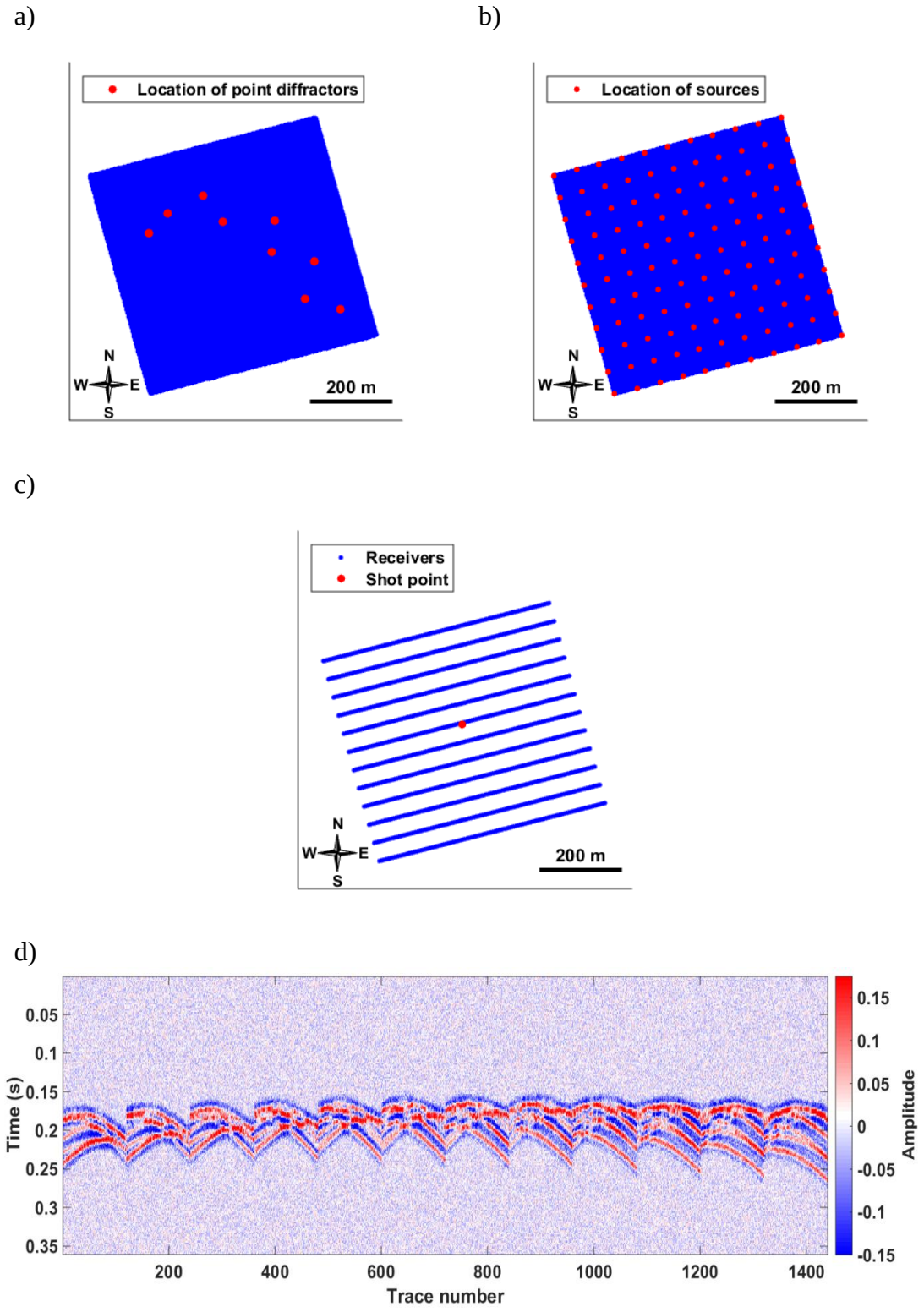

Figure 6.3: a) Point diffractors (red dots) located at 400 m/ 0.16 s within the constant velocity cube, b) location of sources used in the survey (red dots), c) central shot (red dot) and some of the recording receiver lines, and d) the corresponding seismic data.

All receivers were recording each shot. A Ricker wavelet with the dominant frequency of 50 Hz is used for modelling. A sampling interval of 2 ms and geophone spacing of 5 m were used to generate the data. I contaminated the recorded data with random noise with signal-to-noise ratio of 0.75. Figure 6.3c shows the position of the central shot and some of the recording receiver lines and Figure 6.3d shows the corresponding seismic data.

The technique is applied to the noisy data as well as noise-free data. Diffraction traveltime curves were computed using the constant P-velocity cube, for the target time/depth. Finally, D-section was constructed through semblance analysis using a time window of 21 samples along the computed diffraction traveltimes. Figure 6.4a-6.4b show the diffractivity in the target area for the noisy and noise-free data, respectively. Lighter colours indicate higher diffractivity in the D-section. Black dots show the exact position of the point diffractors used to generate the data. It is observed that there is a good match between them and the highest diffractivities in both D-sections. There is negligible contrast between the D-sections constructed for noisy and noise-free seismic data. This demonstrates the robustness of semblance analysis as a coherency measurement of seismic events in the presence of random noise.

a) b)

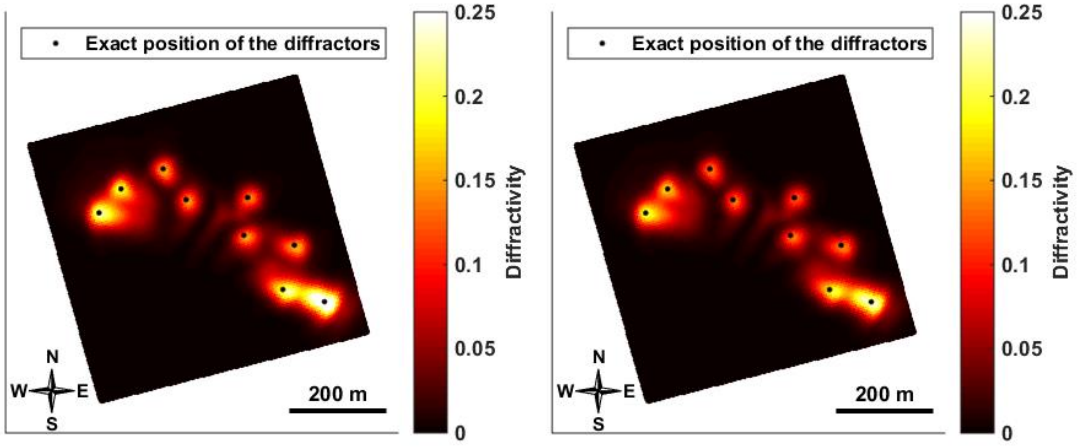

Figure 6.4: D-section constructed for a) noise-free and b) noisy datasets. The lighter the colour, the higher the diffractivity. Black dots indicate the exact location of the point diffractors in the target time/depth slice used in forward modelling.

6.5. Application to 3D field dataset

The 3D prestack diffraction imaging technique is applied to a 3D field data set recorded in 2010 over an area of about 9 km^2 at the Kevitsa Ni-Cu-PGE ore body, northern Finland. Kevitsa is a large, disseminated, Sulfide Ni–Cu–PGE deposit emplaced within layered sedimentary and volcanic rocks of the Central Lapland Greenstone Belt (CLBC) in northern Finland (Mutanen and Huhma, 2001). The CLGB is characterized by Paleoproterozoic supracrustal rocks of volcano-sedimentary stratigraphic groups (Rasanen et al., 2001; Koivisto et al., 2012). The Kevitsa intrusion is part of the Kevitsa-Saatovara igneous complex, separated by the Saatovara fault zone (Mutanen, 1997). The intrusive complex is characterized by an oval-shaped surface expression with a northwest-southeast trending long axis (Koivisto et al., 2012). The ore deposits are located within Olivine Pyroxenite, websterite and their altered derivatives (Koivisto et al., 2012; Lindqvist, 2014). Figure 6.5 shows the bedrock geological map of the area (provided by Kevitsa Mining Oy/First Quantum Minerals Ltd., used by Koivisto et al. (2012) and Malehmir et al. (2012)) and the location of the 3D seismic survey indicated by the dashed rectangle.

Nearly 3300 shot records were generated by a mechanical hammer and explosive sources. There were two separate subsets of the survey with the sampling rate of 1 ms and 2 ms, which were merged to create the 3D seismic volume used in this study. Source and receiver intervals were 45 m and 15 m, respectively. 86765 CDPs with 10 m×10 m bin size were selected so that the maximum fold was 90 and the maximum source-receiver offset was around 1700 m. 35 receiver lines and 34 source lines with the line spacing of 70 m and 80 m were used, giving a nominal receiver and source density of about 800 and 400 per km^2, respectively (Malehmir et al., 2012).

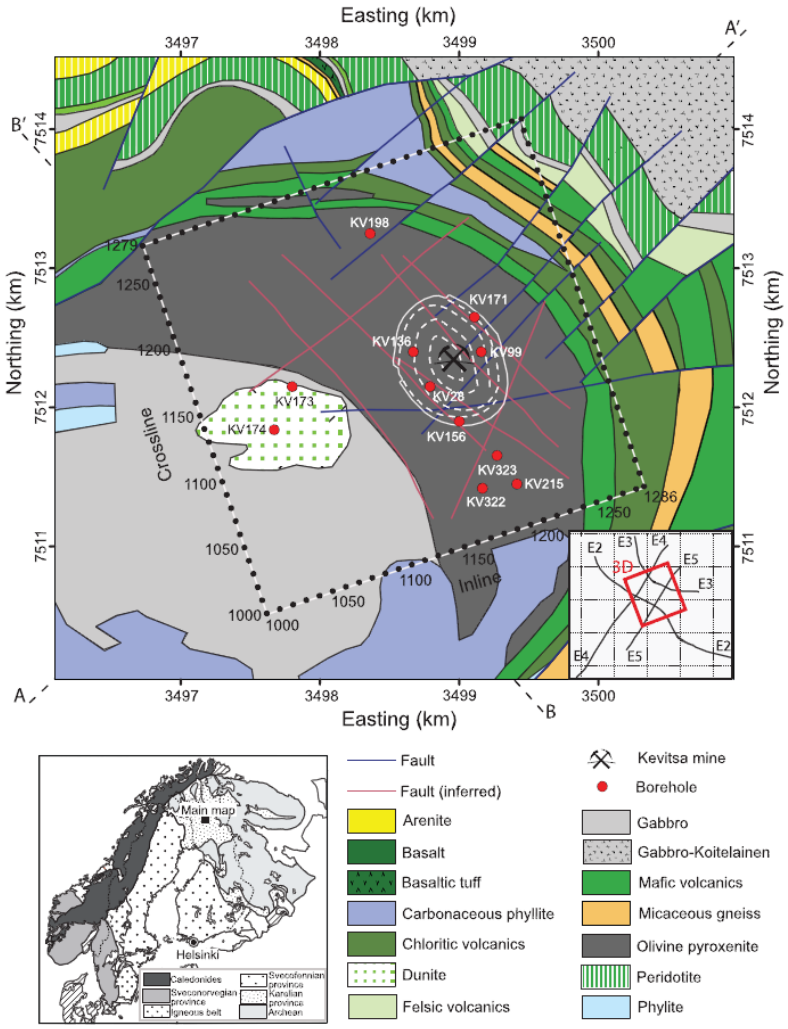

Figure 6.5: Geological map of the Kevitsa Ni-Cu-PGE deposit, showing the location of the 3D survey (boxed area), deep boreholes in the area and inline and crossline numbers used in this study (after Malehmir et al., 2012).

The data set was first processed in 2010 by Dzunic and Urosevic (personal communication) through 3D DMO correction followed by poststack migration. The velocity model used for migration was estimated from DMO corrected CDP gathers. Use of this estimated velocity model causes errors in migration and diffraction imaging in the case of geological complexities in the hard rock environment. In order to handle this problem and to derive a high resolution velocity model, Ziramov et al. (2015), have successfully upgraded the velocity model through an interactive prestack time migration (PreSTM) approach. In this example, I used the velocity model obtained from their approach to apply the proposed prestack diffraction imaging. Figure 6.6 shows the 3D seismic survey and the corresponding fold map (Malehmir et al., 2012).

a)

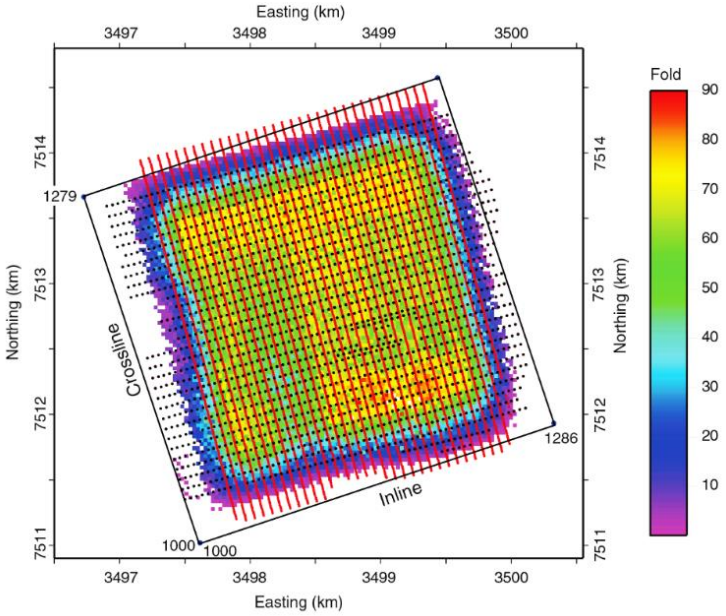

Figure 6.6: 3D seismic survey and the corresponding fold map for the seismic data collected over Kevitsa Ni-Cu-PGE orebody, northern Finland (after Malehmir et al. (2012)).

Figure 6.6a shows the location of a shot and the corresponding recording patch within the acquisition area. Figure 6.6b shows the corresponding pre-processed seismic data (Ziramov et al., 2015) cut to 350 ms.

a)

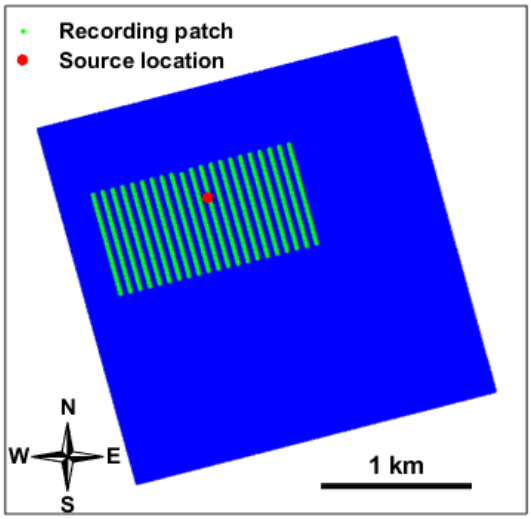

b)

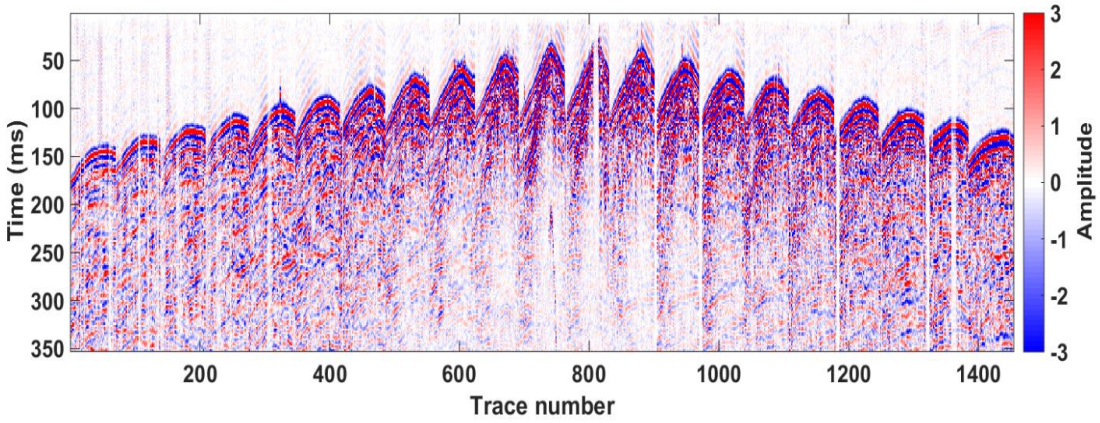

Figure 6.7: a) The location of a shot and the corresponding recording patch within the acquisition area, and b) the corresponding pre-processed seismic data (Ziramov et al., 2015) cut to 350 ms.

Figure 6.8a shows the migration velocity field used for PreSTM and Figure 6.8b illustrates the time slice located at 220 ms extracted from the migrated volume. Using the migration velocity, diffraction traveltimes were computed for each image point. Using these traveltimes, semblance analysis was done to construct diffractivity section through the time windows with a width 34 samples cantered diffraction traveltime curves.

a)

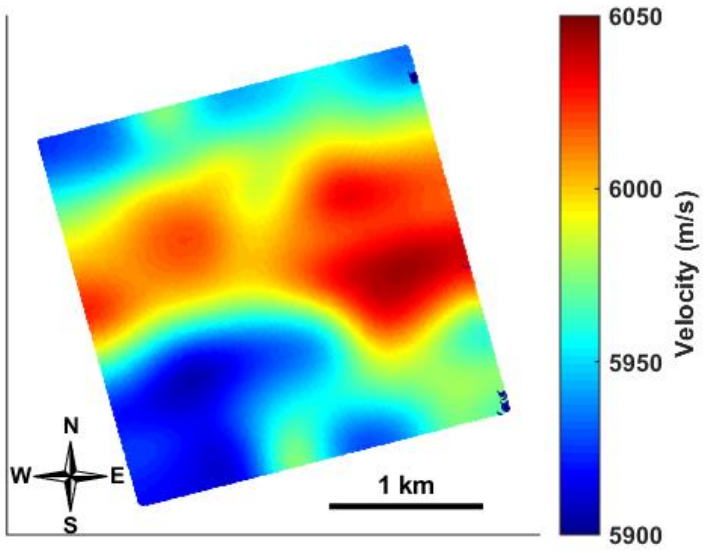

b)

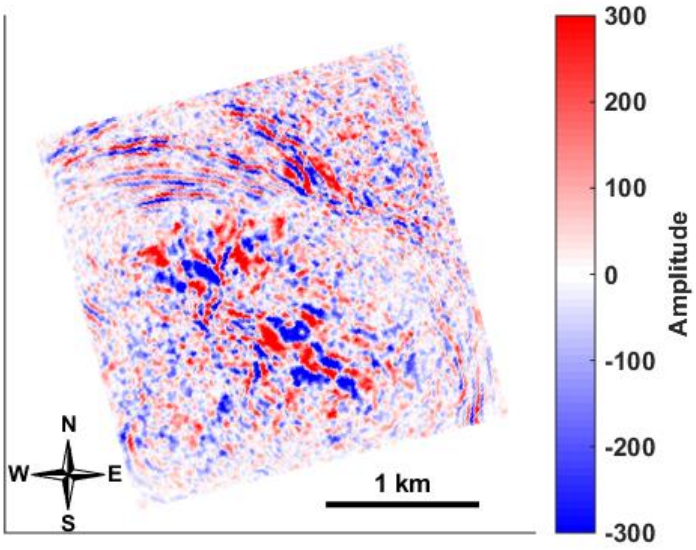

Figure 6.8: a) Velocity field used for PreSTM located at 220 ms and b) the corresponding migrated time slice.

The primary purpose in this field data example was to search for point diffractors generated from objects below seismic resolving power such as sharp edges of vertical intrusions and highly heterogeneous fractured zones. Thus, I did not consider diffractors related to the objects within resolving power of seismic such as bed terminations or sub-horizontal faults with large throws that would require taking care of the edges and the need for the phase-reversals. Figure 6.9a shows the corresponding

computed D-section for the time slice in Figure 6.8b. Again, lighter colors correspond to higher semblance/ diffractivity.

a)

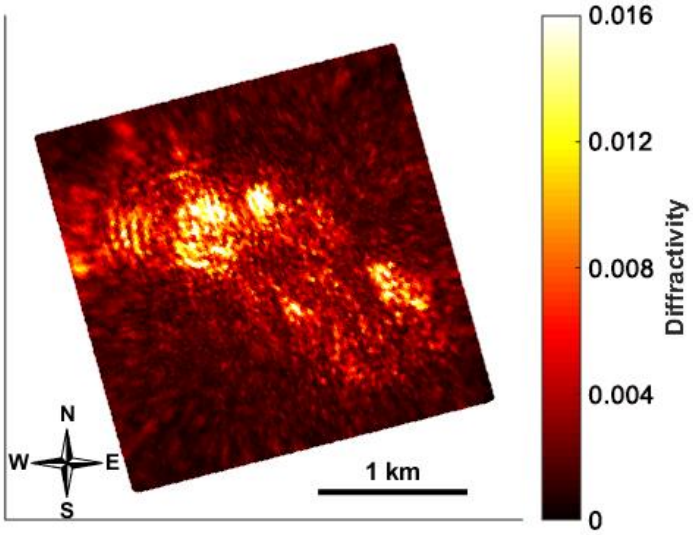

b)

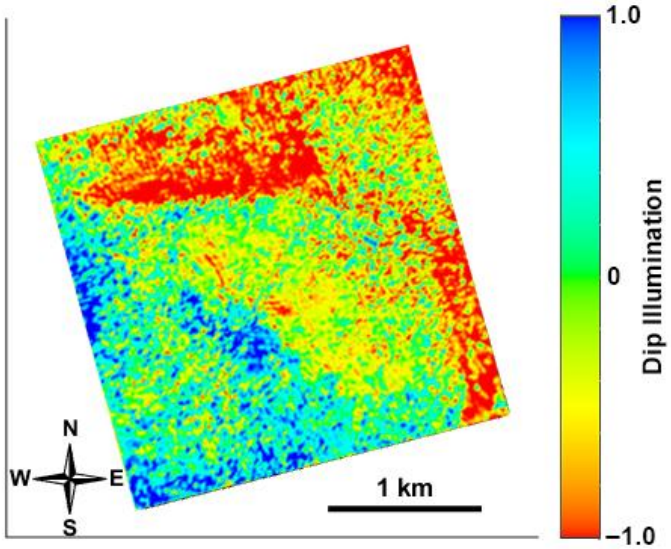

Figure 6.9: a) Diffractivity from the fracture zones and termination of mineralized rocks (Olivine Pyroxenite) and b) the geological structure boundaries extracted by dip-illumination.

The geological map shown in Figure 6.5, inferred from the existing boreholes in the area, contains three main formations, Metasediment and Metavolcanics (top right), Olivine Pyroxenite (central part) and Gabbro (bottom left). Lindqvist (2014) showed that the Olivine Pyroxenite formation is highly fractured. Figure 6.9b shows the dip illumination attribute computed at the target depth. This attribute uses a cross-correlation dip estimation method, and the result is a directional view of the calculated dip, where the direction is in degrees and the dip magnitude. Based on the drill-hole data, the metasediments and metavolcanic layers are dipping approximately 50° to 60° to the south in the northern part of the Kevitsa intrusive complex (Koivisto et al., 2012). In the south, the rock layers display a variety of orientations towards north, south, and east suggesting that the rocks were affected by gentle folding (Koivisto et al., 2012).

In the introduction section it was mentioned that separation of diffractions from reflections may not be necessary in hard rock environment, where the acquired seismic data is not dominated by reflections. To qualitatively investigate this, I included a vertical profile of PreSTM data with horizontal diffractivity slice at the location where the diffractivity is high (Figure 6.10a). The cross section shows that there is almost no reflection in the area of higher diffractivity. To show the validity of time-domain imaging assumption (wave propagation with a constant effective velocity) in hard rock environments, I also computed interval P-velocities from the existing deep boreholes in the area shown in Figure 6.10b. Due to lack of uniformly distributed deep boreholes in the acquisition area, unfortunately, interpolation and/or extrapolation of interval P-velocities is not totally accurate; however, it is observed that there is no considerable lateral velocity change. Note that RMS velocity variations are considerably lower than interval velocity variations.

Comparison between the geological map, dip-illumination and diffractivity shows that the higher diffractivity belongs to the Olivine Pyroxenite formation that hosts the mineral deposits. I interpret the high diffractivity associated with the host rock as being generated by highly fractured zones and terminations of mineralized rocks.

a)

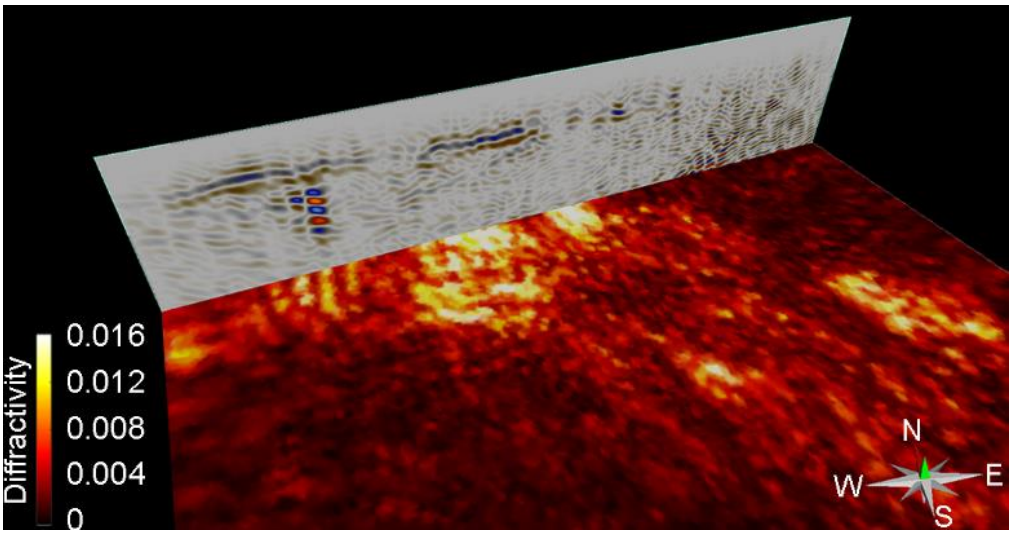

b)

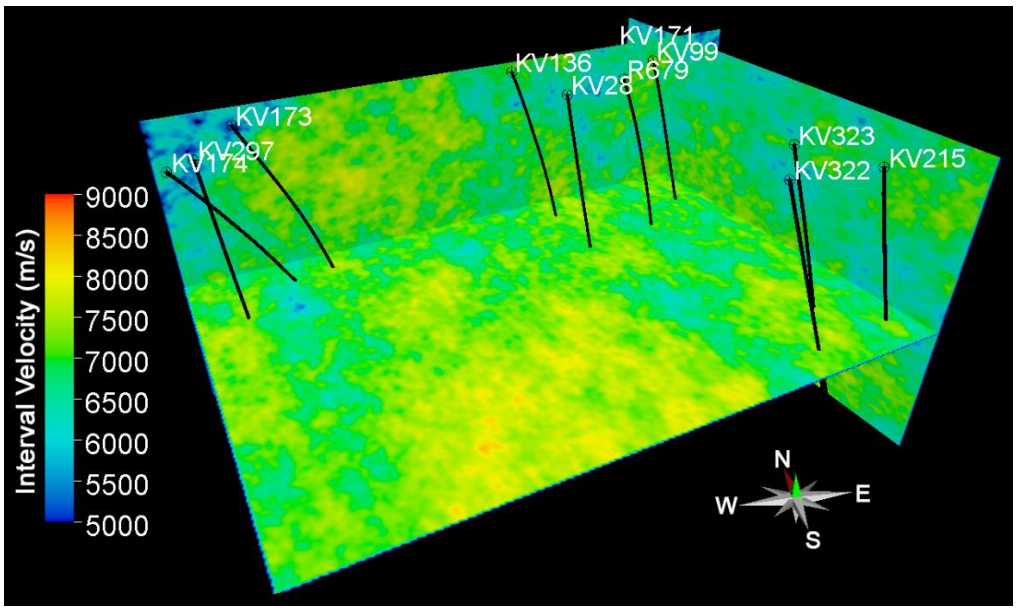

Figure 6.10: a) Vertical profile of PreSTM data with horizontal diffractivity slice at the location of higher diffractivity and b) interval P-velocities computed by interpolation and extrapolation of P-velocities from the existing deep boreholes (black pipes).

6.6. Conclusions

In order to image point diffractors, a 3D prestack diffraction imaging method was applied, based on semblance stacks of seismic energy along diffraction traveltime curves. As such, the method was intended for the detection of point diffractors in 3D seismic data space. The results obtained by the application of the technique to the hard rock field data set, showed a good correlation between the higher diffractivity and the presence of Olivine Pyroxenite rocks that host mineral deposits. I interpret this high diffractivity as being generated by highly fractured zones and the corresponding terminations of mineralization. Since such geological scenarios are often of interest for the exploration of mineral deposits in hard rock environments, it is proposed here that diffractivity should be added to the toolbox of interpreters for the interpretation of seismic data in hard rock environment.

6.7. References

Adam, E., G. Perron, G. Arnold, L. Matthews, and B. Milkereit, 2003, 3D seismic imaging for VMS deposit exploration, Matagami, Quebec, in Eaton, D. W., B. Milkereit, and M. H. Salisbury, eds., Hardrock seismic exploration: SEG, 229–246.

Alonaizi F., R. Pevzner, A. Bóna , V. Shulakova, and B. Gurevich, 2013, 3D diffraction imaging of linear features and its application to seismic monitoring: Geophysical Prospecting **61**, no. 6, 1206-1217.

Bóna A., R. Pevzner, K. Tertyshnikov, A. Greenwood, B. Sun, S. Yavuz, and Urosevic M., 2013, Diffraction Imaging in Hard-rock Environments. 75th Conference and Exhibition, EAGE, Extended Abstracts, doi: 10.3997/2214-4609.20130702.

Claerbout, J. F., 1985, Imaging the earth's interior: Blackwell Scientific Publications.

Dell S., and D. Gajewski, 2011, Common-reflection-surface-based workflow for diffraction imaging: Geophysics, **76**, no. 5, S187-S195.

Eaton, D.W., 1999, Weak Elastic-Wave Scattering from Massive Sulfide Orebodies, Geophysics, **64**, no. 1, 289-299.

Eaton, D.W., B. Milkereit, and M. Salisbury, 2003, Seismic Methods for Deep Mineral Exploration: Mature Technologies Adapted to New Targets: The Leading Edge, **22**, no. 6, 580-585.

Fomel S., E. Landa, and M.T. Taner, 2007, Poststack velocity analysis by separation and imaging of seismic diffractions: Geophysics, **72**, no. 6, U89-U94.

Gibson M. A. S., 2011, Application of seismic to mineral deposit exploration and evaluation: The Leading Egde, **30**, no.6, 616-620.

Gingerich, J. C., M. Peshko, and L. Matthews, 2002, The Development of New Exploration Technologies at Noranda: Seeing More with Hyperspectral and Deeper with 3-D Seismic, CIM bulletin, **95**, no. 1058, 56-61.

Harisson, B., and M. Urosevic, 2012, Seismic processing, inversion, and AVO for gold exploration — Case study from Western Australia: Geophysics, **77**, no. 5, WC235–WC243.

Harlan W.S., J. F. Claerbout, and F. Rocca, 1983, Extracting velocities from diffractions: 53rd Annual International Meeting, SEG, Expanded Abstracts, **2**, no. 1, 574-577.

Kanasewich E.R., and S.M. Phadke, 1988, Imaging discontinuities on seismic sections: Geophysics, **53**, 334–345.

Klem-Musatov K.D., and A.M. Aizenberg, 1989, The edge wave superposition method (2D scalar problem): Geophysical Journal International, **99**, 351–367.

Khaidukov V., E. Landa, and T.J. Moser, 2004, Diffraction imaging by focusing-defocusing: An outlook on seismic super resolution: Geophysics, **69**, 1478–1490.

Khoshnavaz M. J., A. Bóna, M. Urosevic, S. Ziramov, and P. Ahmadi, 2015, Pre-stack diffraction imaging and its application in hard rock environment, 77th Conference and Exhibition, EAGE, Extended Abstracts, We N116 01, doi: 10.3997/2214-4609.201413006.

Klokov A. and S. Fomel, 2012, Separation and imaging of seismic diffractions using migrated dip-angle gathers: Geophysics, **77**, no. 6, S131-S143.

Koivisto E., A. Malehmir, P. Heikkinen, S. Heinonen, and I. Kukkonen, 2012, 2D reflection seismic investigations at the Kevitsa Ni-Cu-PGE deposit, northern Finland: Geophysics, **77**, no. 5, WC149-WC162.

L'Heureux, E., B. Milkereit, and E. Adam, 2005, 3D Seismic Exploration for Mineral Deposits in Hardrock Environments: CSEG Recorder: 36-39.

Landa E., V. Shtivelman, and B. Gelchinsky, 1987, A method for detection of diffracted waves on common-offset sections: Geophysical Prospecting, **35**, 359–373.

Landa E., and S. Keydar, 1998, Seismic monitoring of diffraction images for detection of local heterogeneities: Geophysics, **63**, no. 3, 1093-1100.

Lindqvist T., 2014, 3D Characterization of Brittle Fracture Zones in Kevitsa Open Pit Excavation, northern Finland: M.S. thesis, University of Helsinki.

Malehmir A., C. Juhlin, C. Wijns, M. Urosevic, P. Valasti, and E. Koivisto, 2012, 3D reflection seismic imaging for open-pit mine planning and deep exploration in the Kevitsa Ni-Cu-PGE deposit, northern Finland: Geophysics, **77**, no. 5, WC95-WC108.

Merzlikin D., and S. Fomel, 2015, An efficient workflow for path-integral imaging of seismic diffractions, 85th Annual International Meeting, SEG, Expanded Abstract, 4096-4100, doi: http://dx.doi.org/10.1190/segam2015-5849464.1.

Milkereit, B., E.K. Berrer, A.R. King, A.H. Watts, B. Roberts, E. Adam, D.W. Eaton, J. Wu, and M.H. Salisbury, 2000, Development of 3−D Seismic Exploration Technology for Deep Nickel-Copper Deposits-a Case History from the Sudbury Basin, Canada: Geophysics, **65**, 1890-1899.

Milkereit, B., D. Eaton, J. Wu, G. Perron, M.H. Salisbury, E. Berrer, and G. Morrison, 1996, Seismic Imaging of Massive Sulfide Deposits; Part Ii, Reflection Seismic Profiling, Economic Geology, **91**, no. 5, 829-834.

Moser T.J., and C.B. Howard, 2008, Diffraction imaging in depth: Geophysical Prospecting, **56**, 627–641.

Mutanen, T., 1997, Geology and Ore Petrology of the Akanvaara and Koitelainen Mafic Layered Intrusions and the Keivitsa-Satovaara Layered Complex, northern

Finland: Geological Survey of Finland, **395**, Report available at: www.arkisto.gsf.fi/bul/BT395.pdf .

Mutanen, T., and H. Huhma, 2001, U-Pb geochronology of the Koitelainen, Akanvaara and Keivitsa mafic layered intrusions and related rocks, in Vaasjoki, M., ed., Radiometric age determinations from Finnish Lapland and their bearing on the timing of Precambrian volcano-sedimentary sequences: Geological Survey of Finland, Special Paper 33, 229–246.

Papziner U., and K.P. Nick, 1998, Automatic detection of hyperbolas in georadargrams by slant-stack processing and migration: First Break, **16**, 219–223.

Räsänen, J., and H. Huhma, 2001, U-Pb datings in the Sodankylä schist area, central Finnish Lapland: Geological Survey of Finland, Special Paper, **33**, 153–188.

Rauch-Davies M., A. Berkovitch and K. Deev, 2013, Using Multi-Focusing 3-D Diffraction Imaging to Predict Fracture Swarms in Unconventional Reservoirs, Unconventional Resources Technology Conference (URTEC).

Salisbury, M.H., B. Milkereitz, G. Ascough, R. Adair, L. Matthews, D.R. Schmitt, J. Mwenifumbor, D.W. Eaton, and J. Wu, 2000, Physical Properties and Seismic Imaging of Massive Sulfides: Geophysics, **65**, no. 6, 1882–1889.

Sava P.C., B. Biondi, and J. Etgen, 2005, Wave-equation migration velocity analysis by focusing diffractions and reflections: Geophysics, **70**, no. 3, U19-U27.

Taner M.T., and M. Koehler, 1969, Velocity spectra-digital computer derivation applications of velocity functions: Geophysics, **34**, no. 6, 859-881.

Taner M.T., and S. Fomel, 2006, and E. Landa, Separation and imaging of seismic diffractions using plane-wave decomposition: 76th Annual International Meeting, SEG, Expanded Abstracts, 2401-2405.

Trorey A.W., 1977, Diffractions for arbitrary source-receiver locations: Geophysics, **42**, 1177–1182.

Urosevic M., G. Bhat, and M.H. Grochau, 2012, Targeting nickel sulfide deposits from 3D seismic reflection data at Kambalda, Australia: Geophysics, **77**, no. 5, WC123–WC132.

Veeken P., M. DaSilva, M. Rauch-Davies, and A. Soto Cuervo, 2004, Pre-and Post-Stack Seismic Attributes for Enhancing Production from Cocuite Gas Reservoirs: 66th Conference and Exhibition, EAGE, Extended Abstracts.

Vermeulen J., B. Gurevich, M. Urosevic, and E. Landa, 2006, Enhancing coherency analysis for fault detection and mapping using 3D diffraction imaging: 76th Annual International Meeting, SEG, Expanded Abstracts, 1108–1112.

Ziramov S., A. Dzunic, and M. Urosevic, 2015, Kevitsa Ni-Cu-PGE deposit, North Finland, A seismic case study: 24th Annual International Meeting, ASEG, Expanded Abstracts, Perth, Australia, Expanded Abstracts, no. 1, 1-4.

7. Conclusions and discussion

Diverse techniques and unconventional approaches developed during this research had one common goal: achieving accurate and robust time-domain imaging of a generally complex underground. The advancements achieved are discussed in each chapter and are summarized here.

7.1. Oriented time-domain imaging

Three new oriented time-domain techniques were developed in microseismic/ passive-seismic location, seismic anisotropy and prestack migration.

7.1.1. Microseismic/Passive-seismic location

The oriented microseismic/passive-seismic location technique was applied on several synthetic examples and on a field data set. The results achieved by the application of proposed technique in a constant velocity model and a laterally homogeneous example provided an estimates of the source coordinate that is within a small tolerance of the true position. Using another synthetic example with lateral velocity variation, it was shown that the applicability of the technique is limited to horizontally layered media that is suitable for many unconventional reservoirs. The technique was also applied to a real data example, finding that the derived location was consistent with values from a previous study that used a calibrated velocity model form a single borehole.

I incorporated bootstrapping technique, which is a robust statistical tool suited for the experiments that are not repeatable, for evaluation of level of uncertainty in the estimated locations. This tool, bootstrap technique, can be employed in different branches of seismic data processing.

Future advancement in this area may include:

- Use of non-parametric strategies to smooth the time arrivals.
- Extension of the oriented passive seismic technique for the situations with VTI anisotropy, using different traveltime approximations.
- Generalize the approach for situations with arbitrary layered media.

7.1.2. Kinematic attributes in VTI media

An oriented algorithm for the inversion of kinematic attributes in VTI media was proposed that does not require a prior knowledge of a velocity model. I demonstrated the theoretical contents of the algorithm to a synthetic data example. The validity of the algorithm was first verified using a synthetic example, and then demonstrated on a case of real data situation. The algorithm builds on the old techniques, but it was further developed version of the previous techniques. The main advantages of the algorithm over the other algorithms belong to its

- Fully automation,
- Time-efficiency, and
- Curvature independence.

7.1.3. Prestack time-domain migration

I proposed a new oriented prestack time-domain migration approach, for planar reflectors in common source domain. The main advantages of the techniques over the previous algorithms are

- Seismic data is directly mappable from one domain (common source) to image domain,
- Preserves both the seismic amplitude and frequency contents of seismic data, and

- Higher order derivatives of traveltime with respect to offset are removed from the previous techniques. The need for the derivatives was replaced by point-to-point mapping using predictive painting technique.

The oriented velocity model constructed based on the presented approach in time-domain, can be used as the initial velocity model for depth-domain seismic imaging.

As a future of this research, there is a possibility to develop an oriented time-domain dip-moveout correction (DMO) algorithm using the same approach.

7.2. Diffraction imaging

In the last two technical chapters of the thesis, I suggested to take anisotropy into account in VTI media in poststack domain and also suggested to use diffractivity as a strong attribute in the interpretation of seismic data collected over hard rock environment.

7.2.1. 2D poststack diffraction imaging in VTI media

I suggested to consider anisotropy in poststack seismic domain by considering P-wave non-hyperbolic diffraction traveltime approximations for VTI media. It was demonstrated that application of so-called normal moveout traveltime approximation in the presence of anisotropy results in low resolution image, weak diffractivity and misplacement of diffractors in D-sections. Among six different diffraction traveltime approximations, it was shown that use of generalized moveout approximation (GMA) resulted in the most accurate image.

There are three possibilities in the potential future of the research:

- To extend the presented technique to 3D poststack diffraction imaging
- The inputs of the presented technique are the effective velocity (v) and anellipticity parameter (η). It is possible to first estimate the kinematic attributes (v,η) from the technique presented in chapter 3; then to apply the poststack diffraction imaging technique.

- It is also possible to estimate the kinematic attributes and apply the presented diffraction imaging technique simultaneously. The advantage is to calibrate the velocity model built from velocity analysis in prestack domain, although, it can be more time-consuming.
- Another future of the research (with the above potentials) is to apply the technique to field data examples.

7.2.2. 3D prestack diffraction imaging in hard rock environments

In hard rock environment the scattered energies from small scale objects, edges and wedges of vertical intrusions, are the dominant energies. It was suggested to employ diffractivity as another seismic attribute, with other existing attributes, for the interpretation of seismic data in hard rock environment. It is based on the results obtained by the application of a 3D prestack diffraction imaging technique to a hard rock field data set. The results indicate strong correlation between the higher diffractivities and the location of the fractured host rocks that often contain mineral deposits.

Roads ahead and future developments in this zone may include:

- Further testing with different field seismic data sets, and
- To consider anisotropic double-square-root equations to compute diffraction traveltimes.

8. Appendix

Permissions

SEG publishes journals, books, and digital works with the primary aim of disseminating research in and theory and applications of applied geophysics. Consistent with this objective, the Society provides mechanisms for those who seek to reuse or republish material from SEG publications while protecting the viability of the SEG publications program. Any further questions about permissions can be sent via email to the SEG publications department at permissions@seg.org.

Fair use
Authors and publishers may present or republish up to two figures or tables per SEG article or per SEG book without seeking written permission from SEG, provided that full acknowledgment of the source is provided in the new work. If SEG has cited a publication for which it is not the publisher, rights should be obtained from that publisher. SEG considers this fair use. There are no fees associated with this permission. Authors who need documentation that SEG is extending this permission are encouraged to print this message and present it to their publishers. Those who require further documentation should contact the SEG publications director. Requests to use any portion of "Seismic Data Analysis: Processing, Inversion, and Interpretation of Seismic Data" should be directed to the SEG publications director.

Permission granting
Those seeking permission to republish more material than described above should contact the SEG publications director. Such requests should include complete citations of works for which permission to republish is sought. If permission for specific figures or tables is sought, please provide figure and table numbers. Requests should include a description of the work in which the SEG material would be republished. Information about the audience and the intended distribution also should be included. The requests should be prepared on institutional letterhead if the requesting party is representing an institution. License fees are assessed only when the request is for a large amount of material or when the proposed usage is commercial in nature or would limit SEG's market. If a license fee is assessed, it must be paid prior to use or the permission is void.

Purchase redistribution rights online
Those seeking to redistribute SEG publications or portions thereof in print, by fax, or online may purchase permission to do so online. SEG publications are registered with the Copyright Clearance Center, and licenses to redistribute SEG articles and portions of books are obtained through this nonprofit agency. Special pricing is available for university professors, including license to distribute SEG material through electronic course packs. Licenses also are available for distribution of journal articles and expanded abstracts via email or posting on Intranets and Extranets for limited time periods.

Authors' right to redistribute
Authors of articles in GEOPHYSICS, INTERPRETATION, THE LEADING EDGE, and the Technical Program *Expanded Abstracts* may post their own articles on their personal Web sites or the Web sites of their institutions without obtaining further permission from SEG. Authors of journal articles and *Expanded Abstracts* retain similar rights for print redistribution. If an author or an author's institution redistributes an author's article online or in print, the original publication venue encompassed in a complete citation and including SEG's status as publisher must be identified. Authors of SEG books, or portions of SEG books, must seek permission from the SEG publications director to redistribute these works in any form. Such permission will not be withheld if SEG's investment in the original publication of the works is not threatened. Questions should be directed to the publications director.

Traditional publication (including green open access)

- No author publication charge (APC) is levied, although payment of mandatory page charges are assessed and payment of voluntary charges is requested. Relief from mandatory charges may be requested under SEG's hardship relief policy.
- Copyright is transferred to SEG.
- Authors/employers retain proprietary rights such as the right to patentable subject matter and the right to make oral presentation of the work with full citation and proper copyright acknowledgment.
- Authors/employers enjoy the right to prepare and hold copyright in derivative publications based on the paper provided that the derivative work is published subsequent to the official date of the original paper's publication by SEG.
- Authors/employers may post a final accepted version of the manuscript or the final SEG-formatted version (book chapters excluded) on authors' personal websites, employers' websites, or in institutional repositories operated and controlled exclusively by authors' employers provided that:
  1. the SEG-prepared version is presented without modification;
  2. copyright notice and a full citation appear with the paper;
  3. a link to the SEG version of record in the SEG Digital Library using Digital Object Identifier (DOI) permalinks is provided;
  4. the posting is noncommercial in nature, and the paper is made available to users without charge; and
  5. that notice be provided that use is subject to SEG terms of use and conditions.
- Authors/employers may not post their articles in an institutional repository or other site in which the content is required to carry or is implied as carrying a license contrary to SEG copyright and terms of use and terms of this policy.
- Authors/employers may post to their own websites a preprint (a version prior to SEG peer review) of a submitted manuscript provided that the posting is accompanied by prominent notice that the paper is under review for publication by SEG and the publication to which the manuscript has been submitted is identified. Upon publication of the paper by SEG, the author must replace any previously posted electronic versions of the paper with either (a) a full citation to the SEG-published work with a DOI permalink to the paper's abstract or (b) the final version of the manuscript or SEG-formatted version (book chapters excluded) subject to SEG conditions for such posting.
- Authors may reuse all or part of their papers published with SEG in a thesis or dissertation that authors write and are required to submit to satisfy criteria of degree-granting institutions.
- Authors/employers have the nonexclusive right, after publication by SEG, to give permission to third parties to republish print versions of the paper, or excerpts therefrom, without obtaining permission from SEG, provided that:
  1. the SEG-prepared version is not used for this purpose;
  2. the paper is not republished in another journal or book; and
  3. the third party does not charge a fee. Permission must be obtained from SEG for other republication of the paper.

seg.org/Publications/Policies-and-Permissions/Open-Access-Policy#null

JOHN WILEY AND SONS LICENSE TERMS AND CONDITIONS

Jun 15, 2017

This Agreement between Curtin University -- Mohammad Javad Khoshnavaz ("You") and John Wiley and Sons ("John Wiley and Sons") consists of your license details and the terms and conditions provided by John Wiley and Sons and Copyright Clearance Center.

License Number	4130290511351
License date	Jun 15, 2017
Licensed Content Publisher	John Wiley and Sons
Licensed Content Publication	Geophysical Prospecting
Licensed Content Title	Post-stack diffraction imaging in vertical transverse isotropy media using non-hyperbolic moveout approximations
Licensed Content Author	M. Javad Khoshnavaz,Andrej Bóna,Milovan Urosevic
Licensed Content Date	May 11, 2017
Licensed Content Pages	1
Type of use	Dissertation/Thesis
Requestor type	Author of this Wiley article
Format	Print and electronic
Portion	Full article
Will you be translating?	No
Title of your thesis / dissertation	Coherency based time-domain imaging algorithms
Expected completion date	Jun 2017
Expected size (number of pages)	8
Requestor Location	Curtin University Technology Park West Precinct ARRC/CSIRO Building, H Block, Level 4 26 Dick Perry Ave Kensington, Western Australia 6151 Australia Attn: M. Javad Khoshnavaz
Publisher Tax ID	EU826007151
Billing Type	Invoice
Billing Address	Curtin University Technology Park West Precinct ARRC/CSIRO Building, H Block, Level 4 26 Dick Perry Ave Kensington, Australia 6151 Attn: M. Javad Khoshnavaz
Total	0.00 AUD